Ion Energy Measurements in Plasma Immersion Ion Implantation.

by

Scott Young Allan

A thesis submitted for the degree of

Doctor of Philosophy

Applied and Plasma Physics

The School of Physics

The University of Sydney

Australia

March 2009

Declaration of Originality

I certify that this thesis has not previously been submitted for any degree and is not being submitted as part of candidature for any other degree.

I also certify that this thesis has been written by me and that any help I have received in preparing this thesis and all sources used have been acknowledged in this thesis.

Chapter 6 of this thesis is based on a paper by S. Y. Allan, C. P. Cornet, D. R. McKenzie and M. M. M. Bilek. C. P. Cornet provided guidance on the set up of the computer simulations and D. R. McKenzie and M. M. M. Bilek assisted with analysis of results. All simulation and experimental results were obtained by S. Y. Allan, and all text was written by S. Y. Allan with editing by the co-authors.

Chapter 7 of this thesis is based on a paper by S. Y. Allan, D. R. McKenzie and M. M. M. Bilek. D. R. McKenzie and M. M. M. Bilek assisted with analysis of results. All simulation and experimental results were obtained by S. Y. Allan, and all text was written by S. Y. Allan with editing by the co-authors.

Signature of candidate:

.....

Scott Young Allan

Author's Publications

Refereed Journal Articles

1. S. Y. Allan, D. R. McKenzie and M. M. M. Bilek, Ion energy measurements during plasma immersion ion implantation of an insulator. *Plasma Sources Science and Technology*, 2009. (submitted 6th March, 2009)

2. S. Y. Allan, C. P. Cornet, D. R. McKenzie and M. M. M. Bilek, Ion energy measurements in mesh assisted plasma immersion ion implantation. *Journal of Plasma and Fusion Research*, 2009. (in press)

3. Y. Yin, S. Y. Allan, M. M. M. Bilek and D. R. McKenzie, Time dependent plasma properties during microarcing in radio frequency plasmas. *Applied Physics Letters*, 91(19):191501-1-191501-3, 2007.

Conference Presentations

1. S. Y. Allan, C. P. Cornet, D. R. McKenzie and M. M. M. Bilek, Ion Energy Measurements in Mesh Assisted Plasma Immersion Ion Implantation. *8th Japan-Australia Plasma Diagnostics Workshop*, Murramarang, Australia, 2009.

2. S. Y. Allan, C. P. Cornet, D. R. McKenzie and M. M. M. Bilek, Ion Energy Measurements in Mesh Assisted Plasma Immersion Ion Implantation. *International Congress on Plasma Physics*, Fukuoka, Japan, 2008.

3. C. P. Cornet, S. Y. Allan, D. R. McKenzie and M. M. M. Bilek, Ion Energy Distributions in Mesh Assisted Plasma Immersion Ion Implantation. *Gaseous Electronics Meeting*, Murramarang, Australia, 2008.

Acknowledgements

This thesis would not have been possible without the help of many people. I would like to thank my supervisors, David McKenzie and Marcela Bilek for all their help and guidance during my research work. I would also like to thank Yongbai Yin for allowing me to work in his research laboratory and for his help and advice with the experimental aspects of my project.

I would like to thank Christophe Cornet for his help and advice with the computer simulation work in this thesis. My thanks also to Phil Denniss for his work in the construction of the analyser circuit board and other vital electronic components which I so often managed to break or burn. My thanks to Robert Davies for his assistance in the construction of components for the analyser and for all his technical support. My thanks also to John Pigott for his useful advice and to Brian James for proof reading my thesis.

I would like to thank Christophe Cornet, Bradley Steel, Selina Lee and all my friends in the Applied/Plasma Physics group for their friendship and support.

Finally, I would like to express my thanks to my family. In particular, I would like to thank my parents for their unwavering support and encouragement and it is with grateful thanks that this thesis is dedicated to my mother and father.

Abstract

This thesis investigates ion energy distributions (IEDs) during plasma immersion ion implantation (PIII). PIII is a surface modification technique where an object is placed in a plasma and pulse biased with large negative voltages. The energy distribution of implanted ions is important in determining the extent of surface modifications. IED measurements were made during PIII using a pulse biased retarding field energy analyser (RFEA) in a capacitive RF plasma. Experimental results were compared with those obtained from a two dimensional numerical simulation to help explain the origins of features in the IEDs. Time resolved IED measurements were made during PIII of metal and insulator materials and investigated the effects of the use of a metal mesh over the surface and the effects of insulator surface charging.

When the pulse was applied to the RFEA, the ion flux rapidly increased above the pulse-off value and then slowly decreased during the pulse. The ion density during the pulse decreased below values measured when no pulse was applied to the RFEA. This indicates that the depletion of ions by the pulsed RFEA is greater than the generation of ions in the plasma. IEDs measured during pulse biasing showed a peak close to the maximum sheath potential energy and a spread of ions with energies between zero and the maximum ion energy. Simulations showed that the peak is produced by ions from the sheath edge directly above the RFEA inlet and that the spread of ions is produced by ions which collide in the sheath and/or arrive at the RFEA with trajectories not perpendicular to the RFEA front surface. The RFEA discriminates ions based only on the component of their velocity perpendicular to the RFEA front surface.

To minimise the effects of surface charging during PIII of an insulator, a metal mesh can be placed over the insulator and pulse biased together with the object.

Measurements were made with metal mesh cylinders fixed to the metal RFEA front surface. The use of a mesh gave a larger ion flux compared to the use of no mesh. The larger ion flux is attributed to the larger plasma-sheath surface area around the mesh. The measured IEDs showed a low, medium and high energy peak. Simulation results show that the high energy peak is produced by ions from the sheath above the mesh top. The low energy peak is produced by ions trapped by the space charge potential hump which forms inside the mesh. The medium energy peak is produced by ions from the sheath above the mesh corners. Simulations showed that the IED is dependent on measurement position under the mesh.

To investigate the effects of insulator surface charging during PIII, IED measurements were made through an orifice cut into a Mylar insulator on the RFEA front surface. With no mesh, during the pulse, an increasing number of lower energy ions were measured. Simulation results show that this is due to the increase in the curvature of the sheath over the orifice region as the insulator potential increases due to surface charging. The surface charging observed at the insulator would reduce the average energy of ions implanted into the insulator during the pulse. Compared to the case with no mesh, the use of a mesh increases the total ion flux and the ion flux during the early stages of the pulse but does not eliminate surface charging. During the pulse, compared to the no mesh case, a larger number of lower energy ions are measured. Simulation results show that this is caused by the potential in the mesh region which affects the trajectories of ions from the sheaths above the mesh top and corners and results in more ions being measured with trajectories less than ninety degrees to the RFEA front surface.

Contents

Chapter 1

Introduction

1.1 Overview

In materials processing, plasmas are widely used in the deposition of thin films and for the modification of surfaces. Plasma immersion ion implantation (PIII) is a surface modification technique which was first introduced in the nineteen eighties [27] and is increasingly being used in the treatment of metals, semiconductors and insulators.

In PIII, surfaces are modified by ion bombardment which is achieved by placing the object in a plasma and pulse biasing it with large negative voltages. PIII treated surfaces show improved properties such as increased hardness in metals [11] and improved wetting and adhesive properties in polymers [65, 50]. For an insulator, a common treatment method involves pulse biasing a conductive mesh around the object to reduce the effects of surface charging [41].

In PIII, the ion energy distribution (IED) is an important parameter in determining the extent of surface modifications including the concentration profile of implanted ions. To date, there have only been a limited number of experimental measurements of time resolved IEDs during PIII. One of the reasons for this is the difficulty in obtaining measurements at the high voltages (up to -100 kV) and over the short time scales (pulse lengths of tens of microseconds) used in PIII. Experimental measurements of the IED during mesh assisted PIII are particularly important as ion collisions inside the mesh region will affect the IED.

The aim of this project is to develop a greater understanding of the factors affecting the IED during mesh assisted PIII. In this project, a compact multi grid retarding field energy analyser has been designed and constructed. The time resolved ion energy measurements made under a conducting mesh for both metal and insulator materials are, to the author's knowledge, the first measurements of their type reported. The effects of mesh height and pulse amplitude were investigated and compared with a two dimensional numerical simulation.

1.2 Thesis Outline

This thesis consists of eight chapters. In chapter 2, an introduction to the basic plasma physics used in this thesis is given. In chapter 3, the plasma immersion ion implantation (PIII) method is introduced along with a review of simulation and experimental measurements of ion dose and energy during PIII. The ion energy measurements in this thesis were made using a retarding field energy analyser and in chapter 4, a description of the design and testing of this analyser is given. In chapter 5, the effects of pulse amplitude on ion flux and energy during PIII are investigated experimentally and compared with results obtained using a two dimensional numerical simulation. In chapter 6, the effects of a metal mesh on ion flux and energy at a conductive substrate are investigated experimentally and using computer simulation. When immersed in a plasma, the potential of an insulator surface will increase and in chapter 7, the effects of a Mylar insulator around the RFEA inlet, both with and without a mesh present, are investigated experimentally and using computer simulation. In chapter 8, a summary of the main findings of this thesis and their implications for PIII are discussed.

Chapter 2

Physics of Processing Plasmas

2.1 Introduction

In this chapter, a general introduction to the plasma physics used in this thesis is given. The theory presented is drawn largely from the work of Lieberman and Lichtenberg [81]. In section 2.2, some of the important terms used to describe plasmas such as the Debye length, mean free path and plasma frequency are discussed. In section 2.3, the concept of the plasma sheath is introduced. The plasmas used in this thesis were generated using a capacitive parallel plate radio frequency (RF) system and in section 2.4, an introduction to this type of plasma is given. In section 2.5, a discussion is presented about the factors determining the IED in a RF plasma.

2.2 Plasma Parameters

A plasma is a partially ionised gas made up of an approximately equal number of positively (n_i) and negatively (n_e) charged species and a different number of neutral gas molecules (n_g) [20]. There are a wide variety of plasmas which differ in their charged particle density (n_0) and electron temperature (T_e). Plasmas can range from low temperature, low density plasmas found in interstellar regions and nebulae ($T_e \approx 1$ eV and $n_0 \approx 1$ to 10^3 cm^{-3}) to high temperature, high density plasmas found in fusion experiments ($T_e \approx 10^4$ eV and $n_0 \approx 10^{15}$ cm^{-3}) [121].

Low pressure plasma discharges have important applications in materials depo-

sition and surface modification [81] and are the subject of this thesis. These plasmas are electrically driven with densities of around 10^8 to 10^{13} cm^{-3} and have electron temperatures of between 1 to 10 eV. The degree of ionisation is approximately 10^{-4} so that most species are neutrals. These systems are usually not in thermal equilibrium with the electron temperature (T_e) much greater than the ion temperature (T_i). The operating pressures for these plasmas are between 1 mTorr to 1 Torr (0.13 to 133 Pa).

2.2.1 Debye Length

An important length scale in plasma physics is given by the electron Debye length (λ_{De}). The Debye length is defined by considering the potential around a negatively charged conductive sheet introduced into a neutral plasma where $n_i = n_e = n_0$. Plasma electrons are repelled from near the sheet. Due to their larger mass and slower velocity, ions are assumed to remain stationary so that $n_i = n_0$ near the sheet. Using Poisson's equation in one dimension, the potential (ϕ) is given by

$$\frac{d^2\phi}{dx^2} = -\frac{e}{\epsilon_0}\left(n_i - n_e\right) \tag{2.1}$$

Assuming a Boltzmann distribution, the electron density is given by

$$n_e = n_0 e^{\frac{\phi}{T_e}} \tag{2.2}$$

Using equation (2.2) and $n_i = n_0$, equation (2.1) becomes

$$\frac{d^2\phi}{dx^2} = \frac{n_0 e}{\epsilon_0}\left(e^{\frac{\phi}{T_e}} - 1\right) \tag{2.3}$$

Assuming that the sheet is placed at $x = 0$ and has a potential ϕ_0 and that $\phi = 0$ at $x = \pm\infty$, the solution to (2.3) is given by

$$\phi(x) = \phi_0 e^{-\left(\frac{x}{\lambda_{De}}\right)} \tag{2.4}$$

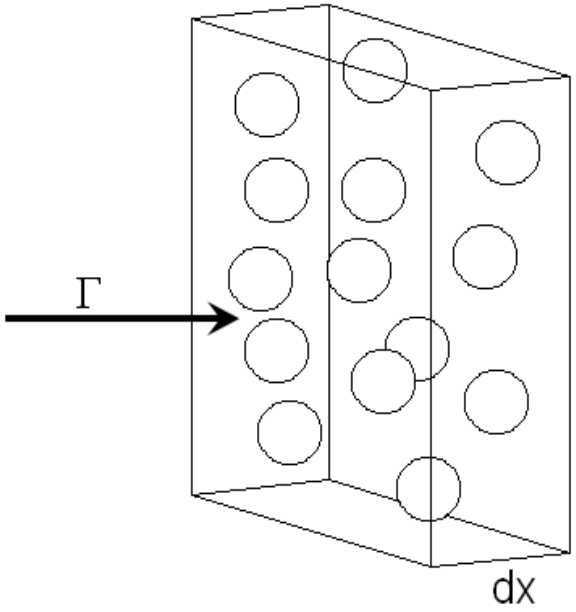

Figure 2.1: The collision cross section (σ) is defined for a flux (Γ) of particles incident upon a slab, of width dx, of stationary molecules with particle density n_g.

where the Debye length λ_{De} is defined by

$$\lambda_{De} = \left(\frac{\epsilon_0 T_e}{e n_0} \right)^{\frac{1}{2}} \tag{2.5}$$

The Debye length describes how rapidly a potential perturbation is shielded by a plasma. Over a distance of λ_{De}, a perturbation will be reduced to $1/e$ of its original value.

2.2.2 Collision Processes

Collisions between particles in a plasma are important in determining particle energy and motion. Collisions are elastic where there is only a transfer of kinetic energy or inelastic where internal energies are affected.

The collision cross section (σ) is defined by considering a flux (Γ) of particles incident upon a slab, of width dx, of stationary particles with particle density n_g as shown in figure 2.1.

The incoming particle flux is given by

$$\Gamma = n\bar{v} \tag{2.6}$$

where n is the particle density and $\bar{v}$ is the particle velocity. The number of particles which interact with the stationary molecules is given by

$$dn = \sigma n n_g dx \tag{2.7}$$

where σ is defined to be the cross sectional area for the interaction. If the collision is elastic and between two identical hard spheres of radius a_1 and a_2, the two spheres will only collide if their centres come within a distance $a_{12} = a_1 + a_2$ of each other. In this situation, the collisional cross section is defined to be πa_{12}^2. For most collisions, σ is dependent on the incoming particle velocity. However, for pressures in the mTorr range the hard sphere cross section provides a reasonable approximation of the collisional cross section. The change in flux ($d\Gamma$) over the distance dx can be expressed by multiplying both sides of equation (2.7) by $\bar{v}$

$$d\Gamma = -\sigma \Gamma n_g dx \tag{2.8}$$

Assuming the incoming flux at $x = 0$ is given by Γ_0, equation (2.8) can be integrated to give

$$\Gamma = \Gamma_0 e^{-\sigma n_g x} \equiv \Gamma_0 e^{-x/\lambda} \tag{2.9}$$

where

$$\lambda = \frac{1}{n_g \sigma} \tag{2.10}$$

is defined to be the mean free path. The mean free path defines the distance over which the incoming flux is reduced to $1/e$ of its original value and is a useful estimate of the distance particles will travel before undergoing a collision.

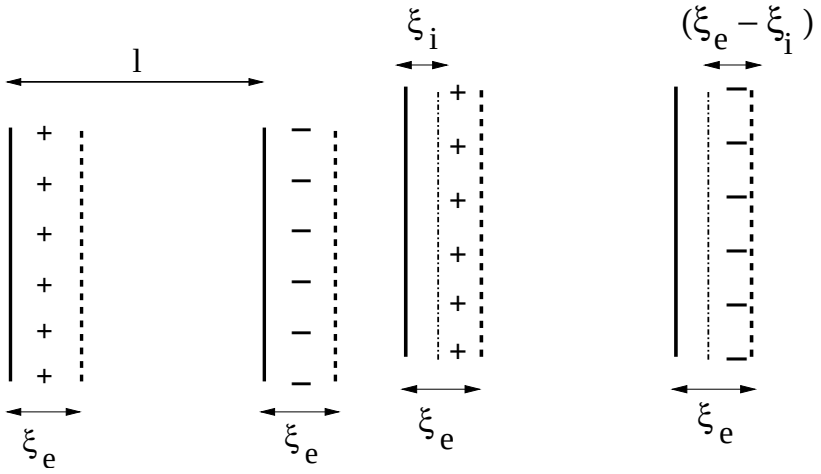

Figure 2.2: Undriven oscillations in a one dimensional slab of plasma of length l. The initial displacement of the electron cloud is shown in (a). The displaced electron cloud will cause a displacement of the ion cloud as shown in (b).

2.2.3 Plasma Oscillations

The frequency of oscillations of the electron and ion densities is important in determining the behaviour of capacitive discharges and the structure of IEDs. The plasma frequency (ω_p) is determined by considering the undriven displacement of an electron and ion cloud with respect to each other in a slab of plasma of length l. The plasma is assumed to contain an equal density of ions and cold electrons ($T_e = 0$) so that $n_i = n_e = n_0$.

If the electron cloud is displaced slightly by a distance $\xi_e(t)$, a surface charge density $\rho_s = en_0\xi_e$ will be uncovered as shown in figure 2.2(a). The uncovered surface charge will cause the ion cloud to shift slightly by a distance $\xi_i(t)$, leading to a surface charge density $\rho_s = en_0(\xi_e - \xi_i)$ as shown in figure 2.2(b). From Gauss's Law, the opposite surface charges in figure 2.2(b) will generate an electric field

$$\bar{E} = \frac{en_0\,(\xi_e - \xi_i)}{\epsilon_0} \tag{2.11}$$

The force equation for the electrons will be

$$m_e\frac{d^2\xi_e}{dt^2} = -e\bar{E} \tag{2.12}$$

and similarly, the force equation for the ions will be

$$m_i \frac{d^2\xi_i}{dt^2} = e\bar{E} \tag{2.13}$$

The relative displacement between the electrons and ions can be expressed as

$$\xi_r = \xi_e - \xi_i \tag{2.14}$$

Differentiating both sides of (2.14) twice with respect to time and substituting in equations (2.12) and (2.13) gives

$$\frac{d^2\xi_r}{dt^2} = -\left(\frac{m_i + m_e}{m_e m_i}\right) e\bar{E} \tag{2.15}$$

which can be written as

$$\frac{d^2\xi_r}{dt^2} = -\left(\frac{e\bar{E}}{m_r}\right) \tag{2.16}$$

where

$$m_r = \frac{m_e m_i}{m_i + m_e} \tag{2.17}$$

is the reduced mass. Substituting (2.11) into (2.16) gives

$$\frac{d^2\xi_r}{dt^2} = -\omega_p^2 \xi_r \tag{2.18}$$

where

$$\omega_p^2 = \frac{e^2 n_0}{m_r \epsilon_0} = \left(\frac{e^2 n_0}{\epsilon_0 m_e} + \frac{e^2 n_0}{\epsilon_0 m_i}\right) = \left(\omega_{pe}^2 + \omega_{pi}^2\right) \tag{2.19}$$

with ω_p the plasma frequency and ω_{pe} and ω_{pi} the electron and ion plasma frequencies respectively. As $m_i >> m_e$, from (2.19), $\omega_p \approx \omega_{pe}$.

2.3 Sheaths

A charged sheath forms between a plasma and any surface in contact with it. The sheath region is important as the energy gained by ions crossing the sheath determines their IED at the surface and the degree of surface modification which can occur.

In low pressure discharges, the higher temperature of electrons together with their smaller mass results in electrons having a greater thermal velocity than ions. Electrons are lost more rapidly from the plasma and a thin positive sheath region where $n_i > n_e$ forms around the plasma. The plasma gains a positive potential known as the plasma potential (V_p) which acts to confine electrons and accelerate ions across the sheath, balancing the electron and ion flux out of the plasma.

2.3.1 Bohm Sheath Criterion

Due to positive space charge in the sheath, ions require a certain minimum energy to cross the sheath region. This is known as the Bohm sheath criterion and is defined by considering the form of the potential across a sheath of potential $-V_0$ and thickness s as shown in figure 2.3. Assuming that the potential (ϕ) is zero at the plasma sheath edge ($x = 0$), the ion energy at x is given by

$$\frac{1}{2}Mu^2(x) = \frac{1}{2}Mu_s^2 - e\phi(x) \tag{2.20}$$

where M is the ion mass, $u(x)$ is the ion velocity and u_s is the velocity at which ions enter the sheath. Assuming no ions are created in the sheath, the ion density in the sheath ($n_i(x)$) is determined using the continuity of ion flux

$$n_i(x)u(x) = n_{is}u_s \tag{2.21}$$

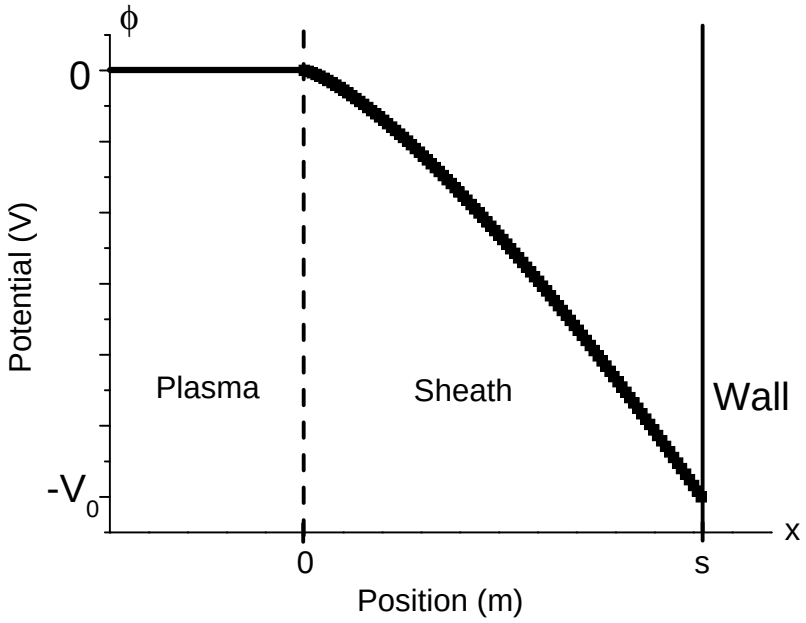

Figure 2.3: Definitions of potential and position for the plasma sheath calculations in section 2.3. The potential at the plasma sheath edge at $x = 0$ is zero and the potential at the wall at $x = s$ is $-V_0$.

where n_{is} is the ion density at the sheath edge. Substitution of (2.21) into (2.20) gives an expression for the ion density

$$n_i(x) = n_{is}\left(1 - \frac{2e\phi(x)}{Mu_s^2}\right)^{-\frac{1}{2}} \tag{2.22}$$

Assuming a Boltzmann distribution, the electron density is given by

$$n_e(x) = n_{es}e^{\frac{\phi}{T_e}} \tag{2.23}$$

where n_{es} is the electron density at the sheath edge. Substituting (2.22) and (2.23) into Poisson's equation gives a relationship between the potential and the electron and ion densities in the sheath

$$\frac{d^2\phi}{dx^2} = \frac{en_s}{\epsilon_0}\left[e^{\frac{\phi}{T_e}} - \left(1 - \frac{2e\phi}{Mu_s^2}\right)^{-\frac{1}{2}}\right] \tag{2.24}$$

where $n_s = n_{es} = n_{is}$ at the sheath edge. Multiplying both sides of (2.24) by $d\phi/dx$ and integrating with respect to x gives

$$\int_0^{\phi} \frac{d\phi}{dx}\frac{d}{dx}\left(\frac{d\phi}{dx}\right)dx = \frac{en_s}{\epsilon_0}\int_0^{\phi}\frac{d\phi}{dx}\left[e^{\frac{\phi}{T_e}} - \left(1-\frac{\phi}{\epsilon_s}\right)^{-\frac{1}{2}}\right]dx \tag{2.25}$$

where $e\epsilon_s = (1/2)Mu_s^2$ is the initial ion energy. Setting $\phi = 0$ and $d\phi/dx = 0$ at $x = 0$, equation (2.25) integrates to

$$\frac{1}{2}\left(\frac{d\phi}{dx}\right)^2 = \frac{en_s}{\epsilon_0}\left[T_e e^{\frac{\phi}{T_e}} - T_e + 2\epsilon_s\left(1-\frac{\phi}{\epsilon_s}\right)^{\frac{1}{2}} - 2\epsilon_s\right] \tag{2.26}$$

For a real solution to exist, the right hand side of (2.26) must be greater than zero. By expressing e^{ϕ/T_e} and $(1-\phi/\epsilon_s)^{\frac{1}{2}}$ as Taylor series expanded to second order, it can be shown that the right hand side of equation (2.26) must satisfy

$$\frac{\phi^2}{2T_e} - \frac{\phi^2}{4\epsilon_s} \geq 0 \tag{2.27}$$

Substituting for ϵ_s, equation (2.27) can be expressed as

$$u_s \geq \left(\frac{eT_e}{M}\right)^{\frac{1}{2}} = u_B \tag{2.28}$$

where u_B is known as the Bohm velocity. For a stable sheath to exist, ions must enter the sheath with a velocity greater than the Bohm velocity.

2.3.2 Presheath

Ions are accelerated to the Bohm velocity across a region called the presheath which has a weak electric field. The potential drop (ϕ_p) across the presheath accelerates ions to the Bohm velocity and can be described by

$$\frac{1}{2}Mu_B^2 = e\phi_p \tag{2.29}$$

Substituting equation (2.28) into (2.29) gives

$$\phi_p = \frac{T_e}{2} \tag{2.30}$$

Within the presheath, the electron and ion densities are equal but less than the densities in the bulk plasma. The presheath densities (n_s) can be determined by substituting (2.30) into (2.23) to give

$$n_s = n_0 e^{-\frac{\phi_p}{T_e}} \approx 0.61 n_0 \tag{2.31}$$

where n_0 is the bulk plasma density.

2.3.3 Floating Potential

The potential of an insulator in a plasma will increase until the incoming fluxes of electrons and ions to its surface are equal. The potential to which the insulator charges is known as the floating potential (ϕ_f). This has important implications in the PIII of insulators where the insulator will eventually charge up to the floating potential during pulse biasing. The floating potential is determined by assuming that the ion and electron flux to the surface are equal when the surface is at the floating potential. The ion flux across the presheath is given by

$$\Gamma_i = n_s u_B \tag{2.32}$$

From kinetic theory, for electrons in thermal equilibrium at temperature T_e, the electron flux to a planar surface is given by

$$\Gamma_e = \frac{1}{4} n_s \bar{v}_e e^{\frac{\phi_f}{T_e}} \tag{2.33}$$

where $\bar{v}_e$ is the mean electron speed given by

$$\bar{v}_e = \left(\frac{8eT_e}{\pi m} \right)^{\frac{1}{2}} \tag{2.34}$$

where m is the electron mass. Equating equations (2.32) and (2.33) and with the substitution of (2.28) and (2.34) for u_B and $\bar{v}_e$ respectively gives

$$n_s \left(\frac{eT_e}{M}\right)^{\frac{1}{2}} = \frac{1}{4} n_s \left(\frac{8eT_e}{\pi m}\right)^{\frac{1}{2}} e^{\frac{\phi_f}{T_e}} \tag{2.35}$$

Solving for the floating potential gives

$$\phi_f = -T_e \mathrm{In} \left(\frac{M}{2\pi m}\right)^{\frac{1}{2}} \tag{2.36}$$

2.3.4 High Voltage Sheaths

For many applications, a large potential exists across the sheath due to a large negative voltage applied to a surface to accelerate ions into it. In these cases, the sheath potential is much larger than T_e and from equation (2.23), n_e can be approximated to zero in the sheath. For this situation, simple equations describing the sheath characteristics can be derived.

Matrix Sheath

The simplest sheath has a uniform ion density (n_i) and zero electron density and is known as the matrix sheath. In plasma immersion ion implantation (PIII), the matrix sheath describes the sheath conditions directly after the pulse has been applied. From Gauss's Law in one dimension

$$\frac{dE}{dx} = \frac{en_i}{\epsilon_0} \tag{2.37}$$

Integration of (2.37) gives the electric field

$$E = \frac{en_i}{\epsilon_0} x \tag{2.38}$$

where $E = 0$ at the plasma sheath boundary at $x = 0$ in figure 2.3. The sheath potential is found by integrating (2.38) with respect to x

$$\phi(x) = -\frac{en_i}{2\epsilon_0}x^2 \tag{2.39}$$

where $\phi = 0$ at $x = 0$. The matrix sheath thickness (s) is determined by setting $\phi = -V_0$ at $x = s$

$$s = \left(\frac{2\epsilon_0 V_0}{en_i}\right)^{\frac{1}{2}} \tag{2.40}$$

Child Law Sheath

In the steady state, the decrease in ion density as ions accelerate across the sheath must be accounted for. Assuming that ions start at the sheath edge with zero velocity, from equation (2.20), the ion energy can be expressed by

$$\frac{1}{2}Mu^2(x) = -e\phi(x) \tag{2.41}$$

Assuming a constant flux across the sheath, the current density (J_0) is given by

$$J_0 = en_i(x)u(x) \tag{2.42}$$

The ion density can be expressed by substitution of (2.41) into (2.42)

$$n_i(x) = \left(\frac{J_0}{e}\right)\left(\frac{-2e\phi}{M}\right)^{-\frac{1}{2}} \tag{2.43}$$

The sheath potential can be described by substituting equation (2.43) into Poisson's equation

$$\frac{d^2\phi}{dx^2} = \left(\frac{-J_0}{\epsilon_0}\right)\left(\frac{-2e\phi}{M}\right)^{-\frac{1}{2}} \tag{2.44}$$

Assuming $d\phi/dx = 0$ at $\phi = 0$ and $\phi = 0$ at $x = 0$, equation (2.44) can be integrated twice with respect to x to give

$$-\phi^{\frac{3}{4}} = \frac{3}{2}\left(\frac{J_0}{\epsilon_0}\right)^{\frac{1}{2}}\left(\frac{2e}{M}\right)^{-\frac{1}{4}} x \tag{2.45}$$

If the wall potential at $x = s$ is given by $\phi = -V_0$, using equation (2.45) the ion current density is

$$J_0 = \frac{4}{9}\epsilon_0\left(\frac{2e}{M}\right)^{\frac{1}{2}}\frac{V_0^{\frac{3}{2}}}{s^2} \tag{2.46}$$

Equation (2.46) is known as the Child law for a space charge limited current in a plane diode. If J_0 is given by

$$J_0 = en_i u_B \tag{2.47}$$

then using equation (2.46), the sheath thickness (s) can be expressed as:

$$s = \frac{\sqrt{2}}{3}\lambda_{De}\left(\frac{2V_0}{T_e}\right)^{\frac{3}{4}} \tag{2.48}$$

Substituting equation (2.46) into (2.45), the sheath potential is given by

$$\phi = -V_0\left(\frac{x}{s}\right)^{\frac{4}{3}} \tag{2.49}$$

To correctly determine the ion density, ions cannot be assumed to start at the sheath edge with zero velocity as was assumed in equation (2.41). Using equation (2.20) with u_s=u_B and equations (2.42) and (2.49), the ion density is equal to

$$n_i(x) = \left(\frac{J_0}{e}\right)\left(u_B^2 + \left(\frac{2eV_0}{M}\right)\left(\frac{x}{s}\right)^{\frac{4}{3}}\right)^{-\frac{1}{2}} \tag{2.50}$$

A graph of sheath potential and ion density as a function of sheath thickness (x/s) is shown in figure 2.4. In PIII, after the application of a pulse bias to the target object, on the timescale of the inverse plasma electron frequency (ω_{pe}^{-1}), a matrix

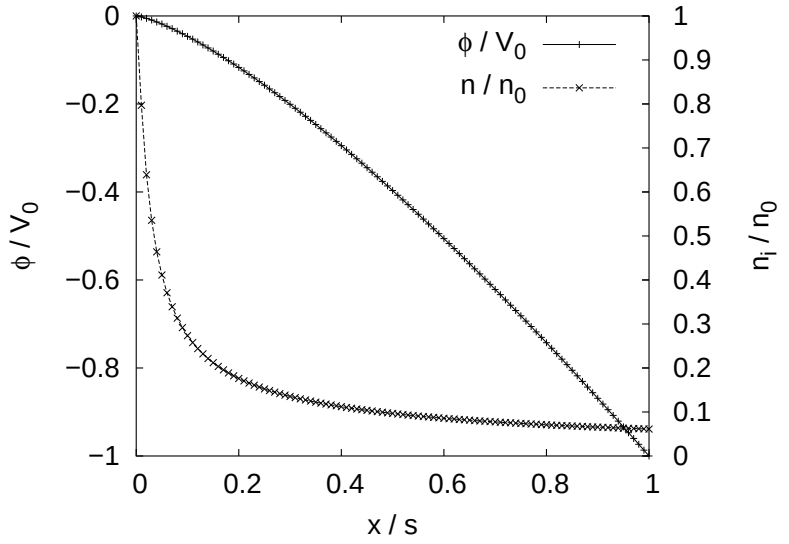

Figure 2.4: Sheath potential (ϕ) and ion density (n_i) as a function of sheath thickness (x/s) for a Child Law sheath determined using equations (2.49) and (2.50). The plasma-sheath edge is at x/s= 0 and the surface being implanted is at x/s= 1.

sheath forms around the object and on the timescale of the inverse plasma ion frequency (ω_{pi}^{-1}), the sheath edge expands outward to eventually reach the Child law sheath thickness.

2.4 Capacitive Discharges

In materials processing, one of the most common plasma sources is radio frequency (RF) discharges. One of the advantages of RF discharges are that insulating materials can be placed on electrodes for deposition or modification. In a DC discharge, an insulator placed on the cathode will act as a capacitor and will charge up positively as it is bombarded by ions. As the insulator surface potential increases, the energy of ions arriving at the surface will decrease which will affect thin film deposition and/or surface modification. In a RF discharge, the positive charge accumulated during one half cycle will be neutralised by electron bombardment during the second half of the cycle reducing the effects of surface charging. RF discharges are also more efficient than DC discharges in sustaining a plasma [20]. This is due to the transfer of energy to plasma electrons from collisions with the oscillating sheath edge and

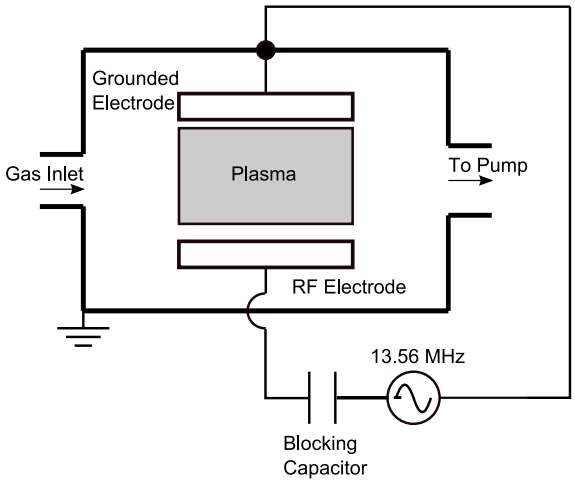

Figure 2.5: Schematic of a typical capacitive radio frequency (RF) discharge driven by parallel plate electrodes.

due to increased electron confinement in the plasma which both increase ionisation in the plasma.

RF discharges can be classified by the means by which power is transferred to the plasma. One of the most commonly used RF systems are capacitively driven discharges where power is transferred to the plasma using electrodes in a vacuum chamber. Other RF plasma sources include high density helicon, helical resonator and other inductive systems which couple RF power to the plasma across dielectric windows. One of the main advantages of these other RF systems is the ability to independently control ion flux and ion energy through separate plasma source and target electrode power supplies. The main advantages of capacitive RF systems are their simplicity of design and the uniformity of the plasma produced between their electrodes. The plasma studied in this thesis was capacitively driven. In this section, an introduction to a simplified homogeneous model [47] is given to describe some of the important physics of the capacitive discharge.

A typical capacitive RF plasma system is shown in figure 2.5. A RF voltage is applied across two parallel electrodes in a vacuum chamber and a plasma is generated between the electrodes using gases fed into the system. The plasma electrons respond to the instantaneous electric field while the ions are slower moving and only respond to the time averaged electric field. The oscillation of the electron cloud results in the

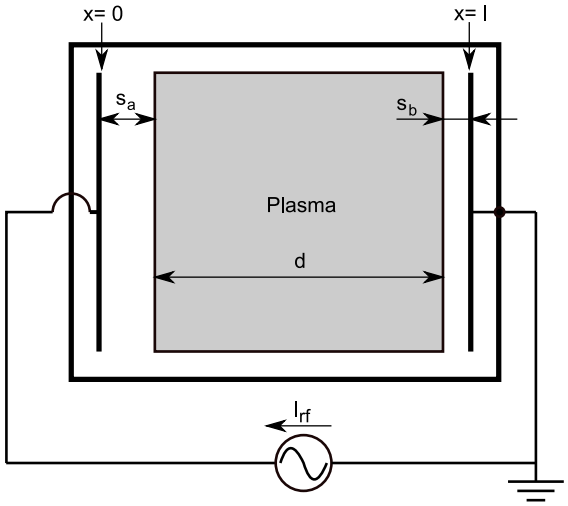

Figure 2.6: A schematic of the plasma and sheaths in the homogeneous capacitive RF discharge model.

formation of sheath regions around the plasma edges. These sheath regions contain a net positive charge which acts to confine electrons and accelerate ions out of the plasma.

2.4.1 Homogeneous Model for Capacitive Discharges

The homogeneous capacitive RF discharge model [47] is shown in figure 2.6. A neutral gas is injected between two electrodes of equal cross sectional area A separated by a distance l. A sinusoidal current, $I_{rf} = Re\left(\bar{I}_{rf}e^{j\omega t}\right)$ flows between the two electrodes. This current generates a plasma with a voltage $V(t)$ across it, ion density $n_i(x,t)$, electron density $n_e(x,t)$ and electron temperature $T_e(x,t)$. Within the bulk plasma, the ion and electron densities are approximately equal while in the sheath region $n_e < n_i$. The instantaneous sheath thickness $s(t)$ and the time averaged sheath thickness $\bar{s}$ are much less than l.

The homogeneous model makes the following assumptions:

1. Due to their larger mass, ions only respond to the time averaged potentials.

2. Due to their smaller mass, electrons respond to the instantaneous potentials

and carry the RF discharge current. This assumption is valid provided

$$\omega_{pe} >> \omega \left(1 + \frac{\upsilon_m^2}{\omega^2}\right)^{\frac{1}{2}}$$

where υ_m is the electron collision rate with neutral molecules.

3. The electron density is zero within the sheath.

4. There is no transverse variation in properties along the electrodes as $l << \sqrt{A}$.

5. The ion density is uniform and constant everywhere in the plasma and sheath. $n_i(x,t) = n =$ constant.

In more complicated models such as those developed by Lieberman [78, 79], a non-uniform ion and electron density is assumed in the sheath which lead to more realistic calculations. However, the homogeneous model is still qualitatively correct and reveals much of the underlying physics.

2.4.2 Bulk Plasma Properties

The bulk plasma has capacitive, resistive and inductive properties. The admittance (Y) of the bulk plasma can be derived by considering the application of an electric field to a uniform plasma in a background gas. The applied electric field is given by

$$E_x(t) = \tilde{E}_x \cos\omega t = Re\left[\tilde{E}_x e^{j\omega t}\right] \tag{2.51}$$

Assuming that ions do not respond to the instantaneous electric field due to their larger mass, only the electron motion will be considered. The force equation for electrons of mass m_e in the absence of magnetic fields is

$$m_e \frac{du_x}{dt} = -eE_x - m_e \upsilon_m u_x \tag{2.52}$$

where u_x is the electron velocity and υ_m is the electron collision rate with neutrals. The second term on the right hand describes the momentum transfer rate due to

collisions with neutrals. If the electron velocity is given by

$$u_x(t) = Re\left[\tilde{u_x} e^{j\omega t}\right] \tag{2.53}$$

substitution of (2.51) and (2.53) into (2.52) gives an expression for the electron velocity amplitude

$$\tilde{u}_x(t) = -\frac{e}{m}\frac{\tilde{E}_x}{j\omega + \upsilon_m} \tag{2.54}$$

The total current density (J_{Tx}) can be written as

$$J_{Tx} = \epsilon_0 \frac{\partial E_x}{\partial t} + J_x \tag{2.55}$$

where the first term on the right hand side is the displacement current and the second term is the conduction current due to free charges. Substitution of (2.51) and $J_0 = -en_0\tilde{u}_x$ for the electron conduction current into (2.55) gives

$$\tilde{J}_{Tx} = j\omega\epsilon_0\tilde{E}_x - en_0\tilde{u}_x \tag{2.56}$$

Substituting (2.54) into (2.56) and rearranging gives

$$\tilde{J}_{Tx} = j\omega\epsilon_0\left[1 - \frac{\omega_{pe}^2}{\omega\left(\omega - j\upsilon_m\right)}\right]\tilde{E}_x \tag{2.57}$$

which can be expressed as

$$\tilde{J}_{Tx} = j\omega\epsilon_p\tilde{E}_x \tag{2.58}$$

where

$$\epsilon_p = \epsilon_0\left[1 - \frac{\omega_{pe}^2}{\omega\left(\omega - j\upsilon_m\right)}\right] \tag{2.59}$$

is an effective plasma dielectric constant. Equation (2.57) can also be written in the form

$$\tilde{J}_{Tx} = \left(\sigma_p + j\omega\epsilon_0\right)\tilde{E}_x \tag{2.60}$$

where

$$\sigma_p = \frac{\epsilon_0\omega_{pe}^2}{j\omega + \upsilon_m} \tag{2.61}$$

is the plasma conductivity. Depending on the conditions, equations (2.59) or (2.61) can be used to describe the plasma as having either the properties of a dielectric or a conductor.

The admittance (Y_p) of a bulk plasma slab of length $d = l - 2\bar{s}$ can be expressed as

$$Y_p = \frac{j\omega\epsilon_p A}{d} \tag{2.62}$$

Substitution of (2.59) into (2.62) allows the bulk plasma to be expressed in the form of an equivalent electrical circuit model

$$Y_p = j\omega C_0 + \frac{1}{j\omega L_p + R_p} \tag{2.63}$$

where $C_0 = \epsilon_0 A/d$ is the vacuum capacitance, $L_p = 1/\omega_{pe}^2 C_0$ is the plasma inductance and $R_p = \upsilon_m L_p$ is the plasma resistance. Equation (2.63) represents the bulk plasma as a capacitor in parallel with the series combination of an inductor and a resistor. This is illustrated in figure 2.7 along with circuit elements for the sheaths which will be discussed in section 2.4.3.

The displacement current through C_0 is much smaller than the conduction current through L_p and R_p. Using (2.63), the current through C_0 is given by

$$I_C = \left(\frac{\omega^2\left(1 - \frac{j\upsilon_m}{\omega}\right)}{\omega^2\left(1 - \frac{j\upsilon_m}{\omega}\right) - \omega_{pe}^2}\right) I_{rf} \tag{2.64}$$

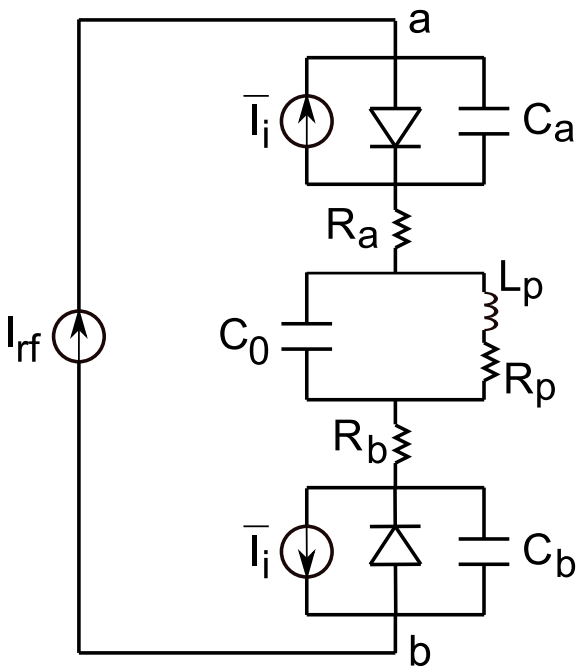

Figure 2.7: Equivalent circuit model of a homogeneous RF capacitive discharge. The bulk plasma is represented as a capacitor (C_0) in parallel with the series combination of an inductor (L_p) and a resistor (R_p). The ion flow across the sheaths are represented by the two current sources ($\bar{I}_i$) and the flow of electrons are represented by the two diodes. The sheath capacitances are represented by C_a and C_b and the resistors R_a and R_b represent energy gained by plasma electrons due to stochastic heating.

where I_{rf} is the total current. The current through L_p and R_p is given by

$$I_{LR} = \left(\frac{-\omega_{pe}^2}{\omega^2 \left(1 - \frac{j\upsilon_m}{\omega}\right) - \omega_{pe}^2} \right) I_{rf} \tag{2.65}$$

From assumption (2) in section 2.4.1, $\omega_{pe} >> \omega \left(1 + \frac{\upsilon_m^2}{\omega^2}\right)^{\frac{1}{2}}$, which gives $I_{LR} \approx I_{rf}$ and $I_C \approx 0$.

The dielectric constant of the bulk plasma (ϵ_p) is much larger than that of the sheath region (ϵ_0) and very little of the RF voltage is dropped across the bulk plasma. From (2.58), the electric field in the bulk plasma is given by

$$\tilde{E}_{x(plasma)} = \frac{\tilde{J}_{Tx}}{j\omega\epsilon_p} \tag{2.66}$$

As will be discussed in section 2.4.3, the majority of current in the sheath is dis-

placement current. As a result, the second term on the right hand side of (2.56) is approximately zero and

$$\tilde{E}_{x(sheath)} = \frac{\tilde{J}_{Tx}}{j\omega\epsilon_0} \tag{2.67}$$

where $\tilde{J}_{Tx}$ has been assumed to be constant across the bulk and sheath regions. As $\epsilon_p >> \epsilon_0$, the electric field in the bulk plasma will be much smaller than across the sheath and the majority of the RF voltage is dropped across the sheath regions.

2.4.3 Sheath Properties

In the sheath, the majority of current is displacement current which is caused by time varying electric fields. The conduction current, which is mostly made up of electrons, is much smaller in the sheath due to the reduced electron density in this region. The conduction current due to ion flow is also much less than the displacement current but is important for the modification of materials at the electrodes.

Displacement Current

The equations describing the displacement current through the sheath can be used to derive equations for the sheath voltage waveforms. Using Poisson's equation, the electric field $E = \bar{E}_x$ in sheath a in figure 2.6 is given by

$$\frac{dE}{dx} = \frac{en}{\epsilon_0} \tag{2.68}$$

where n is the charged particle density in the sheath. Integration of (2.68) gives the electric field

$$E(x,t) = \frac{en}{\epsilon_0}\left[x - s_a(t)\right] \tag{2.69}$$

where $s_a(t)$ is the plasma-sheath edge and $E \approx 0$ at $x = s_a$. If the conduction current through the sheath is very small then the second term on the right hand side of (2.55) is approximately zero. The displacement current through the sheath

is

$$I_{ap}(t) = \epsilon_0 A \frac{\partial E}{\partial t} \tag{2.70}$$

where A is the sheath cross sectional area. Substituting (2.69) into (2.70) gives

$$I_{ap}(t) = -enA \frac{ds_a}{dt} \tag{2.71}$$

If $I_{ap}(t) = I_{rf}(t) = I_1 \cos(\omega t)$, integration of (2.71) gives

$$s_a(t) = \bar{s} - s_0 \sin(\omega t) \tag{2.72}$$

where $\bar{s}$ is the DC value of the sheath thickness and

$$s_0 = \frac{I_1}{en\omega A} \tag{2.73}$$

is the sheath oscillation amplitude. Integration of (2.69) gives the voltage across the sheath

$$V_{ap}(t) = \int_0^{s_a} E dx = -\left(\frac{en}{\epsilon_0}\right)\left(\frac{s_a^2}{2}\right) \tag{2.74}$$

Substitution of (2.72) into (2.74) gives

$$V_{ap}(t) = -\left(\frac{en}{2\epsilon_0}\right)\left(\bar{s}^2 - 2\bar{s}s_0 \sin\omega t + \frac{s_0^2}{2} - \frac{s_0^2}{2}\cos 2\omega t\right) \tag{2.75}$$

The time averaged value for V_{ap} is given by

$$\bar{V}_{ap} = \frac{1}{T}\int_0^T V_{ap}(t)dt = -\frac{en}{2\epsilon_0}\left(\bar{s}^2 + \frac{s_0^2}{2}\right) \tag{2.76}$$

Similarly, for sheath b in figure 2.6, the displacement current through the sheath is given by

$$I_{bp}(t) = -enA \frac{ds_b}{dt} \tag{2.77}$$

and the voltage across the sheath is given by

$$V_{bp}(t) = \left(\frac{en}{\epsilon_0}\right)\left(-\frac{s_b^2}{2}\right) \tag{2.78}$$

By continuity of current

$$I_{bp} + I_{ap} = 0 \tag{2.79}$$

Substitution of (2.71) and (2.77) into (2.79) gives

$$s_a + s_b = constant = 2\bar{s} \tag{2.80}$$

Substitution of (2.72) into (2.80) gives

$$s_b = \bar{s} + s_0 \sin \omega t \tag{2.81}$$

The sheath voltage $V_{bp}(t)$ is given by substituting (2.81) into (2.78)

$$V_{bp}(t) = -\frac{en}{2\epsilon_0}\left(\bar{s}^2 + 2\bar{s}s_0 \sin \omega t + \frac{s_0^2}{2} - \frac{s_0^2}{2}\cos 2\omega t\right) \tag{2.82}$$

The time averaged value for $V_{bp}(t)$ is given by

$$\bar{V}_{bp} = \frac{1}{T}\int_0^T V_{bp}(t)dt = -\frac{en}{2\epsilon_0}\left(\bar{s}^2 + \frac{s_0^2}{2}\right) \tag{2.83}$$

The combined voltage across both sheaths $V_{ab} = V_{ap} - V_{bp}$ is given by

$$V_{bp}(t) = \left(\frac{2en\bar{s}s_0}{\epsilon_0}\right)\sin \omega t \tag{2.84}$$

A graph of the sheath voltages $V_{ap}(t)$ and $V_{pb}(t) = -V_{bp}(t)$ are given in figure 2.8 along with their time averaged values $\bar{V}_{ap}$ and $\bar{V}_{pb}$.

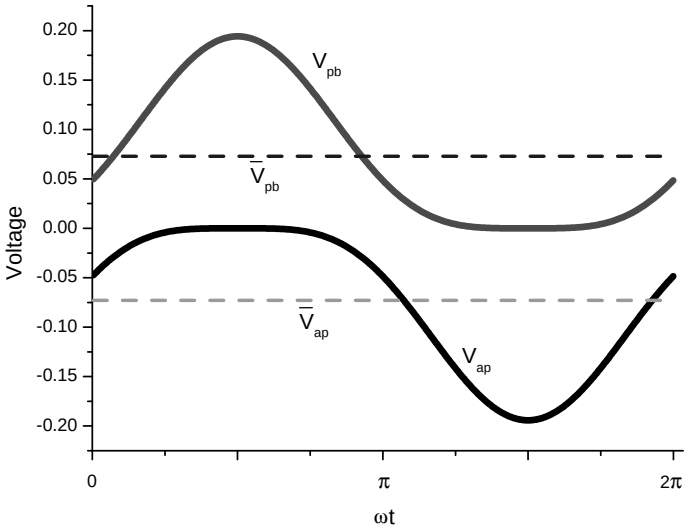

Figure 2.8: Sheath voltages $V_{ap}(t)$ and $V_{pb}(t) = -V_{bp}(t)$ and their time averaged values obtained using the homogeneous capacitive discharge model.

Conduction Current

The conduction current in the sheath is very small due to the reduced electron density in the sheath. However, the balance between ion and electron conduction currents in the sheath determines the average sheath thickness $\bar{s}$. By assumption (1), there is a steady ion current flow through the sheath given by

$$\bar{I}_i = enu_b A \tag{2.85}$$

Over one RF period the total current flow to each electrode must sum to zero. In the homogeneous model the electron density in the sheath is zero so the thickness of each sheath must collapse to zero at some time in each period to allow electron transfer to the electrodes. For sheath a, setting $s_a(t) = 0$ in (2.72) gives

$$\bar{s} = s_0 = \left(\frac{I_1}{en\omega A}\right) \tag{2.86}$$

Substitution of (2.86) into (2.75) gives

$$V_{pa} = -V_{ap} = \left(\frac{en}{2\epsilon_0}\right) s_0^2 \left(1 - \sin\omega t\right)^2 \tag{2.87}$$

The electron transfer from the plasma to the electrodes occurs when the sheath voltage collapses to zero and can be represented in the circuit diagram in figure 2.7 as a diode, forward biased into the plasma.

The linear sheath capacitance (C_s) can be obtained by differentiating (2.84) and substituting in (2.86)

$$\frac{dV_{ab}}{dt} = \left(\frac{2s_0 I_1}{\epsilon_0 A}\right) \cos \omega t \tag{2.88}$$

Rearrangement of (2.88) gives

$$I_{rf} = C_s \left(\frac{dV_{ab}}{dt}\right) \tag{2.89}$$

where C_s is the linear sheath capacitance given by

$$C_s = \left(\frac{\epsilon_0 A}{2s_0}\right) \tag{2.90}$$

The capacitance C_s is represented in figure 2.7 as the series combination of two non linear capacitances $C_a = \epsilon_0 A/s_a(t)$ and $C_b = \epsilon_0 A/s_b(t)$. The ion current sources across both sheaths in figure 2.7 represent ion flow across the sheath. The two resistors R_a and R_b represent energy gained by electrons through stochastic heating which occurs when electrons are reflected by the moving high voltage sheaths which act to confine electrons in the plasma and increase their energy.

2.4.4 Asymmetric Discharges

In most capacitive discharges, the area of the RF powered electrode is smaller than the area of the grounded electrode which includes the grounded chamber walls. This asymmetry will cause a DC self bias to develop at the RF electrode.

The magnitude of this bias can be determined by considering the capacitance of each sheath and the current across it. If the sheath is approximated to be a parallel plate capacitor, its capacitance (C) can be written as

$$C = \frac{Q}{V} = \frac{\epsilon_0 A}{d} \tag{2.91}$$

where A is the electrode area, Q is the charge on the electrode, V is the voltage and d is the sheath thickness. As the area of the electrode increases, the sheath capacitance will increase and the voltage drop across the sheath will decrease. If the area of the two electrodes a and b in figure 2.6 are given by A_a and A_b respectively, from (2.91) the current density through sheath a can be expressed with the following proportionality

$$J_{a1}(\mathbf{x}) \propto \frac{\bar{V}_a}{s_a(\mathbf{x})} \tag{2.92}$$

From equation (2.46) for the Child law

$$J_{a1}(\mathbf{x}) \propto n_a(\bar{x}) \propto \frac{\bar{V}_a^{\frac{3}{2}}}{s_a^2(\mathbf{x})} \tag{2.93}$$

The total RF current to electrode a can be expressed as

$$I_{a1} = \int_{A_a} J_{a1}(\mathbf{x}) d^2x \tag{2.94}$$

Substitution of (2.92) and (2.93) into (2.94) gives

$$I_{a1} = \bar{V}_a^{\frac{1}{4}} \int_{A_a} n_a^{\frac{1}{2}}(\mathbf{x}) d^2x \tag{2.95}$$

Similarly for electrode b

$$I_{b1} = \bar{V}_b^{\frac{1}{4}} \int_{A_b} n_b^{\frac{1}{2}}(\mathbf{x}) d^2x \tag{2.96}$$

For RF current continuity $I_{a1} = I_{b1}$ which gives

$$\frac{\bar{V}_a^{\frac{1}{4}}}{\bar{V}_b^{\frac{1}{4}}} = \frac{\int_{A_b} n_b^{\frac{1}{2}} d^2x}{\int_{A_a} n_a^{\frac{1}{2}} d^2x} \tag{2.97}$$

If the ion density is equal in both sheaths, $n_a = n_b$, which gives

$$\frac{\bar{V}_a}{\bar{V}_b} = \left(\frac{A_b}{A_a}\right)^4 \tag{2.98}$$

The effects of asymmetric electrodes are illustrated in figure 2.9 using the sheath voltage waveforms derived in section 2.4.3. Due to the higher mobility of the plasma electrons, the plasma potential must remain more positive than the RF electrode and the grounded walls. In a symmetric system (figure 2.9(a)), the DC bias developed at the RF electrode and grounded electrode are equal. For a system where the RF electrode is much smaller than the grounded electrode (figure 2.9(b)), the situation encountered in this thesis, a self bias forms at the RF electrode. This results in the potential between the plasma and the grounded electrode being smaller than the potential between the plasma and the RF electrode (V_p - V_{RF}). More detailed experimental studies of sheath voltages in asymmetric discharges can be found in the literature [66, 108].

The scaling power of four in (2.98) is much larger than seen in experiments where the power is typically less than 2.5 [81]. Two reasons for this discrepency are that in real plasmas the ionisation rate in the RF electrode sheath is greater than in the grounded sheath making $n_a \neq n_b$ as was assumed to obtain (2.98). Ion collisions in the sheath would also modify equation (2.93) which would reduce the scaling power.

2.5 Ion Energy Distributions

In plasma processing, the energy of ions arriving at a surface is important in determining the structure of deposited films and the degree of surface modification. In this thesis, ion energy distribution (IED) measurements are made during mesh assisted plasma immersion ion implantation (PIII). In this section, a discussion of the factors affecting the IED is given along with an analytical model for determining the IED.

Energy is gained by ions as they cross the plasma sheath. In RF plasmas, the energy gained by ions crossing the sheath is determined by the amplitude of the sheath voltage, the pressure and the relationship between the time taken for an ion to cross the sheath (τ_{ion}) and the RF period (τ_{RF}) [59]. The pressure determines the number of collisions an ion experiences and the relationship between τ_{ion} and τ_{RF} determines the potential difference experienced by ions crossing the sheath. As will

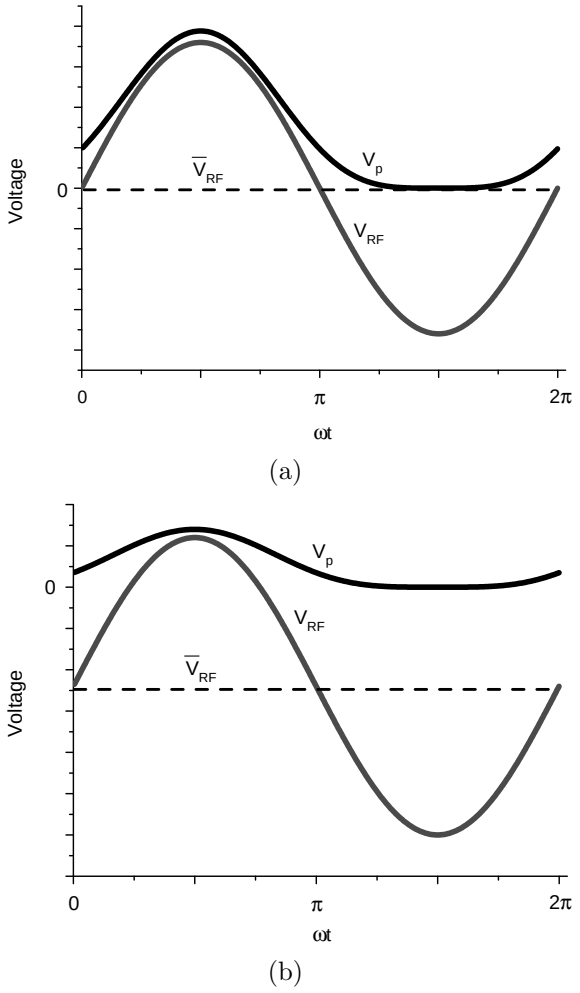

Figure 2.9: Plasma potential (V_p), RF electrode potential (V_{RF}) and mean RF potential ($\bar{V}_{RF}$) for a capacitive discharge with (a) symmetric electrodes and (b) asymmetric electrodes where the RF electrode is much smaller than the grounded electrode.

be discussed in chapter 4, IEDs can be measured experimentally using mass spectrometer systems or electrostatic energy analysers. IEDs have also been calculated using analytical models [9, 59], using the numerical integration of the equations of motion [147, 90], using Monte Carlo methods to account for ion collisions [85, 63] and using particle in cell methods [45, 153].

Analytical IED models [9, 59] for collisionless RF sheaths are useful in describing the factors which determine the IED. If the time taken by ions to cross the sheath (τ_{ion}) is much less than the RF period (τ_{RF}), the energy of the ions arriving at the target will vary, depending on the sheath voltage at the time the ion entered

the sheath. This is known as the low frequency case, where $\tau_{ion} << \tau_{RF}$. For the collisionless low frequency case, the IED will have a width corresponding to the range of values of the sheath voltage. Peaks will occur at the maximum and minimum sheath voltage where the sheath potential changes most slowly. If $\tau_{ion} >> \tau_{RF}$ the ions will take many RF periods to cross the sheath and will experience the time averaged value of the sheath potential. This is known as the high frequency case. The IED produced will be narrower than for the low frequency case and as τ_{ion} increases, the separation between the two peaks will decrease.

In the high frequency case, the time taken by an ion to cross a RF sheath can be estimated using the Child-Langmuir law. From (2.45), the sheath potential (V_s) can be expressed as

$$V_s = C_1 x^{\frac{4}{3}} \tag{2.99}$$

where

$$C_1 = \left(\frac{9J_0}{4\epsilon_0}\right)^{\frac{2}{3}} \left(\frac{M}{2e}\right)^{\frac{1}{3}} \tag{2.100}$$

If the initial ion velocity at the sheath edge is neglected, the velocity of the ion in the sheath ($v(x)$) can be determined by equating the ion's kinetic energy ($(1/2)Mv(x)^2$) to its electrical potential energy (eV_s) to give

$$v(x) = \left(\frac{2eV_s(x)}{M}\right)^{\frac{1}{2}} \tag{2.101}$$

The time taken by the ion to cross the sheath is given by

$$\tau_{ion} = \int_0^{\bar{s}} \frac{dx}{v(x)} \tag{2.102}$$

where $\bar{s}$ is the time averaged sheath thickness given by (2.48). Substitution of (2.99) and (2.101) into (2.102) gives

$$\tau_{ion} = 3\bar{s} \left(\frac{M}{2e\bar{V}_s}\right)^{\frac{1}{2}} \tag{2.103}$$

where $\bar{V}_s$ is the mean sheath voltage. The argon plasmas studied in this thesis were driven with RF power sources in the high frequency regime with a signal frequency of 13.56 MHz and sheath voltages between -20 to -420 V while the power supply used to simulate PIII was operated in the low frequency regime.

2.5.1 Analytical Model

For the high frequency case, an analytical model for the IED in a collisionless RF sheath has been derived [9]. The assumptions of the model are

1. A constant sheath width.
2. A uniform sheath electric field.
3. A sinusoidal sheath voltage given by $V_s(t) = \bar{V}_s + \tilde{V}_s \sin \omega t$.
4. Ions enter the sheath with zero velocity.

The expression for the IED is given by

$$f(E) = \frac{dn}{dE} = \frac{2n_t}{\omega \Delta E_i} \left[1 - \frac{4}{\Delta E_i^2} \left(E - e\bar{V}_s \right)^2 \right]^{-\frac{1}{2}} \tag{2.104}$$

where n_t is the number of ions entering the sheath per unit time and ΔE_i is the IED width given by

$$\Delta E_i = \frac{2e\tilde{V}_s}{\bar{s}\omega} \left(\frac{2e\bar{V}_s}{M} \right)^{\frac{1}{2}} = \frac{3e\tilde{V}_s}{\pi} \left(\frac{\tau_{RF}}{\tau_{ion}} \right) \tag{2.105}$$

Equation (2.104) is obtained by integrating the equation of motion for ions in the sheath using the assumption that $\tau_{ion} >> \tau_{RF}$. IEDs obtained using the analytical model for $\tilde{V}_s$ values of 20 and 50 V are shown in figure 2.10, for a 13.56 MHz RF argon plasma with $n_t = 1000$, $T_e = 3$ eV and $\bar{V}_s = 100$ V. Even though the ions take more than ten RF periods to cross the sheath, two peaks at the maximum and minimum values of the IED are observed as the sheath potential changes most slowly near its maximum and minimum values. The energy difference between the peaks is much smaller than the sinusoidal component of the sheath voltage ($\tilde{V}_s$)

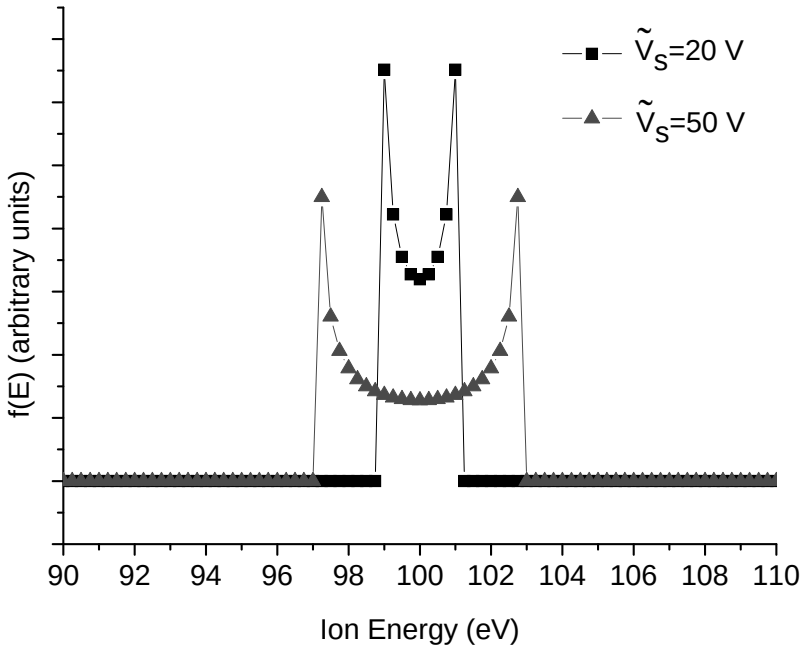

Figure 2.10: IEDs obtained using the analytical model for $\tilde{V_s}$ values of 20 and 50 V in a 13.56 MHz argon plasma with $n_t = 1000$, $T_e = 3$ eV and $\bar{V_s} = 100V$.

and becomes less as the time taken by the ions to cross the sheath becomes larger. As $\tilde{V_s}$ increases, the IED width increases as the ions experience a greater range of potentials in the sheath. In experimental IED measurements, ions enter the sheath with a range of velocities greater than the Bohm velocity and this, along with ion collisions in the sheath will broaden the IED.

2.6 Summary

In this chapter, an introduction to the plasma and discharge physics relevant to this thesis has been given. A plasma is a partially ionised gas made up of an approximately equal number of ions and electrons and a different number of neutrals. Plasmas have important applications in materials deposition and in the modification of surfaces.

The Debye length, mean free path and plasma frequency are important parameters used to describe a plasma. The Debye length is dependent on the charged particle density and electron temperature and describes how effectively a plasma

shields a potential perturbation. Collisional processes determine the energy of particles in a plasma and the average distance between collisions for a particle in a plasma is described by its mean free path. In an applied electric field, the charged particles in a plasma will oscillate. The natural frequency of these oscillations is determined by the electron and ion plasma frequencies and these provide an important timescale for describing effects in a plasma.

Due to the higher mobility of electrons, a positively charged sheath region forms around the outside of a plasma at its boundaries with electrodes and the vacuum vessel. For high voltages such as those imposed by PIII electrodes, this sheath can be described using the Child law. The energy gained by ions crossing the sheath determines their IED.

In materials processing there are a number of different methods of generating plasmas. In this project, a capacitive RF discharge where a plasma is generated by applying an electric field across two parallel plate electrodes was used. The majority of the voltage is dropped across the sheath regions where the displacement current is much larger than the conduction current. In asymmetric systems where the area of the grounded electrode is much larger than the area of the RF electrode, a significant DC bias develops at the RF electrode.

In RF plasmas the IED is determined by the sheath voltage, pressure and relationship between the time taken for the ion to cross the sheath (τ_{ion})and the RF period (τ_{RF}). If τ_{ion} is much less than τ_{RF}, the potential experienced by the ion will depend on the time at which the ion entered the sheath. This will produce a wide bimodal IED. If τ_{ion} is much greater than τ_{RF}, the ion will experience the time averaged sheath voltage. This will produce a narrower IED centred around the mean sheath voltage.

Chapter 3

Plasma Immersion Ion Implantation (PIII)

3.1 Introduction

In this chapter, an introduction to plasma immersion ion implantation (PIII) and ion energy measurements during PIII is given. In section 3.2, the PIII method is introduced and in section 3.3, examples of its use in the surface treatment of metals, semiconductors and insulators are discussed. In section 3.4, an analytical model developed by Lieberman [80] is presented to illustrate some of the important features of the transient sheath during PIII. In section 3.5, a review of ion dose and energy measurements during PIII using both simulation and experiment is given.

3.2 Plasma Immersion Ion Implantation

Since its introduction in the nineteen eighties [27], plasma immersion ion implantation (PIII) has become a widely used technique for the surface modification of metals, semiconductors and insulators. The basic PIII process is shown in figure 3.1(a). A negative voltage pulse with an amplitude of up to -150 kV and a period of between one to several hundred microseconds is applied to an object immersed in a plasma [148]. Plasma ions are accelerated across the sheath and are implanted into the object.

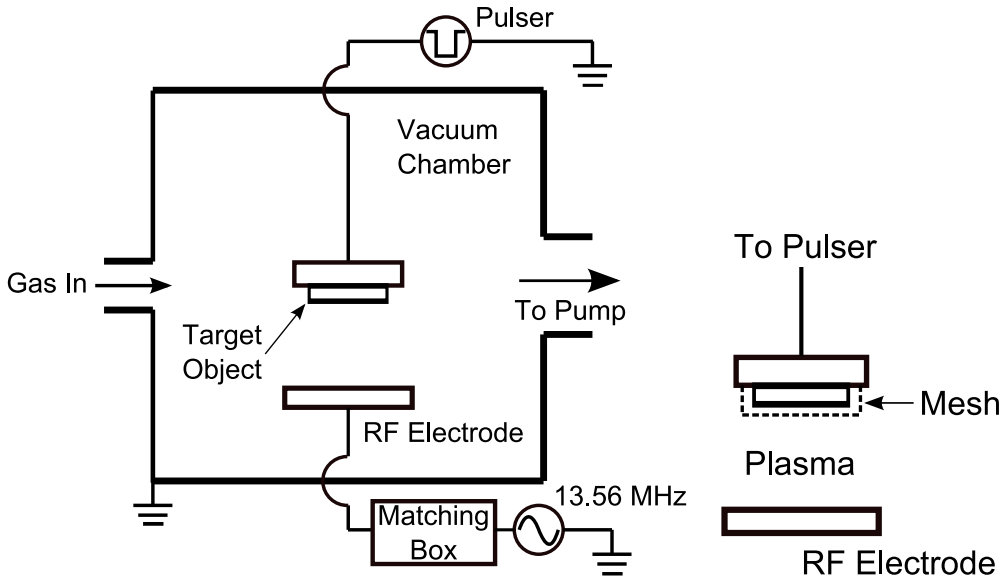

(a) Basic PIII setup (b) Mesh assisted PIII

Figure 3.1: (a) In the basic PIII process, a large negative voltage pulse is applied to a target object immersed in a plasma. (b) When the target object is an insulator, a conductive mesh can be used to minimise surface charging effects.

Compared to conventional beamline ion implantation, PIII has several advantages. In beamline ion implantation, a thin beam of ions is extracted from a plasma source, focused and accelerated onto the object whose surface is to be modified. The beam and/or object are then moved to expose the area requiring treatment. In PIII, the entire object is immersed in the plasma and all exposed surfaces undergo treatment at the same time. This allows objects with complex shapes, such as drill bits [138], to be treated quickly without the need for object manipulation. Immersion in a plasma also allows charge build up during implantation to be neutralised during the pulse-off periods. During pulse-off periods, PIII can also be combined with deposition processes.

While PIII provides a quick and simple surface treatment method it has some limitations. PIII is not mass selective and all plasma ions are accelerated into the target object. Due to ion collisions in the sheath and the finite rise and fall time of the pulse, the implantation energy of ions into the object will be inhomogeneous. The minimum feature size to be treated must also be of the order of the sheath width to allow the plasma sheath to mold over the surface.

3.3 Applications of PIII

PIII has been used in the treatment of metals, semiconductors and insulators [104]. The PIII treatment of metals such as stainless steel, chromium and alloys has been shown to improve resistance to wear and corrosion [26, 142, 86]. The depth of surface modifications is usually less than 100 nm but can be increased by heating, such as in the implantation of nitrogen into stainless steel at temperatures of around 400 °C [11, 77].

PIII has been used in the treatment of semiconductors such as silicon to modify optical, electrical and magnetic properties [114, 136, 104]. This process can produce layers of nanometre thickness with very different properties to the bulk material such as in the implantation of nitrogen into aluminium which produces semiconductor aluminium nitride surfaces [89]. The ability of PIII to produce shallow layers with different properties has also been used in the fabrication of p-n junction diodes by incorporating ions of atoms such as boron or arsenic into silicon [58, 73].

PIII has been used to improve the mechanical [33], wetability [43, 65], adhesive [50] and gas barrier [102] properties of polymer films. This has important applications in areas such as food packaging and in biomedicine where improved hydrophilic properties can improve the lifetime of attached proteins [100]. Unlike metals, where charge build up can be conducted away, the PIII treatment of insulators results in positive charge accumulation on the surface during the pulse-on period. This increases the potential on the insulator surface and reduces the energy of implanted ions. The deposition of a thin sacrificial metal layer on the polymer surface has been used to overcome this problem [101]. The pulse bias is applied to the metal layer and plasma ions are implanted through the layer into the polymer. Another method of overcoming this problem is by placing a conductive mesh around the sample, as shown in figure 3.1(b)[93], and pulse biasing both the mesh and substrate with the same pulse. The negatively biased mesh returns secondary electrons released from the insulator surface due to ion bombardment, helping to minimise surface charging. This method has been used to improve the PIII treatment of materials including polystyrene [67], quartz [44], polyurethane [24] and silicon carbide [42].

PIII can be combined with thin film deposition in a process known as plasma immersion ion implantation and deposition (PIIID). Deposition occurs during pulse-off periods and implantation occurs during pulse-on periods. PIIID allows a graded transition layer to be formed between the thin film and substrate and this improves film adhesion. Examples of PIIID can be found in the production of metal and metal sulfide coatings [50, 145] and diamond like carbon (DLC) films [130, 144, 72]. The hardness and chemical inertness of DLC films gives them many applications in the coating of parts for industrial and medical use.

PIII can also be combined with cathodic arc deposition of metal ions in a process known as metal plasma immersion ion implantation (MePIIID) [3]. A metal plasma is generated when an arc discharge is created between two electrodes in a vacuum. The arc produces a plasma from the cathode material and also releases neutral liquid macroparticles. The macroparticles can be removed using a curved magnetic filter which directs plasma ions to the substrate and does not alter the trajectories of neutrals. Metal film deposition occurs during times when a high voltage pulse is not being applied to the substrate and implantation occurs during pulse-on periods. The implantation of metals such as titanium, tantalum, molybdenum and tungsten using MePIIID hardens metals [18, 157]. A variety of thin films have also been formed including titanium nitrides and oxides with potential medical applications [52, 137], tantalum oxides [156] and chromium films [16]. MePIIID has also been used for the treatment of polymers such as copper implantation into polyethylene [159]. Through the control of parameters such as pulse amplitude and frequency, MePIIID allows thin films with tailored properties such as low stress and increased hardness to be grown [4].

While PIII is usually carried out with pulse amplitudes in the kilovolt range, there are also applications with pulse amplitudes below -1000 V. PIII and PIIID in this voltage range improves surface properties without generating significant defects in the surface layers. Shallow junction doping of silicon with boron and phosphorous has been carried out with pulse amplitudes between -700 and -800 V [106]. DLC films have also been deposited using pulse amplitudes between -50 and -300 V in acetylene plasmas [131, 75]. The DLC films produced showed increased hardness

and compressive stress compared to films made using RF biasing of the substrate. The effects of pulse frequency have been studied during -100 V pulse bias sputtering of copper onto silicon dioxide [6]. Increasing the pulse frequency from 20 Hz to 10 kHz while keeping the duty cycle constant reduced the time for surface charge accumulation and increased the average energy of the ion flux. The use of pulse biasing provides greater control of the average ion energy which is an important factor in determining film properties. Mesh assisted PIII with pulse amplitudes between -200 and -400 V has also been performed on polyurethane [24]. The use of a conductive grid was shown to reduce surface charging effects and to improve surface roughness and adhesive properties.

3.4 Collisionless Transient Sheath PIII Model

In this section, an analytical model developed by Lieberman [80] for a planar, collisionless, transient sheath is introduced to illustrate the nature of the ion dose and energy distribution during PIII.

As shown in figure 3.2, when a negative voltage pulse ($-V_0$) is applied to an object immersed in a plasma, on the timescale of the inverse electron plasma frequency (ω_{pe}^{-1}), electrons near the object are repelled away. This leaves a uniform density ion matrix sheath with thickness s_0 given by equation (2.40). On the timescale of the inverse ion plasma frequency (ω_{pi}^{-1}), the matrix sheath ions are accelerated into the surface which drives the plasma-sheath edge further back to expose more ions to be extracted. On a timescale much greater than the inverse ion plasma frequency, the sheath width approaches the steady state Child law sheath thickness given by equation (2.48). The time evolution of the sheath determines the current density and energy distribution of the implanted ions.

The assumptions of the model are:

1. The ion flow is collisionless.

2. Electrons have zero mass and respond instantly to the applied potentials. This is valid as the timescale of interest is much greater than ω_{pe}^{-1}.

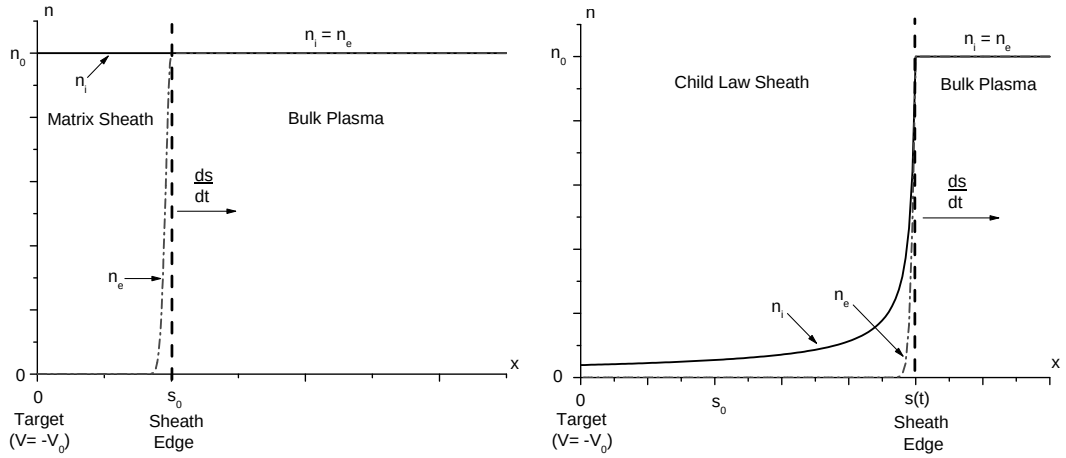

(a) Ion Matrix Sheath (b) Child Law Sheath

Figure 3.2: Ion (n_i) and electron (n_e) densities after the application of a negative voltage pulse ($-V_0$). (a) On the timescale of the inverse plasma electron frequency (ω_{pe}^{-1}), an ion matrix sheath forms. (b) On a timescale much greater than the inverse ion plasma frequency (ω_{pi}^{-1}), a Child Law sheath forms.

3. The applied voltage ($-V_0$) is much greater than T_e so that $\lambda_{De} << s_0$.

4. After the ion matrix sheath formation, a Child law sheath forms. The current for this sheath is supplied by the uncovering of ions at the moving sheath edge.

5. Ions cross the sheath instantly so that the implantation current equals the charge uncovered by the expanding sheath.

6. Ions are singly charged.

3.4.1 Sheath Edge Motion

The Child law current density (j_c) for a potential V_0 across a sheath of thickness s is given by equation (2.46)

$$j_c = \frac{4}{9}\epsilon_0 \left(\frac{2e}{M}\right)^{\frac{1}{2}} \frac{V_0^{\frac{3}{2}}}{s^2} \tag{3.1}$$

where ϵ_0 is the permittivity of free space, M is the ion mass and e is the ion charge. The amount of charge crossing the moving sheath edge is equated to the Child law

current density

$$en_0\left(\frac{ds}{dt}+u_B\right)=j_c \tag{3.2}$$

where u_B is the Bohm velocity given by equation (2.28) and ds/dt is the sheath edge velocity. Substitution of (3.1) into (3.2) gives an expression for the sheath edge velocity

$$\frac{ds}{dt}=\frac{2}{9}\left(\frac{s_0^2u_0}{s^2}\right)-u_B \tag{3.3}$$

where s_0 is the matrix sheath thickness given by equation (2.40) and u_0 is the ion velocity given by

$$u_0=\left(\frac{2eV_0}{M}\right)^{\frac{1}{2}} \tag{3.4}$$

Rearrangement of equation (3.3) gives

$$\int dt=\int\frac{9s^2}{2s_0^2u_0-9s^2u_B}ds \tag{3.5}$$

Using the substitution $s=A\text{sec}\,\theta$ and the identity

$$\tanh^{-1}\left(\frac{s}{A}\right)=\frac{1}{2}\log\left(\frac{A+s}{A-s}\right) \tag{3.6}$$

integration of (3.5) gives

$$\tanh^{-1}\left(\frac{s}{s_c}\right)-\frac{s}{s_c}=\frac{u_Bt}{s_c}+\tanh^{-1}\left(\frac{s_0}{s_c}\right)-\frac{s_0}{s_c} \tag{3.7}$$

where s_c is the steady state Child law sheath thickness given by

$$s_c=s_0\left[\frac{2}{9}\left(\frac{u_0}{u_B}\right)\right]^{\frac{1}{2}} \tag{3.8}$$

Given that $s_c >> s_0$ and assuming $s_c >> s$, from (3.7) the following expression for the sheath position is obtained

$$\frac{s^3}{s_0^3} = \left(\frac{2}{3}\right)\omega_{pi}t + 1 \tag{3.9}$$

where $\omega_{pi} = u_0/s_0$ is the ion plasma frequency. Substitution of (3.8) into (3.9) gives an expression for the timescale over which the Child law sheath forms

$$t_c \approx \left(\frac{\sqrt{2}}{9}\right)\left(\frac{1}{\omega_{pi}}\right)\left(\frac{2V_0}{T_e}\right)^{\frac{3}{4}} \tag{3.10}$$

An estimate for the time required for the formation of the Child law sheath can be made for the systems studied in this thesis. For argon ions with the following assumed values of $n_0 = 1$ x 10^{15} m^{-3}, $T_e = 3$ eV and $V_0 = -400$ V the value of t_c is 0.1 μs.

3.4.2 Matrix Sheath Implantation

The implantation current density during the matrix sheath period can be determined by considering the ion acceleration across the sheath. From Gauss's law, the electric field across a one dimensional matrix sheath can be expressed as

$$E = \frac{en_0x}{\epsilon_0} = \frac{M}{e}\left(\frac{d^2x}{dt^2}\right) \tag{3.11}$$

where x is the ion's position. Rearrangement of (3.11) gives

$$\frac{d^2x}{dt^2} = \omega_{pi}^2\,(x - s) \tag{3.12}$$

The sheath edge position can be approximated by

$$s = s_0 + t\left(\frac{ds}{dt}\right)_{t=0} \tag{3.13}$$

Substitution of (3.3) with $s = s_0$ into (3.13) gives

$$s = s_0 + t\left(\frac{2}{9}u_0 - u_B\right) \tag{3.14}$$

Integration of (3.14) gives

$$x - s_0 = (x_0 - s_0)\cosh(\omega_{pi}t) - \frac{2}{9}s_0\sinh(\omega_{pi}t) + \frac{2}{9}u_0 t \tag{3.15}$$

where $x = x_0$ and $dx/dt = 0$ at $t = 0$. An expression for the ion flight time (t) across the sheath is obtained by setting $x = 0$ in (3.15)

$$s_0 = (s_0 - x_0)\cosh(\omega_{pi}t) + \frac{2}{9}s_0\sinh(\omega_{pi}t) - \frac{2}{9}u_0 t \tag{3.16}$$

During the time interval between t and $t + dt$, ions between x_0 and $x_0 + dx_0$ are implanted. Rearrangement and differentiation of (3.16) gives

$$\frac{dx_0}{dt} = \frac{\omega_{pi}(s_0 - x_0)\sinh(\omega_{pi}t) + \frac{2}{9}u_0(\cosh(\omega_{pi}t) - 1)}{\cosh(\omega_{pi}t)} \tag{3.17}$$

Substitution of (3.16) into (3.17) allows the current density $j = en_0\,(dx_0/dt)$ for ions in the matrix sheath ($0 \leq x_0 \leq s_0$) to be calculated

$$J = \frac{\sinh(T)}{\cosh^2(T)} + \frac{2}{9}\frac{(1 + T\sinh(T) - \cosh(T))}{\cosh^2(T)} \tag{3.18}$$

where $J = j/(en_0u_0)$ is the normalised current density and $T = \omega_{pi}t$ is the normalised time. The time taken for the matrix sheath to form can be determined by setting $x_0 = s_0$ in (3.16). This gives a value of T of approximately 2.7 for the time at which ions start to arrive from the matrix sheath edge. A graph of the normalised implantation current density during the matrix sheath and Child law sheath time periods is shown in figure 3.3 for a -500 V pulse with argon ions with a density of 1x10^{15} m^{-3}.

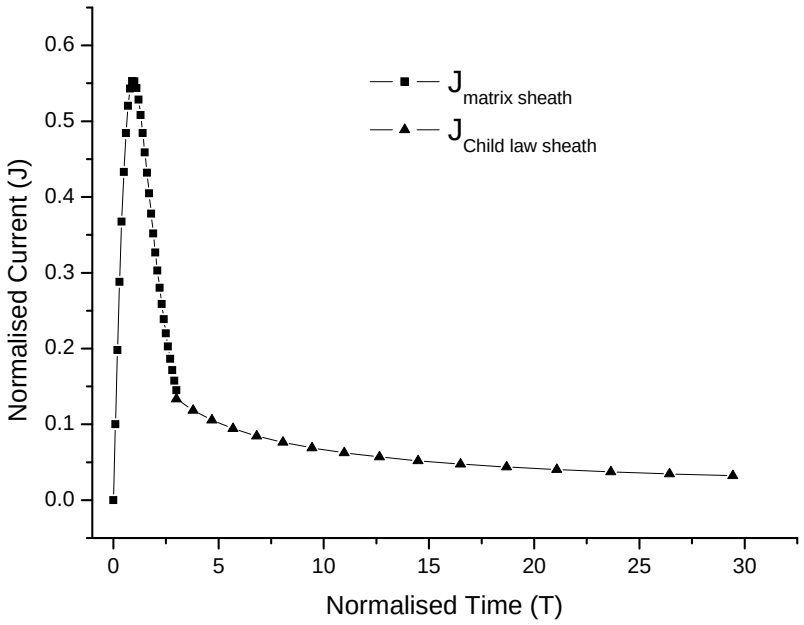

Figure 3.3: Normalised implantation current density (J) versus normalised time (T) during the matrix and Child law sheath time periods obtained using equations (3.18) and (3.27) for a pulse amplitude of -500 V with argon ions with a density of 1x10^{15} m^{-3}.

3.4.3 Child Law Sheath Implantation

The implantation current density of ions with initial positions beyond the matrix sheath edge can be calculated by considering the time required for ions to cross the sheath. The time taken (t_s) for the sheath edge initially at s_0 to reach x_0 can be determined by substitution of $s = x_0$ into equation (3.9)

$$\omega_{pi} t_s = \frac{3}{2}\left(\frac{x_0}{s_0}\right)^3 - \frac{3}{2} \tag{3.19}$$

The time taken for an ion to cross a Child law sheath of thickness s can be determined by considering the sheath potential given by equation (2.49)

$$\phi = -V_0\left(\frac{x}{s}\right)^{\frac{4}{3}} \tag{3.20}$$

The electric field (E) is given by

$$E = -\frac{d\phi}{dx} = \frac{4V_0}{3}\left(\frac{x^{\frac{1}{3}}}{s^{\frac{4}{3}}}\right) \tag{3.21}$$

For an ion with charge q and mass M, the acceleration will be

$$\frac{d^2x}{dt^2} = \frac{qE}{M} = \frac{4qV_0}{3M}\left(\frac{x^{\frac{1}{3}}}{s^{\frac{4}{3}}}\right) \tag{3.22}$$

Integration of (3.22) with the assumption that at $t = 0$, $x = 0$ and $dx/dt = 0$ gives the ion flight time

$$t = 3s\left(\frac{M}{2qV_0}\right)^{\frac{1}{2}} \tag{3.23}$$

which for $s = x_0$ can be expressed as

$$t' = \left(\frac{3x_0}{s_0\omega_{pi}}\right) \tag{3.24}$$

An ion at x_0 will reach the target at $t = t_s + t'$ which can be written using equations (3.19) and (3.24) as

$$T = \omega_{pi}t = \frac{3}{2}\left(\frac{x_0^3}{s_0^3}\right) - \frac{3}{2} + \frac{3x_0}{s_0} \tag{3.25}$$

Differentiation of (3.25) gives

$$\frac{dx_0}{dt} = \frac{u_0}{(9/2)\left(x_0/s_0\right)^2 + 3} \tag{3.26}$$

The normalised current density $J = j/(en_0u_0)$ is given by

$$J = \frac{1}{(9/2)\left(x_0/s_0\right)^2 + 3} \tag{3.27}$$

From equation (3.25), for $x_0/s_0 = 1$, $T = 3$ and as $T \to \infty$, $x_0 \to s_c >> s_0$ and J approaches the steady state value of en_0u_B. A graph of equation (3.27) is shown in figure 3.3 for a -500 V pulse with argon ions with a density of 1x10^{15} m^{-3}. The

discontinuity at $T = 3$ is due to the assumptions made about the formation of the Child law sheath and the sheath electric field.

While this model provides only qualitative agreement with more detailed analytical and numerical models, it illustrates the large current of ions received by the pulsed object from the matrix sheath and the rapid decrease in this current towards the steady state value of the Child law sheath.

3.5 Ion Dose and Energy Studies in PIII

In PIII and PIIID, the energy distribution of ions arriving at the pulsed object is important in determining the extent of surface modifications and thin film properties, such as in the case of diamond like carbon films [76]. Direct experimental measurements of the IED at the pulsed object during PIII are difficult due to the large voltages involved and the microsecond timescale over which the measurements must be performed. While there have been a number of analytical studies and numerical simulations of factors affecting ion dose and energy during PIII, there have been very few direct experimental measurements of the IED. In this section, some of the key results of these simulation and experimental studies will be reviewed.

3.5.1 Analytical Models of PIII

Analytical models have provided useful information on the evolution of plasma parameters during PIII. One dimensional analytical models, such as presented in section 3.4, have been developed to describe the implantation current and energy distribution for planar [80], cylindrical and spherical geometries [118].

For the one dimensional planar, collisionless case with instantaneous pulse rise and fall time, the IED is made up of three groups of ions. Ions which are uncovered by the formation of the matrix sheath will impact the object with an energy between zero and qV_0 where V_0 is the pulse amplitude. The energy of these ions will depend on the potential at their starting position in the matrix sheath. As the sheath edge extends outward to its final steady state Child law value, any ion which crosses the sheath edge will be accelerated into the object with the full sheath potential energy

qV_0. Finally, when the pulse switches off, any ions in the sheath will impact the object with an energy dependent on the potential at the position at which they were located in the sheath when the pulse switched off.

One dimensional analytical models have also been developed for pulses with finite rise and fall times [129] and for pulse biased plasmas [92] which more accurately model real experiments. The IED is dependent on the ratio between the pulse rise/fall time and the time period at which the pulse voltage is at its maximum. As the pulse rise/fall time increases, the fraction of ions with energy less than the maximum sheath potential increases.

One dimensional analytical models for PIII have also been developed for highly collisional sheaths [139] and for multiple charge state ions [111]. As the gas pressure increases, the number of lower velocity ions increases due to ion collisions in the sheath. For multiply charged ions, ion energy increases with increased charge state and this increases implantation depth. Sheath expansion for increased charge state ions is also faster due to their greater charge.

3.5.2 Numerical Simulations of PIII of Conductors

Numerical simulations using particle in cell (PIC) methods have been applied to study the effects of pulse, plasma and target parameters on ion dose and energy in PIII. Pulse parameters such as pulse rise and fall time have been shown to have a significant effect on IEDs. Ions which enter the sheath during the pulse rise or fall times will experience less than the full accelerating potential, causing a spread in the IED [134, 2, 84, 95]. To minimise the number of ions which implant during the pulse rise time, the rise time must be less than the ion transit time across the matrix sheath. To minimise the number of ions which implant during the pulse fall time, the fall time must be less than the maximum sheath collapse rate of s/u_B, where s is the sheath thickness and u_B is the Bohm velocity, to prevent ions from diffusing across the sheath as the pulse collapses. The ion transit time across the sheath is also dependent on the ion mass [60]. For lighter ions, which have a greater acceleration, the sheath expansion rate is faster and more ions are implanted during the pulse rise

time leading to a broader IED. For heavier ions, fewer ions are implanted during the pulse rise time. The use of a positive pulse before a negative pulse in pulse generated plasmas for PIII has also been studied [96]. The positive pulse is used to ignite the glow discharge and was found to produce plasmas more conformal to trench shaped objects.

The effects of plasma parameters such as pressure and plasma uniformity have also been studied using simulation [152, 51, 83, 2]. Non-uniformities in the plasma due to the chamber and electrode design affect sheath expansion and this affects the ion flux and angles at which ions strike the pulsed object. Ion collisions in the sheath also cause a significant broadening to the IED [83]. Both simulation and experimental results show that as pressure increases, the total flux to the pulsed object increases due to charge exchange collisions in the sheath producing fast neutrals which strike the object's surface and release secondary electrons. As pulse amplitude and sheath thickness increase, the release of secondary electrons becomes larger. These secondary electrons are accelerated back across the sheath and into the plasma where they can cause increased ionisation through collisions with neutral species. Increasing plasma density increases the total dose and reduces the sheath width which reduces ion collisions and the number of low energy ions. However, it also leads to increasingly nonuniform sheath expansion and uneven dose distribution across the sample [152]. A similar effect occurs with the use of longer pulse widths which lead to uneven sheath expansion if the sheath width has not yet reached the Child law equilibrium sheath thickness.

While objects with dimensions of the order of the matrix sheath thickness have a more conformal sheath [152], many PIII applications involve the treatment of complex shaped objects such as trenches, cylinders or spheres. The non uniform sheath shape around these objects will affect the ion dose and energy distribution. During PIII treatment of trenches, the side walls receive very little ion implantation once the sheath has expanded out of the trench [69, 103, 123, 110, 15]. To maximise the energy of these ions, short pulse rise times are required so that ions arriving during the early stages of sheath expansion have more energy. Once the matrix sheath has developed, the majority of ions implant into the trench tops or trench base with

the full pulse voltage energy but increased trench depth will reduce implantation into the base due to ion deflection to the sidewalls. These simulations support experimental measurements of ion dose into trenches and cylinders which show little implantation into side walls [38, 39, 87]. The IEDs at the trench top and bottom show peaks near the maximum ion energy [110]. For the side walls, the IEDs have a broad structure with fewer maximum energy ions. Most ions which strike the sides do so when the sheath is expanding out of the trench and have less than the full pulse voltage energy.

Trench corners also receive uneven treatment due to the convergence of electric field lines to convex corners at trench tops and divergence of electric field lines away from concave corners in trench bottoms. This effect has been seen in other structures such as cone tips [71] and causes an increased implantation at convex corners and reduced implantation at concave corners.

3.5.3 Numerical Simulations of PIII of Insulators

During PIII treatment of an insulator, the implantation of positive ions and the emission of secondary electrons due to ion bombardment reduces the insulator surface potential. Simulations and experimental studies have shown that this will affect ion implantation and sheath development. Simulations have shown the increase in insulator surface potential during pulsing and that the majority of the implantation dose is received during the first few microseconds of the pulse when the surface potential is lowest [41, 133]. From both experiment and simulation it has been shown a thinner and/or higher dielectric constant sample will have a larger ion dose and greater treatment depth. This can be understood by approximating the sample to be a parallel plate capacitor of thickness d with a capacitance C given by

$$C = \frac{\epsilon_r \epsilon_0 A}{d} = \frac{Q}{V} \tag{3.28}$$

where Q is the sample charge, A is the sample surface area, ϵ_r is the dielectric constant and V the potential across the sample. As ϵ_r increases and/or d decreases, the potential across the sample decreases and the potential across the sheath will

increase, causing ions to implant with more energy. As the sheath potential and sheath thickness increase, the plasma-sheath surface area will increase causing the ion flux to become larger.

Surface charging has been shown experimentally and with simulation to distort sheath expansion [132]. During PIII, at the interface between an insulator and conductor, the thinner sheath above the insulator causes increased ion bombardment of the conductor and the insulator edges near the conductor. Increasing ion density in the plasma will increase the total dose but will also increase surface charging, causing an increased spread of the IED [82] and a greater change to the surface potential [41].

3.5.4 Numerical Simulations of Mesh Assisted PIII

The placement of a metal mesh around an insulator during PIII has been shown to reduce surface charging. The pulse bias is applied to both the mesh and the insulator base and the mesh reflects secondary electrons emitted by ion implantation back to the insulator. In both simulations and experiments this has been shown to reduce the increase in surface potential and increase treatment depth [44, 24, 132]. Simulations have shown that the implantation of ions is affected by space charge build up inside the mesh and by the shape of the expanding sheath around the mesh [24, 109]. The hemispherical sheath shape which forms around a cylindrical mesh during pulsing causes ion lensing with a focal point which shifts as the sheath evolves. In the case where there is no plasma inside the mesh, a positive space charge builds up which alters ion trajectories and broadens the IED until the charge dissipates during the pulse-off period.

3.5.5 Experimental PIII Ion Energy Measurements

The IED during PIII has been determined in simulation studies for trenches [96, 103, 110, 69] and at planar surfaces investigating the effects of pressure, insulators, mesh and ion mass [23, 83, 152, 84, 134, 82, 60, 2, 109]. However, there have only been limited experimental measurements of IEDs during PIII.

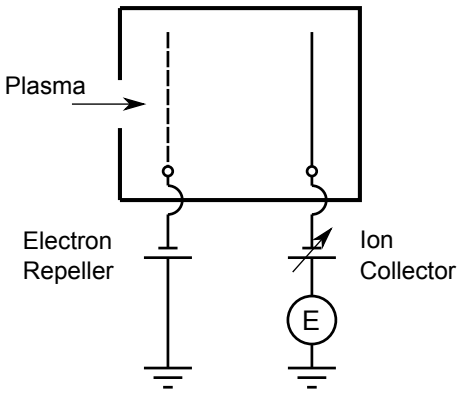

Figure 3.4: A Faraday cup for ion energy measurements uses a negatively biased grid to repel electrons and an ion collector plate with a variable bias to measure ion current as a function of ion energy using a device such as an electrometer (E).

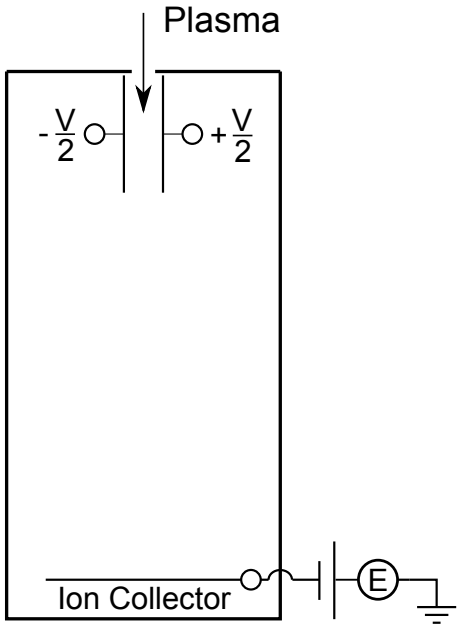

Figure 3.5: A parallel plate ion energy analyser uses electrically biased plate deflectors to control the energy of the ions that are measured at the collector disc which is biased negatively to repel plasma electrons.

IED measurements during PIII have been made using Faraday cups and also with a parallel plate energy analyser. As shown in figure 3.4, a Faraday cup is a metal cylinder which houses a metal ion collector disc and an electron repeller grid [54]. The electron repeller grid is biased negatively to repel plasma electrons while the bias on the ion collector plate can be varied to control which energy ions reach the collector. Faraday cups have been used to determine IEDs at a hemispherical target with pulse amplitudes up to -20 kV [88] and at a flat plate with voltages up to -10 kV [61]. The hemispherical target results show a decrease in ion flux after several microseconds due to the stopping of sheath expansion after the sheath reaches the Child law thickness.

A parallel plate energy analyser is a cylinder housing parallel deflecting plates and a metal collector disc as shown in figure 3.5. A bias voltage applied to the parallel plates deflects ions based on the time spent between the plates which is dependent on the ion's velocity. The parallel plate voltage can be varied to discriminate which energy ions are able to reach the ion collector. This type of analyser has been used to measure IEDs in a system where the target object is held at 0 V and the chamber is positively biased to accelerate ions into the target [55].

Mass spectrometer systems have also been used to study IEDs in pulsed plasma doping systems [46]. Commercial mass spectrometers can be fitted with electrical signal gating to perform time resolved ion energy measurements during PIII. Studies in BF_3 plasmas with pulse amplitudes of -500 and -1000 V have shown that as pressure increases from 100 up to 250 mTorr, the IED widens due to increased collisions in the sheath.

IEDs have also been determined from depth profiles of implanted ions during PIII [7, 140, 112]. The depth profile can be obtained using methods such as secondary ion mass spectrometry (SIMS), Auger electron spectroscopy (AES) or elastic recoil detection analysis (ERDA). The IED can be determined by fitting depth profile data to theoretical plots using computer software packages such as TRIM (the transport of ions in matter) [160].

To date, there have not been any reported experimental measurements of IEDs during mesh assisted PIII. Simulations of mesh assisted PIII have shown important

effects which will affect ion dose and energy such as space charge build up inside the mesh and ion focusing due to the sheath shape around the mesh [109]. While Faraday cups and parallel plate energy analysers can measure IEDs, as will be discussed in section 4.2, measurements made with these probes can have significant errors due to secondary electron emissions. Mass spectrometer systems can also measure IEDs but their large size and cost make installation in many plasma systems difficult. In this thesis, a retarding field energy analyser (RFEA) was used for IED measurements during PIII. As will be discussed in chapter 4, through the use of multiple grids the RFEA minimises the effects of secondary electron emission and its compact size allows it to be easily installed in most plasma systems.

3.6 Summary

Plasma immersion ion implantation (PIII) is a materials modification technique where an object is placed in a plasma and pulse biased with a negative voltage. PIII is increasingly being used in the treatment of metals, semiconductors and insulators. For the treatment of insulators, a metal mesh can be placed around the object being treated and pulse biased together with the object to minimise the effects of surface charging. After the application of the pulse, on the timescale of the inverse plasma electron frequency, an ion matrix sheath forms and ions in the matrix sheath are implanted into the pulsed object with energies dependent on their starting position. On longer timescales of the order of the inverse plasma ion frequency, the sheath thickness extends outward toward a steady state Child law sheath thickness with ions implanting with the full pulse potential energy. A number of analytical and numerical models have been developed to study ion dose and energy during PIII. These studies have shown that factors which affect the development of the sheath such as the ion density, pulse rise and fall time and target shape and material will have a significant effect on the implanted ion dose and energy. There have only been a limited number of experimental measurements of ion dose and energy at the pulse biased object during PIII using Faraday cups, parallel plate energy analysers and mass spectrometer systems. A retarding field energy analyser (RFEA) allows some

of the disadvantages of these methods to be overcome and is used in this thesis for ion energy measurements during PIII.

Chapter 4

The Retarding Field Energy Analyser

4.1 Introduction

The energy of ions arriving at a pulse biased object during PIII are important in determining the extent of surface modifications. The large size of mass spectrometers and the problems associated with the control of secondary electron emission in Faraday cups can be overcome using a retarding field energy analyser (RFEA). The subject of this chapter is the design and testing of a retarding field energy analyser (RFEA) for time resolved ion energy measurements during PIII. In section 4.2, the theory of how a RFEA works is discussed. In section 4.3, a review of the use of mass spectrometers and RFEAs for time resolved ion energy measurements is given. In sections 4.4 and 4.5, the design and construction of the RFEA used in this thesis is discussed. In section 4.6, initial results obtained using the RFEA in a DC biased mode are presented.

4.2 Theory

The energy of ions arriving at a surface are important in determining the extent of surface modifications. While Langmuir probes can be used to determine the electron temperature, electron density and electron energy distribution they have

limited usefulness in measuring IEDs. A basic Langmuir probe consists of a metal wire, inserted into the plasma, with a variable voltage applied to it [99]. A sheath forms around the wire and while the bias voltage on the wire is below the floating potential (ϕ_f), the wire draws mostly ion current. As the bias voltage approaches ϕ_f, the probe draws more and more electron current and for bias voltages above ϕ_f, an electron saturation current is approached and the ion current drops to zero. The variations in ion and/or electron current can be used to derive information on the electron or ion energy distributions. Due to their smaller mass, the electron saturation current is much larger than the ion current and can swamp out small changes in ion current, making it difficult to obtain any information on the ion energy.

To effectively measure ion energies, the electron flux must be removed. This can be done using a Faraday cup as discussed in section 3.5.5. As shown in figure 3.4, plasma enters the cup through an inlet orifice and electrons are repelled by a negatively biased grid. Ion current is measured at the metal collector disc which has a variable bias voltage applied to it. Information on the IED can be obtained by varying the collector bias voltage which discriminates which energy ions are able to reach the collector [54].

In a Faraday cup, ions which are repelled from the collector can collide with the electron repeller grid, releasing secondary electrons which will cause errors in the measurement of ion current. The problem of secondary electron emission can be reduced by using a retarding field energy analyser (RFEA) which uses multiple grids as shown in figure 4.1. The first grid (F) is held at the potential of the probe body to prevent electric fields in the RFEA from perturbing the plasma. The second grid (R) is biased negatively to repel plasma electrons. The third grid (D) is biased with a voltage which is stepped upwards to discriminate which energy ions can pass through to the negatively biased collector (C). The suppressor grid (S) is biased more negatively than the collector to return secondary electrons released by ion impacts with the collector. The suppressor also prevents secondary electrons released by ion impacts with other grids from reaching the collector.

In a RFEA, ion current is recorded at the collector as the discriminator voltage

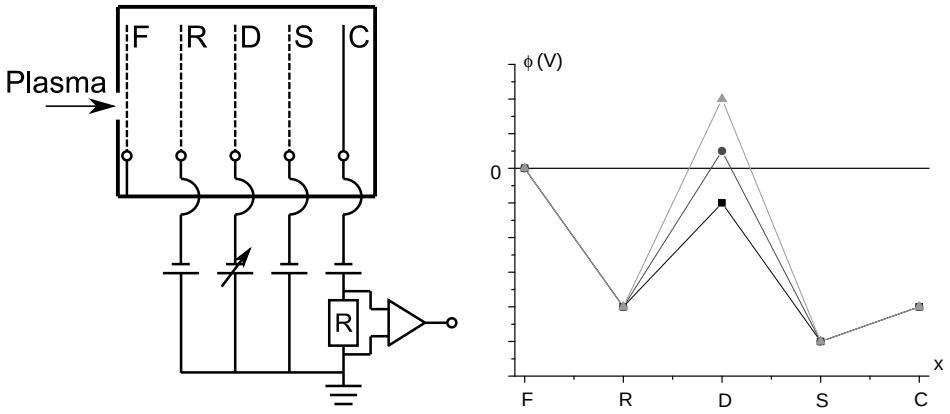

(a) RFEA Schematic (b) RFEA Grid Potentials

Figure 4.1: (a) A retarding field energy analyser (RFEA) uses a series of biased grids and a metal collector to measure ion energy and flux. (b) The first grid (F) is held at the probe body potential. The second grid (R) is biased negatively to repel electrons. The third grid (D) has a variable voltage applied to discriminate which ions can pass through to the collector (C). The fourth grid (S) is biased negatively to minimise the effects of secondary electron emission.

is stepped upwards. The RFEA discriminates ions based on the component of their velocity perpendicular to the grid faces and the IED can be calculated from the ion current versus discriminator voltage graph [70, 54]. For a single species, the ion current (I_c) at a collector with area A is given by

$$I_c = A\tau e \int_{-\infty}^{0} f(v_\perp) v_\perp dv_\perp \tag{4.1}$$

where τ is the overall transmission coefficient of the RFEA grids, $v_\perp$ is the component of the ion velocity perpendicular to the grid face and $f(v_\perp)$ is the velocity distribution function. The velocity ($v_\perp$) of an ion with mass M, accelerated by a potential ϕ can be expressed by equating the kinetic energy of the ion to the electrostatic potential energy ($e\phi$) to give

$$v_\perp = \sqrt{\frac{2e\phi}{M}} \tag{4.2}$$

At a discriminator potential ϕ, the ion current at the collector will be

$$I_c = A\tau e \int_{-\infty}^{-\sqrt{\left|\frac{2e\phi}{M}\right|}} f(v_\perp) v_\perp dv_\perp \tag{4.3}$$

Rearrangement and differentiation of (4.2) with respect to $v_\perp$ gives

$$\frac{d\phi}{dv_\perp} = \frac{Mv_\perp}{e} \tag{4.4}$$

Using (4.4), differentiation of (4.3) with respect to ϕ gives

$$\frac{dI_c}{d\phi} = \frac{dI_c}{dv_\perp}\left(\frac{e}{Mv_\perp}\right) = \left(\frac{e^2A\tau}{Mv_\perp}\right)\frac{d}{dv_\perp}\int_{-\infty}^{-\sqrt{\left|\frac{2e\phi}{M}\right|}} f(v_\perp)v_\perp dv_\perp = \frac{e^2A\tau}{M}f(v_\perp) \tag{4.5}$$

Equation (4.5) shows that the ion velocity distribution is proportional to the first derivative of the collector current versus discriminator voltage. Using the experimentally determined IED, information on the average ion density $\langle n\rangle$, mean ion velocity $\langle v_\perp\rangle$ and mean random energy $\langle E_\perp\rangle$ associated with ion motion perpendicular to the grid face can be obtained [70]. The average ion density is given by

$$\langle n\rangle = \int_{-\infty}^{\infty} f(v_\perp)dv_\perp \tag{4.6}$$

Substitution of the derivative of (4.2), with respect to ϕ, into (4.6) gives

$$\langle n\rangle = \left(\frac{e}{2M}\right)^{\frac{1}{2}}\int_0^{\infty}\frac{f\left(v_\perp\right)}{\phi^{\frac{1}{2}}}d\phi \tag{4.7}$$

To determine $\langle v_\perp\rangle$ and $\langle E_\perp\rangle$, the following parameters must be obtained with substitution of (4.2) and the derivative of (4.2) with respect to ϕ

$$\langle nv_\perp\rangle = \int_{-\infty}^{\infty} v_\perp f(v_\perp)dv_\perp = \left(\frac{e}{M}\right)\int_0^{\infty} f(v_\perp)d\phi \tag{4.8}$$

$$\left\langle\frac{Mv_\perp^2 n}{2}\right\rangle = \int_{-\infty}^{\infty}\frac{Mv_\perp^2}{2}f(v_\perp)dv_\perp = e\left(\frac{e}{2M}\right)^{\frac{1}{2}}\int_0^{\infty}\phi^{\frac{1}{2}}f(v_\perp)d\phi \tag{4.9}$$

The mean velocity is given by

$$\langle v_\perp\rangle = \frac{\langle nv_\perp\rangle}{\langle n\rangle} \tag{4.10}$$

and the mean kinetic energy is given by

$$\left\langle \frac{Mv_{\perp}^2}{2} \right\rangle = \frac{\langle Mv_{\perp}^2 n/2 \rangle}{\langle n \rangle} \tag{4.11}$$

The mean random energy associated with the velocity component perpendicular to the grid face is given by

$$\langle E_{\perp} \rangle = \left\langle \frac{Mv_{\perp}^2}{2} \right\rangle - \left(\frac{M}{2} \right) \langle v_{\perp} \rangle^2 \tag{4.12}$$

While the RFEA provides a simple and effective means of measuring the IED, its design has some limitations. Ion losses to grids will reduce the total ion current and require the use of sensitive current measurement devices at the collector. Compared to a Langmuir probe, the RFEA is larger in size. When mounted as part of the substrate or electrode this is not a problem but when used in the bulk plasma the RFEA will perturb the plasma. If differential pumping is not used, to minimise ion collisions inside the analyser, the total distance from the probe front to the discriminator grid must be significantly less than an ion mean free path. Finally, in high density plasmas, the build up of space charge between grids can affect the potential profile inside the analyser. These issues and their effect on the design of the RFEA used in this thesis will be discussed in section 4.5.

4.3 RFEAs and Mass Spectrometers

IEDs can be measured using mass spectrometers and RFEAs. Since the 1960s [125], different designs of RFEA have been used to measure IEDs in a variety of plasma discharges under different conditions. In this section, a review of the application of RFEAs and mass spectrometers to ion dose and energy measurements is given.

4.3.1 Mass Spectrometers

IEDs can be measured with mass spectrometer systems fitted with electrostatic energy analysers. A simplified schematic of a mass spectrometer system is shown

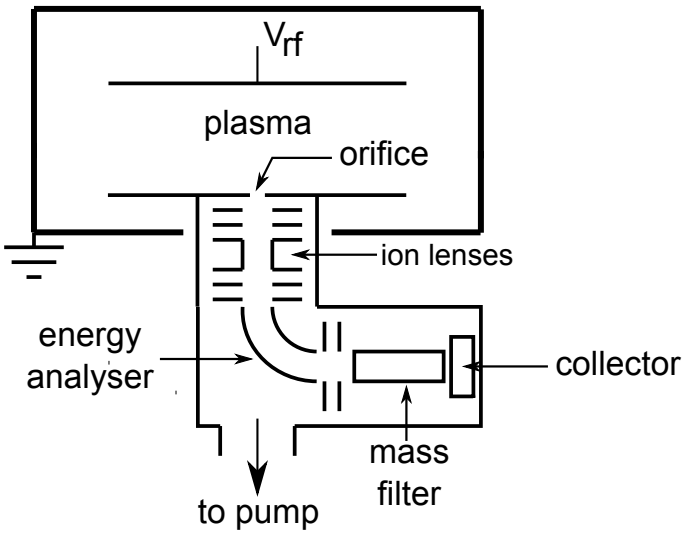

Figure 4.2: A schematic of the main parts of a mass spectrometer system for ion energy measurements.

in figure 4.2. Plasma enters the differentially pumped system through an orifice in the electrode. Electrostatic lenses are used to focus ions into the energy analyser and to reject electrons. A variable potential applied to the electrostatic energy analyser discriminates which energy ions are able to pass through to the mass filter. The mass filter discriminates ions based on the ratio of their charge to mass using electric and/or magnetic fields and determines which ions are able to be measured at the collector [49]. Mass spectrometers have been used to measure IEDs in a variety of different plasma systems. At grounded electrodes in capacitive and inductive RF plasmas, the effects on the IED of pressure [127], RF frequency [120], ion mass [8] and parameters affecting plasma potential [66, 25] have been studied using mass spectrometer systems. By floating the spectrometer, IED measurements have been made at RF powered electrodes in capacitive and inductive plasmas investigating the effects of RF power and voltage, pressure and ion mass/charge [97, 158, 48, 94, 1].

While mass spectrometers allow mass and charge selective study of IEDs, they have some disadvantages. Their large size makes them difficult to mount at different locations in a chamber. The paths taken by ions in the spectrometer can be of the order of tens of centimetres in length and the spectrometer must be differentially pumped to reduce the number of ion collisions. Compared to RFEAs, mass

spectrometers are more complicated in their design and this increases their cost.

4.3.2 Retarding Field Energy Analysers

Unlike mass spectrometers, RFEAs cannot distinguish between ions of different charge or easily distinguish between ions of different mass. In the low frequency case, discussed in section 2.5, where the time taken by ions to cross the sheath is much less than the RF period, the splitting of the bimodal peaks in the IED can be used to distinguish ions of different mass [37]. However, in the high frequency case, where ions take many RF periods to cross the sheath, the splitting of the bimodal IED peaks becomes too small to identify different mass ions. The main advantage of RFEAs are their compact size and simplicity. This reduces their perturbation of the plasma and allows them to be easily positioned at different locations in the vacuum chamber. Different variations of RFEA have been used to study IEDs and ion flux in a variety of plasma systems.

RFEAs with electrically grounded bodies have been used in numerous plasma studies. As pressure is increased, RFEA measurements of IEDs in capacitive and inductive RF plasmas show increasing numbers of low energy ions [56, 14, 135, 119]. IED measurements in capacitive RF plasmas show an increase in ion density and in the number of high energy ions with increasing RF power and decreased ionisation in the sheath with increasing RF frequency [14]. In pulsed plasmas, grounded RFEAs have been used to study the effects of pulse frequency and duty cycle on the IED [155]. While most RFEAs are constructed with metal bodies, RFEAs in a ceramic material [5] and a micron scale RFEA with silicon (Si) grids and silicon dioxide (SiO_2) spacers [10] have been constructed. For the micron size RFEA, 750 nm holes were etched into a $Si/SiO_2/Si/SiO_2/Si$ multilayer structure , with a nickel metal top surface, to allow ions to travel through to the silicon collector. The silicon grids were 400 nm thick and the two silicon dioxide layers were one and two μm thick.

The compact size of RFEAs has allowed free standing RFEAs to be used for ion energy measurements in the bulk plasma. Ion energy measurements have been made in helicon RF plasmas [21, 22] and in the boundary layers of tokamak [107, 143] and

heliac fusion plasmas [116]. By rotating the RFEA, computer tomography has also been used to construct three dimensional IEDs [57].

RFEAs have been used in numerous studies of ion flux and energy at DC and RF biased substrates. The energy of ions arriving at DC biased substrates has been studied using RFEAs and related to physical [35] and optical/electrical [105] properties of deposited films. At RF biased substrates, both the plasma potential and substrate potential are oscillating and the energy of an ion arriving at the substrate will depend on the phase at which the ion enters the sheath and the time taken to cross the sheath. If the time taken to cross the sheath is less than the RF period, bimodal peak IEDs will be produced. A number of studies of IEDs at RF biased substrates have been performed using RFEAs, including investigations of the effects of ion mass [37], RF frequency [91] and RF power and pressure [36].

The angle at which ions arrive at the substrate is also important in determining the extent of surface modifications and thin film structure. Using hemispherical grids and a hemispherical collector made up of an array of separate collector discs, RFEAs have been used to measure ion angular distributions (IADs) and IEDs. As pressure increases, ions undergo more collisions in the sheath and the collided, low energy ions have larger incident angles to the substrate [151, 85, 149]. The distortion of the sheath shape around trench corners and bumps on the substrate causes increased deflection of ions and a reduced numbers of high energy ions [150, 64].

Time resolved ion energy measurements have been performed using both mass spectrometers and RFEAs. These measurements are more difficult due to the additional electronics required to study ion energies and flux at different times. Using electronic signal gating, mass spectrometers have been used to study IEDs in pulsed plasma systems during the pulse-on and off periods at grounded substrates in argon [68, 141, 154], boron trifluoride [113, 68] and carbon tetrafluoride [126] plasmas. Time resolved ion energy measurements using RFEAs have been carried out in pulsed argon plasmas [32], and in pulsed helicon plasmas [13].

A number of studies have investigated factors affecting the energy resolution of RFEAs including grid voltages and inlet orifice design [12, 85], space charge build up [161, 98], grid hole lens effects [125, 53] and grid alignment [19]. The outcomes

of these studies will be discussed with regards to the RFEA used in this thesis in section 4.5.

4.4 RFEA Construction

For this thesis, an ion energy analyser was required which was capable of performing time resolved ion energy measurements at a pulse biased substrate during PIII. A commercial mass spectrometer was not used due to the large cost in purchasing such a system and the difficulty in mounting it in an existing chamber without significantly perturbing the plasma. It was instead decided to construct a RFEA. The requirements of the RFEA were:

1. A compact size to allow easy mounting in the vacuum chamber.
2. An outer body that could be pulse biased.
3. An ability to make current measurements on a microsecond time scale.
4. A distance from the first grid to the discriminator grid of less than the mean free path to minimise ion collisions inside the RFEA.

A front and top view of the RFEA which was constructed is shown in figures 4.3 and 4.4. The design of the RFEA was based on a free standing, electrically grounded RFEA in use at the Australian National University [28]. The RFEA was constructed by the Physics Workshop at The University of Sydney. The main body is a stainless steel cylinder with a diameter of 52 mm and height of 36 mm. The RFEA is connected to a stainless steel pipe with a diameter of a 1/4 inch (6.35 mm) which provides a feed through for electrical connections and allows the analyser to be moved to different positions in the vacuum chamber. The 1/4 inch pipe is stepped up to a 3/8 inch (9.525 mm) pipe at the RFEA to allow greater separation between electrical wires entering the RFEA. A vacuum seal is made using Torr Seal at the RFEA end of the 3/8 inch pipe. Both the 1/4 inch and 3/8 inch pipes were electrically grounded through the chamber walls and were insulated from the main body of the RFEA using teflon spacers.

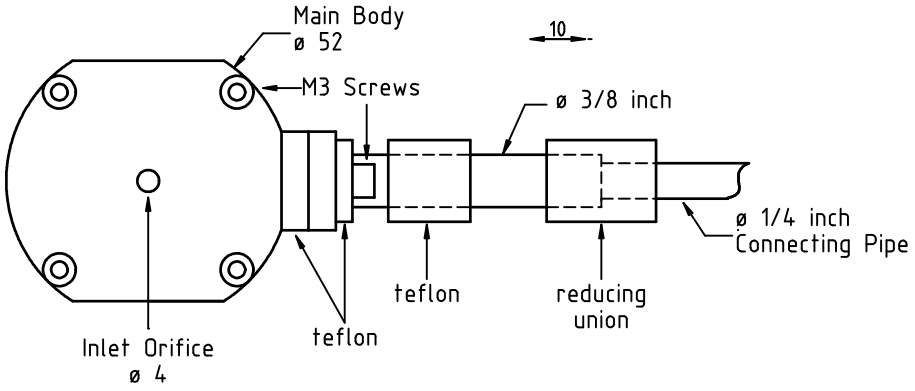

Figure 4.3: Assembled front view of the RFEA used in this thesis.

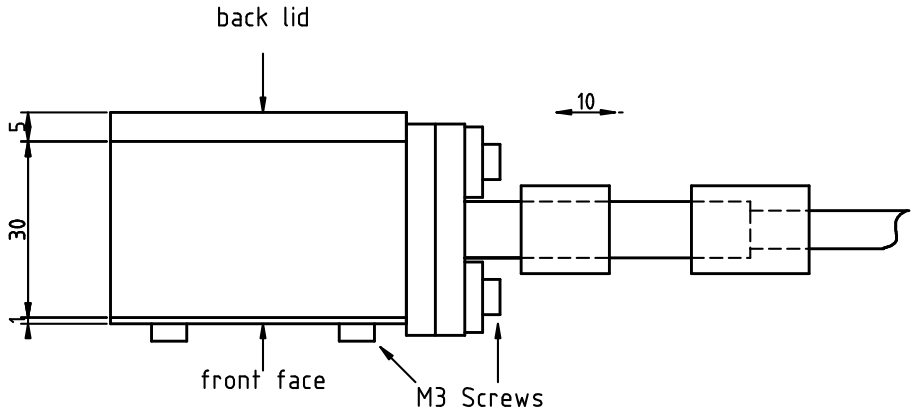

Figure 4.4: Assembled top view of the RFEA used in this thesis.

To allow easy access for servicing, the front and back lids of the RFEA could be removed. The front lid of the analyser was made from stainless steel with a thickness of 0.2 mm and a 4 mm diameter inlet orifice at its centre. The front lid was made as thin as possible to minimise ion losses to the inlet orifice sidewalls, caused by distortion of electric fields in the sheath near the orifice [12, 85]. To prevent electric fields in the analyser from distorting the sheath, the orifice was covered with a conductive nickel mesh with a thickness of approximately 5 μm. The mesh was sixty percent transparent with square holes with side lengths of 39 μm. To minimise electric field distortion of the sheath, the grid hole sizes must be smaller than the Debye length given by equation (2.5). For the plasmas studied in this thesis, with an estimated ion density of 1x10^{15} m^{-3} and an electron temperature of 3 eV, the Debye length is 407 μm. This is much larger than the grid hole size and

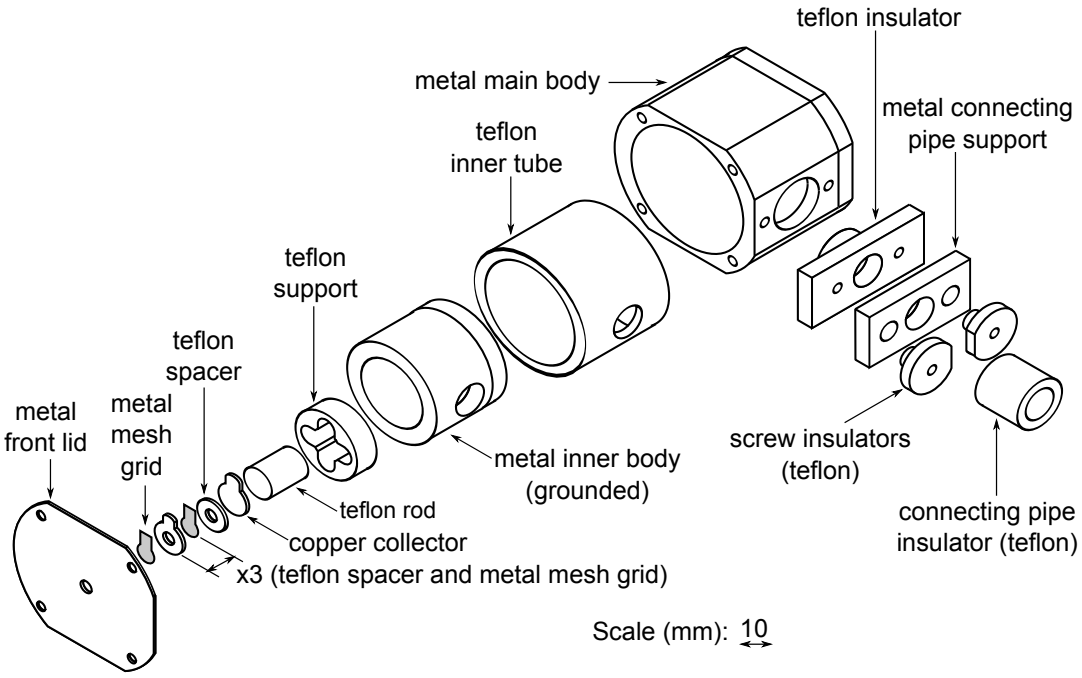

Figure 4.5: Exploded isometric drawing of the internal components of the RFEA. The teflon spacer and metal mesh grid components are repeated three times in the actual RFEA.

as a result the potentials on the grid wires will not be significantly shielded by the plasma.

An exploded isometric drawing of the internal components of the RFEA are shown in figure 4.5. For clarity, the screws and connecting pipe have been omitted. The connecting pipe is joined to the grounded inner body of the RFEA which is insulated from the outer body with a teflon tube. A grounded inner body was used to provide shielding of the collector from electric fields generated by pulsing the probe body.

Inside the grounded inner body, a teflon disc with a cross cut into it was used to support the metal grids, teflon spacers and collector. The RFEA grids were made from the same material used for the mesh covering the inlet orifice. The RFEA used four grids as shown in figure 4.1(a). Each grid had a diameter of 6 mm with a 4 mm wide tab to allow attachment of electrical wires. A teflon spacer with a thickness of 0.8 mm, diameter of 10 mm and a centre hole with a diameter of 4 mm was placed between each grid for insulation. Conductive glue was used to fix the

grid covering the inlet orifice to the front lid. To prevent movement, the tabs on the other grids were fixed with a small dab of glue to the teflon spacer in front of them. Ion current was measured at the copper collector which had a diameter of 10 mm and a 5 mm wide tab. The entire grid, spacer and collector stack was held in place with a teflon support rod which pushed down on the back of the collector. The tabs of the repeller, discriminator, suppressor and collector were positioned in the different arms of the cross cut into the teflon disc. Due to their fragile nature, electrical connections to the grids were made by fixing fine multistrand copper wire to the grid tabs using conductive glue. Connection to the collector was made by soldering copper wire to the collector tab. The overall distance from the top surface of the front lid to the collector was approximately 3.5 mm. The energy resolution of the analyser is determined by the spacing between the grids and the size of the grid holes. The choice of these parameters for the RFEA in this thesis will be discussed in section 4.5.

4.4.1 RFEA Electrical Circuit

A schematic of the electrical connections to the RFEA are shown in figure 4.1(a). Variable DC power supplies were connected to each grid and the collector. Insulated copper wire was used for electrical connections between grids and power supplies. For the collector, a coaxial cable was used between the biasing power supply and the vacuum seal in the connecting pipe, after which insulated copper wire was used. Inside the RFEA, loose fitting teflon cylinder segments were put around the copper wires for insulation to reduce slow outgasing from the wires. At the collector, the ion current was measured as a voltage across a resistor (R). For the DC biased measurements in section 4.6, a 1 MΩ resistor was used and the voltage across the resistor was measured using a Keithley 617 electrometer.

A schematic of the circuit used for time resolved measurements is given in figure A.1 in appendix A. For time resolved measurements, the time constant ($\tau = RC$) of the resistance (R) and coaxial cable capacitance (C) is larger than the microsecond timescale over which measurements need to be performed. The coaxial cable capac-

itance is estimated by assuming the cable is cylindrical with an inner conductor of radius a and an outer conductor of radius b separated by a material with dielectric constant ϵ_r. Using Gauss's law to determine the electric field between the conductors, the potential between the conductors can be determined and substituted into $C = Q/V$ to give

$$C = \frac{2\pi\epsilon_r\epsilon_0 L}{\mathrm{In}\left(\frac{b}{a}\right)} \tag{4.13}$$

where L is the cable length. The 0.5 m length coaxial cable used in the RFEA had an inner conductor with radius of approximately 0.25 mm and outer conductor of radius of approximately 1 mm with a teflon dielectric. Using equation (4.13), the cable capacitance is approximately 28 pF and for a 1 MΩ resistor the time constant is 28 μs which is much greater than the microsecond time resolution required for measurements. To overcome this problem, the resistor value was reduced to 1 kΩ and the three stage amplifier circuit shown in figure A.1 in appendix A was used to measure the ion current.

4.5 RFEA Design Considerations

The energy resolution of a RFEA is limited by ion collisions in the probe, aperture diameters, electrostatic lens effects at grid holes and space charge build up between grids. In this section, these effects will be discussed in relation to the RFEA used in this thesis.

4.5.1 Ion Collisions

Ion collisions inside the RFEA alter the energy of ions, causing errors in the IED measurements. Due to the low ionisation level of the plasmas studied in this thesis, the majority of collisions ions undergo will be with neutral gas molecules. To minimise the effects of ion collisions on IED measurements, the distance from the RFEA front to the discriminator grid must be much less than a mean free path. Ions which collide with gas molecules after the discriminator will still be measured

at the collector with the correct energy.

From kinetic theory, the mean free path (λ) for collisions between rigid gas molecules with a diameter a is given by

$$\lambda = \frac{1}{\sqrt{2}\pi n a^2} \tag{4.14}$$

where n is the neutral gas density. At a given pressure (p) in Pa and temperature (T) in Kelvins, the neutral gas density is given by

$$n = \frac{p}{k_B T} \tag{4.15}$$

where k_B is the Boltzmann constant. Using equation (4.14) and (4.15), for argon atoms with a diameter of 196 pm [124] at a temperature of 300 K and pressure of 5 mTorr (0.67 Pa), the mean free path for hard sphere collisions is 3.6 cm. Over this distance, the number of ions which do not collide will be $1/e$ times the total incoming flux.

Charge exchange collisions occur when a fast ion collides with a neutral atom and captures an electron to produce a fast neutral atom and a slow ion. For charge exchange collisions, the collision cross section increases as the energy of the incoming ion decreases and is of the order of $5\text{x}10^{-19}$ m^2 for argon ions in argon [29]. At a pressure of 5 mTorr, using equation (2.10) this gives a mean free path of approximately 12 mm. In the RFEA used in this work, the distance from the RFEA front to the discriminator is approximately 1.8 mm which is much less than the mean free path based on the argon atom diameter or charge exchange at 5 mTorr.

4.5.2 Aperture Diameters

The finite diameter of grid apertures in the RFEA results in ion losses which affect the acceptance angle of the analyser. This effect is illustrated in figure 4.6, which shows two apertures with diameters A and B covered by metal mesh and separated by a distance D. Even if both ion 1 and 2 have enough energy to pass through grid $G2$, ion 2 will not be measured due to the finite size of the apertures. Both

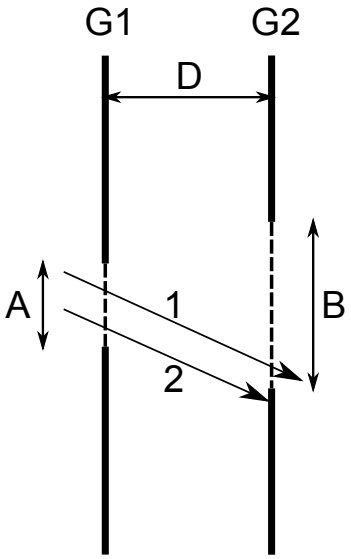

Figure 4.6: The trajectories of two ions (1 and 2) through apertures of diameters A and B covered by metal mesh in the RFEA. The loss of ions to aperture walls affects the RFEA acceptance angle. To minimise the loss of ions, the distance between apertures (D) must be kept much less than the aperture diameters.

experimental measurements [74] and theoretical calculations [31] have shown that to minimise this effect, the separation distance between grids must be kept much less than the aperture diameters.

4.5.3 Grid Hole Lens Effects

The grid holes of the meshes used in the RFEA act as electrostatic lenses and the trajectories of incoming ions will diverge, limiting the analyser energy resolution. The effects of electrostatic lensing on RFEA measurements has been addressed in a number of studies [125, 53, 117].

The paraxial equation for charged particles can be used to estimate the focal length of a circular aperture [128]. The focal length (f) of a circular aperture, for charged particles with energy eV_0 travelling parallel and close to the axis through the aperture is given by

$$f = \frac{4V_0}{E_2 - E_1} \tag{4.16}$$

where E_1 and E_2 are the electric fields on either side of the aperture. A positive

focal length indicates a converging lens action and a negative focal length indicates a diverging lens action. Using equation (4.16), the holes of the front (F) and discriminator (D) grids act as converging lenses and the holes of the repeller (R) and suppressor (S) grids act as diverging lenses.

Equation (4.16) shows that as the energy of the ion (eV_0) becomes smaller, the lensing action of the grid holes becomes stronger. At both the front and repeller grids, the ions are moving with relatively high velocity and the lensing actions are weak with focal lengths greater than the grid separation distance. At the discriminator where ions are decelerated, the divergent action of the grid holes becomes stronger, spreading the ion beam which passes through the grid hole. As the grids in the RFEA were not aligned, the spreading of the ion trajectories after the discriminator should not cause significant errors in IED measurements.

The variation in potential across grid holes also cause errors in ion energy measurements. While the potential at the grid wires will equal the applied potential, the electric fields on either side of the grid will cause a potential gradient across the grid hole. At the discriminator, this results in ions with energy less than the wire potential passing through the hole centre, causing measurement errors. The potential variation across the grid hole can be minimised by decreasing the grid hole size and/or reducing the electric field between grids by increasing grid separation. However, as the grid hole size decreases, ion flux to the collector will also decrease due to ion losses at the grid wires.

For an effective RFEA, a balance must be obtained between bringing the grids as close as possible to reduce ion collisions and keeping the grids far enough apart to minimise lens effects and potential variation across the grid holes. The spacing between grids and grid hole size for the RFEA in this thesis were chosen as a compromise between these competing factors.

4.5.4 Space Charge Effects

The build up of space charge between grids in the analyser alters the potential profile and affects ion energy measurements. This is a significant problem in high density

plasmas [98] and space charge dominated beams [161, 30].

An estimate of the space charge potential (ϕ) between two grids in one dimension is determined using Poisson's equation

$$\frac{d^2\phi}{dx^2} = -\frac{en_0}{\epsilon_0} \tag{4.17}$$

where n_0 is the bulk plasma density. Assuming potentials V_1 and V_2 on two grids separated by a distance d, equation (4.17) is solved to give

$$\phi(x) = \left(\frac{-en_0}{2\epsilon_0}\right)x^2 + \left(\frac{V_2 - V_1}{d} + \frac{en_0 d}{2\epsilon_0}\right)x + V_1 \tag{4.18}$$

Inside the RFEA, the region of most significant space charge build up occurs between the repeller and discriminator grids where ions rejected by the discriminator can accumulate. A graph of the potential between the repeller (R) and discriminator (D) grids obtained using equation (4.18) is shown in figure 4.7. The repeller voltage is -80 V, the discriminator voltage is 0V and the grid separation is 0.8 mm. The ion density was taken to be twice the expected bulk ion density of 1x10^{15} m^{-3}. This density was then attenuated by the transparency of the front and repeller grids to account for ions lost to these grids. The graph shows that the space charge build up has very little effect on the potential profile.

4.6 RFEA Testing

4.6.1 Experimental Setup

Initial tests of the RFEA were performed with the probe body DC biased. A schematic of the experimental setup used is shown in figure 4.8. Measurements were performed at a pressure of 5 mTorr in a capacitive 13.56 MHz radio frequency (RF) argon plasma with a RF power of 100 W. The RF electrode was disc shaped with a diameter of 13 cm. The RF power supply was an ENI Power Systems OEM-6 with an ENI Power Systems Matchwork matching box. The vacuum chamber was a stainless steel cylinder with a diameter of 44 cm and length of 46 cm.

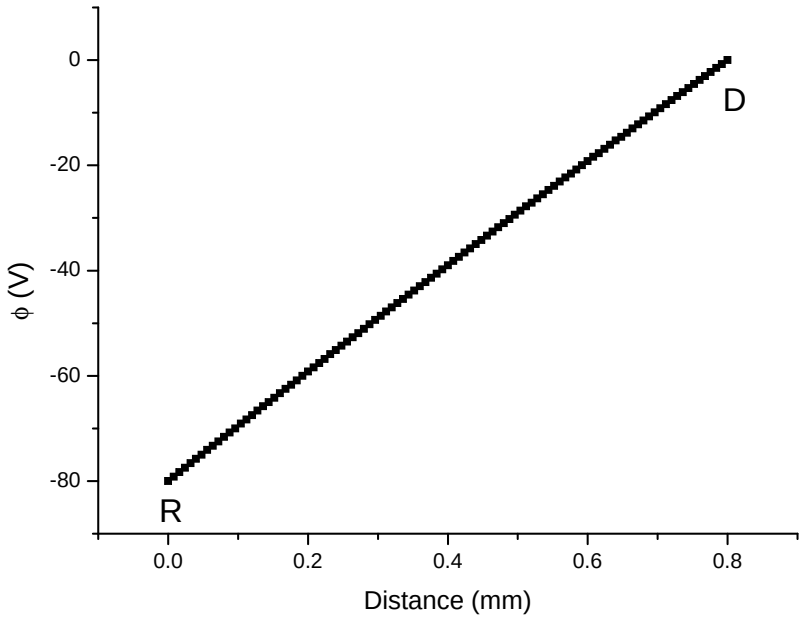

Figure 4.7: A graph of the space charge potential between the repeller (R) and discriminator (D) grids obtained using equation (4.18) with an ion density of 2x10^{15} m^{-3} attenuated by the transparency of the front and repeller grids.

The outer body of the RFEA was biased using a variable voltage DC power supply. The ion current to the RFEA collector was recorded as a voltage across a 1 MΩ resistor using a Keithley 617 electrometer. The RFEA grids and collector were biased using variable DC power supplies and a graph of the grid bias voltages used is shown in figure 4.9. The probe body (F) was biased at voltages between -30 and 30 V. The repeller voltage was set to -80 V to repel plasma electrons. Assuming an electron temperature of 3 eV, the majority of electrons should be repelled by a voltage of -80 V. The discriminator (D) potential was varied between -60 and 100 V. The suppressor (S) was set to -100 V to minimise the effects of secondary electron emission on ion current measurements at the collector (C) which was set to -80 V to attract ions.

A computer program written in LabView was used to record the voltage across the 1 MΩ resistor and to control the discriminator grid voltage. The computer graphing program Origin was used for analysis of the ion current versus discriminator grid voltage data.

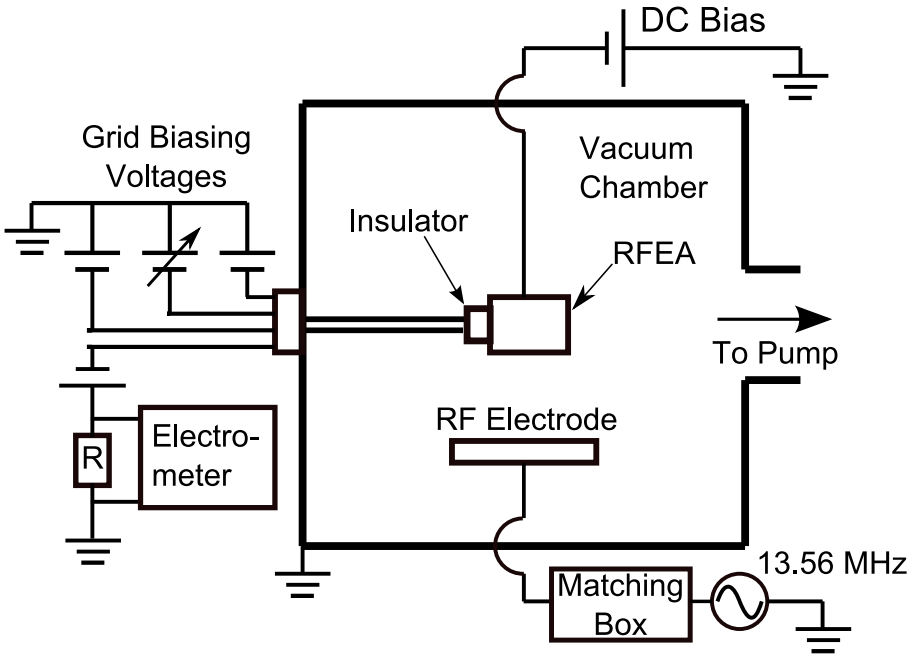

Figure 4.8: Schematic of the experimental setup used for ion energy measurements with a DC biased RFEA.

4.6.2 Grounded RFEA Results and Discussion

In the first experiments, ion energy measurements were made with the probe body electrically grounded. A graph of the collector current versus discriminator voltage and the IED obtained from this data using equation (4.5), are shown in figure 4.10. For discriminator voltages above the maximum ion energy, the collector current goes to a negative value due to an electrical leakage current between the collector and earth. This leakage current is dependent on the collector bias voltage which is kept constant for all measurements. From the IED graph, the maximum ion energy measured was 24 eV. The IED has a peak at 20 eV and a range of ions measured with energies between zero and the maximum ion energy.

For the grounded RFEA, the maximum ion energy value of 24 eV represents the time averaged local plasma potential (V_p) in the region of the plasma surrounding the RFEA. Using equation (2.103), the time taken by an ion to cross the sheath when the RFEA body is grounded is much longer than the RF period and ions will only experience the time averaged plasma potential. The IED peak close to the maximum ion energy indicates that the majority of ions gain close to the full

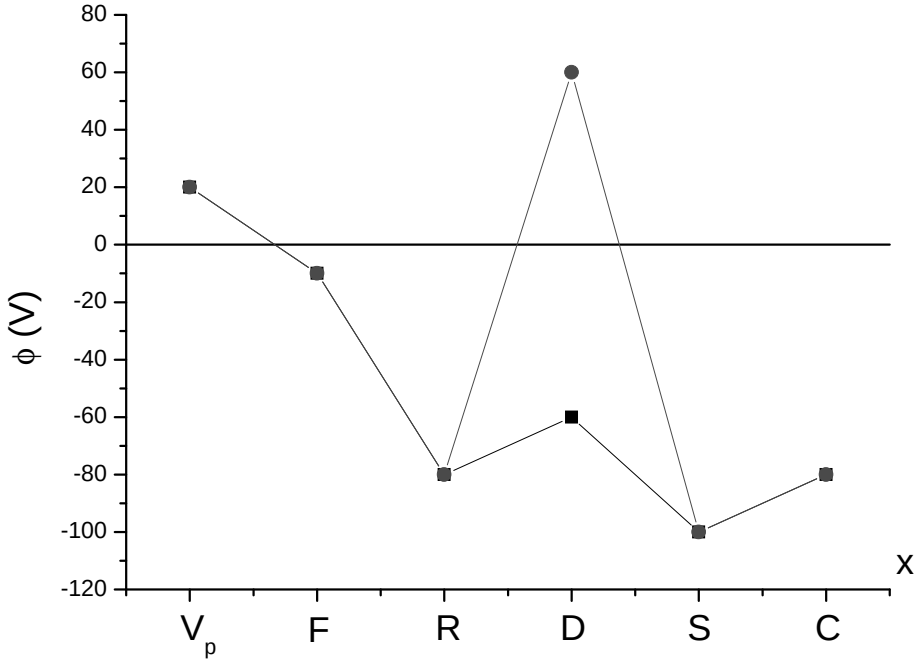

Figure 4.9: Grid voltages for the DC biased tests of the RFEA with an estimate of the plasma potential (V_p) and two different discriminator grid (D) voltages shown. The voltage on the RFEA body (F) was varied between -30 and 30 V.

sheath potential. These ions would experience very few collisions in the sheath and would arrive with trajectories close to perpendicular to the RFEA front surface. The spread of ions measured with energies extending down to 0 eV is attributed to ion collisions in the sheath and RFEA. From section 4.5.1, for argon at a pressure of 5 mTorr, the mean free path is 3.5 cm for hard sphere collisions and is 1.2 cm for charge exchange collisions. While these distances are larger than the sum of the sheath thickness and RFEA length, a number of ions will still undergo collisions in this region.

4.6.3 DC Biased RFEA Results and Discussion

The RFEA was DC biased with voltages between -30 and 30 V in an argon RF plasma at a pressure of 5 mTorr. A graph of the ion current versus discriminator voltage for the different bias voltages is shown in figure 4.11. The local plasma potential, which is given by the discriminator voltage at which the collector current first reaches its minimum value, decreases as the DC bias becomes more negative

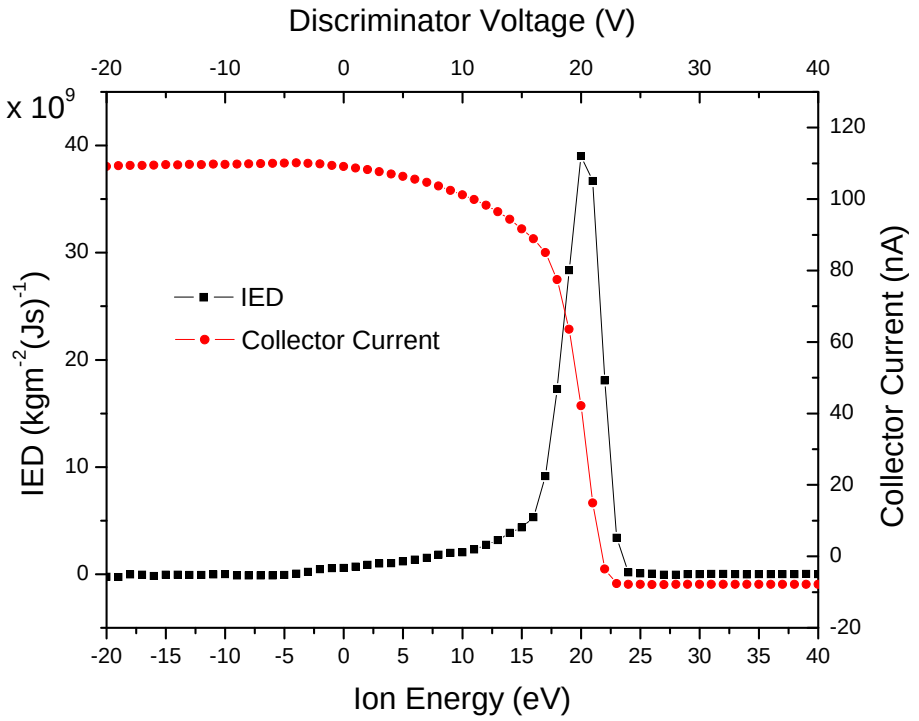

Figure 4.10: Ion current versus discriminator voltage graph and the IED obtained from this data using equation (4.5). Measurements were made with a grounded probe in an argon RF plasma at a pressure of 5 mTorr. The IED shows the majority of ions have an energy close to 20 eV and that the plasma potential is 24 eV.

and increases as the DC bias becomes more positive. Using equations (4.7) and (4.8), the average ion density and average ion flux for the different bias voltages were calculated and are shown in figure 4.12. As the bias voltage becomes more negative the ion density decreases below the value obtained when the RFEA was grounded and for positive biasing the ion density is greater than obtained with a grounded RFEA. Negative biasing of the RFEA results in very little change to the ion flux compared with the value measured with a grounded RFEA while positive biasing results in a small increase in ion flux.

The plasma potential is determined by the number of ions and electrons in the plasma. As the DC bias applied to the RFEA body becomes more negative, the sheath thickness around the RFEA increases which increases the plasma-sheath surface area. This results in more ions being drawn out of the plasma which lowers the plasma ion density and local plasma potential as seen in figures 4.11 and 4.12. Negative biasing also confines more electrons in the plasma which would also lower the

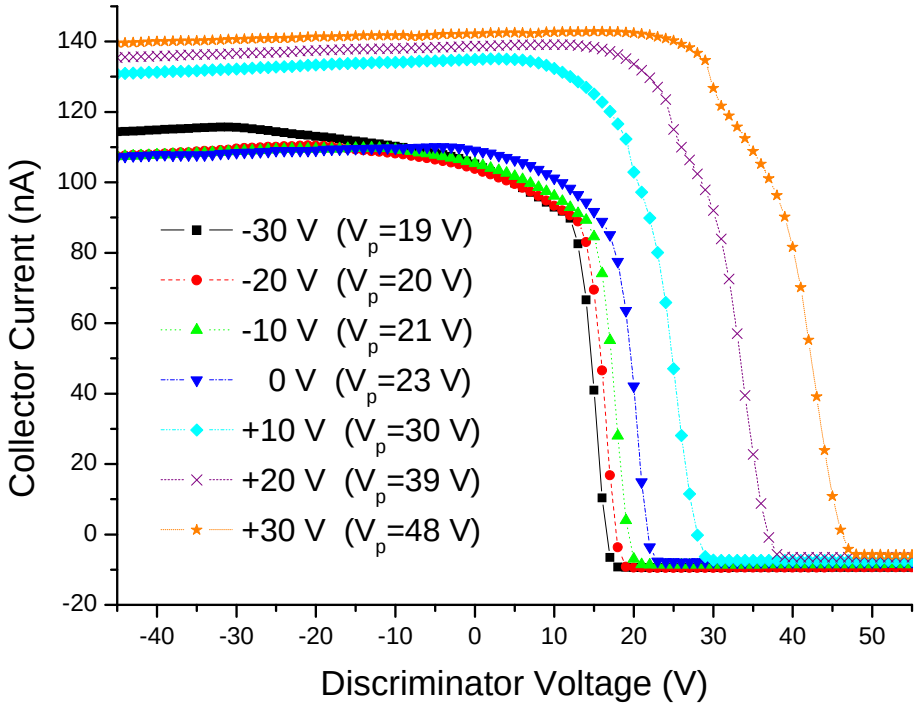

Figure 4.11: Ion current versus discriminator voltage graphs as a function of DC bias voltage applied to the RFEA. The local plasma potential (V_p) is measured as the point at which the ion current graph first reaches its minimum value. Measurements were made in an argon RF plasma at a pressure of 5 mTorr.

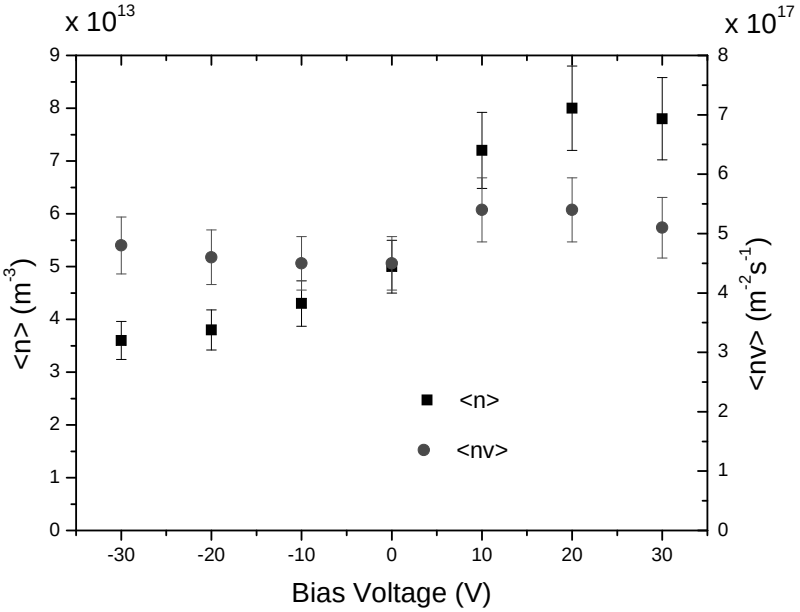

Figure 4.12: Average ion densities and ion fluxes as a function of DC bias applied to the RFEA in an argon plasma at a pressure 5 mTorr.

local plasma potential. Positive biasing of the RFEA reduces the sheath thickness around the RFEA which reduces the plasma-sheath surface area. This reduces the number of ions drawn out of the plasma and increases the ion density and plasma potential. Positive biasing also reduces the potential barrier confining electrons in the plasma which allows more electrons to escape to the RFEA surface and increases the local plasma potential. This increase in the local plasma potential acts to restore the potential barrier confining electrons in the plasma and balance the flux of electrons and ions to the RFEA surface. Negative biasing of the RFEA does not produce as large a change to the plasma potential or ion density as positive biasing. This may be due to most electrons which escape the plasma having an energy too large to be affected by the negative bias voltages tested in this work. For a 3 eV electron temperature, there would be a large number of electrons with energies less than 30 eV and biasing the probe positively allows many of these electrons to escape which would have a significant effect on the plasma potential.

The ion flux shows little change during negative DC biasing of the RFEA. Negative biasing would increase the plasma-sheath surface area and ion flux to the RFEA. However, it appears that this is balanced out by the reduction in ion density due to the increased depletion rate of ions from the plasma. The small increase in ion flux during positive DC biasing of the RFEA is attributed to the increased ion density produced by positive biasing of the RFEA.

A graph of the IEDs obtained for negative and positive DC biasing of the RFEA are shown in figures 4.13 and 4.14 respectively. During negative DC biasing, the maximum ion energy measured increases by slightly less than the applied bias voltage. This is explained by the increase in the sheath potential during negative biasing of the RFEA. For positive biasing, the maximum ion energy measured decreases slightly with increasing bias voltage. This is explained by the increase in the plasma potential with positive DC biasing of the RFEA. For all IEDs, peaks are measured close to the maximum ion energy which indicates that the majority of ions gain close to the maximum sheath potential. As discussed in section 4.6.2, the spread of ions with energies between zero and the maximum ion energy is attributed to ion collisions in the sheath and RFEA and due to the measurement of ions with

trajectories not perpendicular to the RFEA front surface. The small peaks close to 0 eV for bias voltages of 20 and 30 V indicate an increasing number of low energy ions as the DC bias voltage increases.

A graph of the effects of bias voltage on the mean random ion energy associated with motion perpendicular to the RFEA front surface is shown in figure 4.15. The mean random ion energy was obtained using equation (4.12). For negative DC biasing, the mean random energy increases as the bias voltage becomes more negative. For positive DC biasing, the mean random energy remains relatively unchanged with increasing bias voltage. The increase in the random energy as the bias voltage becomes more negative is explained by the increase in sheath thickness and the increased chance of ion collisions. During collisions, energy associated with the velocity component perpendicular to the RFEA front can be transformed to energy associated with velocity in random directions, increasing the mean random ion energy. During positive biasing, the sheath potential and sheath width decrease only slightly and the mean random ion energy remains relatively unchanged.

The experimentally measured ion densities were lower than typical materials processing plasma densities of the order of $1x10^{15}$ m^{-3}. Using equation (2.48), for a 20 V sheath with an electron temperature of 3 eV, a decrease in the ion density from $1x10^{15}$ m^{-3} to $5x10^{13}$ m^{-3} would increase the sheath thickness from approximately 1.3 to 6.0 mm. From section 4.5.1, for argon ions with a density of $5x10^{13}$ m^{-3} at 5 mTorr the sheath thickness will still be much less than the mean free path. This is seen in the IED results which show the majority of ions reaching the RFEA with close to the maximum sheath potential energy. The ion densities measured by the RFEA may be lower than expected due to ion losses in the RFEA and also due to the finite acceptance angle of the RFEA inlet aperture. Assuming that the RFEA inlet is approximately 3.5 mm deep and 4 mm wide the acceptance angle is 97.6 degrees.

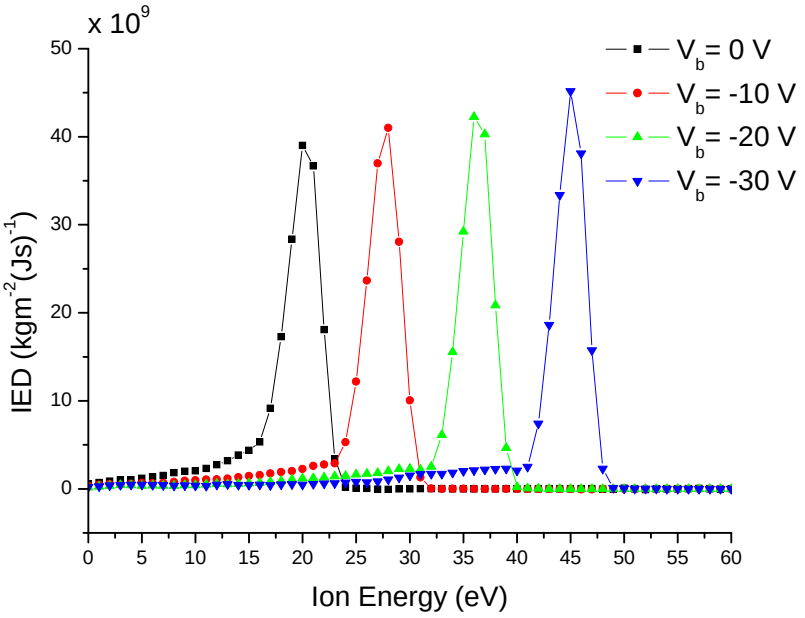

Figure 4.13: IEDs for different negative DC bias voltages (V_b) applied to the RFEA. Measurements were made in an argon RF plasma at a pressure of 5 mTorr.

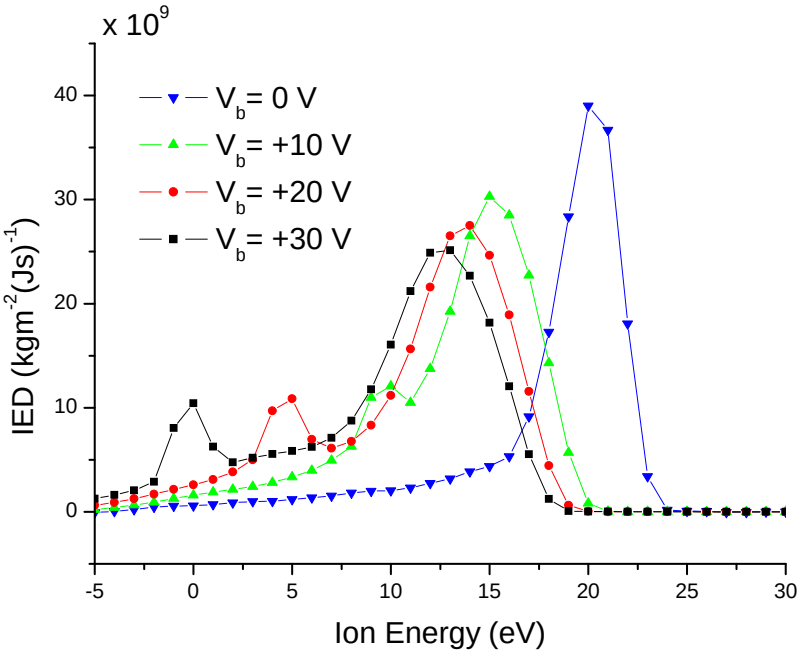

Figure 4.14: IEDs for different positive DC bias voltages (V_b) applied to the RFEA. Measurements were made in an argon RF plasma at a pressure of 5 mTorr.

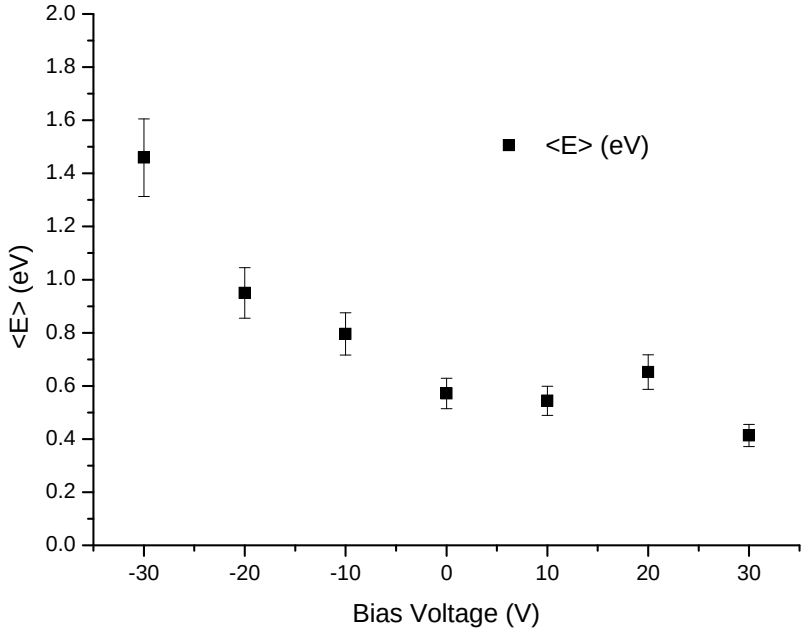

Figure 4.15: Mean random ion energies as a function of DC bias applied to the RFEA in an argon plasma at a pressure of 5 mTorr. Negative biasing increases the sheath width and the chance of ion collisions which increase the mean random energy of the ions.

4.7 Summary

The energy of ions arriving at a surface in a plasma are important in determining the extent of surface modifications and the properties of deposited thin films. Their ability to minimise the effects of secondary electron emission and their compact size give retarding field energy analysers (RFEAs) an advantage over Faraday cups and mass spectrometers for IED measurements. RFEAs use a series of electrically biased metal grids to repel plasma electrons and measure the energy of ions based on the component of their velocity perpendicular to the grid face. The IED can be obtained from the first derivative of the ion current versus the discriminating grid voltage. For this thesis, a RFEA was constructed with an outer body which could be pulse biased. The design of the RFEA considered the effects of ion collisions inside the analyser, aperture diameters, electrostatic lens effects at grid holes and space charge build up which determine the requirements for grid separation and grid hole size. When the RFEA was DC biased with negative voltages, the plasma potential and ion density decreased below values measured with the RFEA body grounded. This

is attributed to an increased depletion of ions from the plasma. Negative biasing increased the maximum energy of ions reaching the RFEA. For positive biasing, the plasma potential and ion density increased. Positive biasing of the RFEA results in a reduction in the maximum ion energy measured. The majority of ions are measured with energies close to the maximum sheath potential which indicates that most ions experience few collisions in the sheath and arrive with trajectories close to perpendicular to the RFEA front surface.

Chapter 5

Time Resolved Ion Energy Measurements During PIII

5.1 Introduction

This chapter describes results of time resolved ion energy measurements using a pulse biased RFEA in a capacitive RF argon plasma. This is the first application of a RFEA to time resolved ion energy measurements in PIII. In section 5.2, the experimental method used is discussed and in section 5.3, measurement results are presented. To further investigate experimental results, a two dimensional numerical simulation of ion trajectories in the sheath region near the front surface of the RFEA was performed. In section 5.4, the simulation method is discussed and in section 5.5, the results of these simulations are compared with experimental results.

5.2 Experimental Method

The experimental setup used is shown in figure 5.1. The vacuum chamber, RF power source and matching box were the same as used in section 4.6. The outer body of the RFEA was pulse biased using a GBS Electronik RUP 3-3a pulsed power supply. The pulse rise time was 70 ns and the pulse fall time was 80 ns.

To allow time resolved ion energy measurements, the RFEA collector current was measured as a voltage across a 1 kΩ resistor using the three stage amplifier

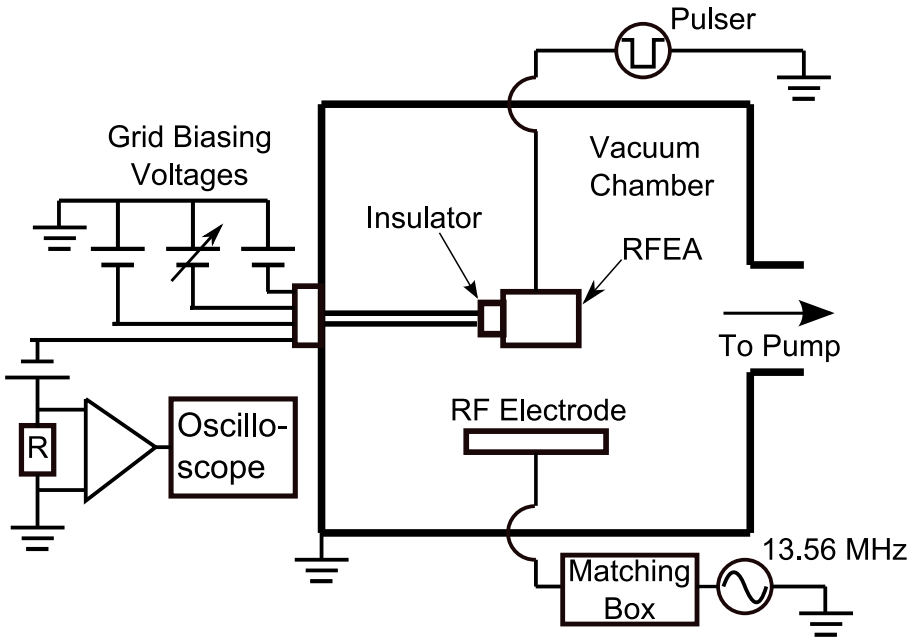

Figure 5.1: Experimental setup used for ion energy measurements using a pulse biased RFEA in a capacitive RF argon plasma at a pressure of 5 mTorr.

circuit shown in figure A.1 of appendix A. The circuit output was displayed on a Tektronix TDS2024 oscilloscope and recorded using a LabView computer program. Ion current measurements were averaged over 128 pulses to minimise the effects of electrical noise. The oscilloscope was triggered using the square wave signal input to the high voltage pulser which was supplied by a Datapulse 100A pulse generator.

The grid voltages used during -300 V pulsing of the RFEA are shown in figure 5.2. The probe body and front grid (F) were held at -300 V during the pulse-on period and at 0 V during the pulse-off period. The bias voltages on the RFEA grids were fixed during pulsing of the probe body. To allow ions to reach the collector, all grid voltages, with the exception of the discriminator, were kept more negative than the pulse amplitude. The repeller (R) was set to -320 V (20 V below the pulse amplitude) to repel plasma electrons during the pulse-off period. The discriminator was swept upwards from -340 V (40 V below the pulse amplitude) to 100 V (a range of 440 V) to control which energy ions were able to reach the collector (C) which was set to -320 V (20 V below the pulse amplitude) to attract ions. The suppressor (S) was set to -340 V (40 V below the pulse amplitude) to minimise the effects of

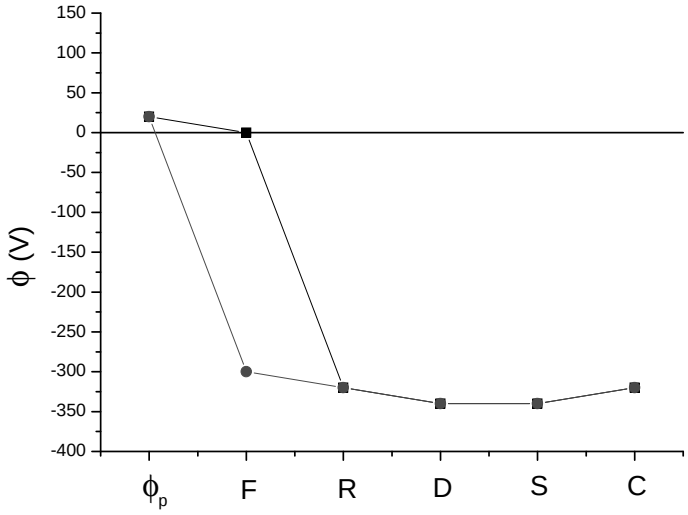

Figure 5.2: Grid voltages used during -300 V pulsing of the RFEA. The plasma potential (ϕ_p) is assumed to be 20 V. The front grid (F) was held at -300 V when the pulse was applied and at 0 V when the pulse was off. Ion current measurements were made at the collector (C) as the discriminator (D) was stepped upwards to 100 V.

secondary electron emission on ion current measurements.

The collector current was recorded using the oscilloscope for each discriminator grid voltage as the discriminator was stepped upwards to 100 V. The oscilloscope data was converted to ion current versus discriminator voltage data using a computer program written in GNU Octave and was graphed using the computer program Origin.

The time response of the RFEA circuit was determined by applying a square wave signal to the circuit and measuring the time constant of the output. The time constant measured was 9 μs. The time response of the circuit was also limited by currents induced when the pulse was switched on or off. Figure 5.3(a) shows the collector current measured when a -300 V pulse, with a width of 200 μs and period of 800 μs, was applied to the RFEA with no RF plasma present at a pressure of 5 mTorr. The grid voltages were $\phi_R = -320$ V, $\phi_D = 100$ V, $\phi_S = -340$ V and $\phi_C = -320$ V to repel plasma electrons and ions generated by pulsing of the RFEA body. Figure 5.3(b) shows an enlarged view of the collector current after the pulse was switched on. When the pulse switches on, a current is induced in the collector and the circuit takes approximately 25 μs to return to zero current. A similar time

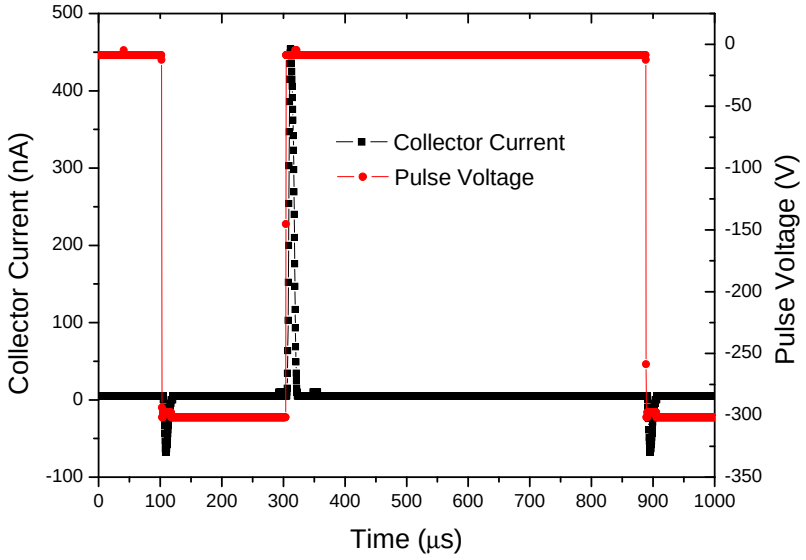

(a)

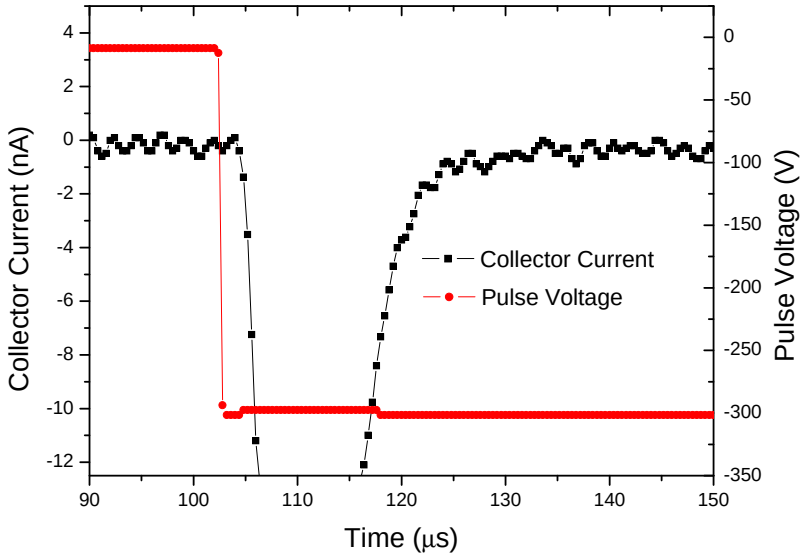

(b)

Figure 5.3: (a) RFEA collector current and pulse voltage for -300 V pulsing of the RFEA body with no RF plasma present and (b) an enlarged view of when the pulse is switched on. A current is induced in the collector when the pulse is switched on and off. The RFEA grid voltages were $\phi_R = -320$ V, $\phi_D = 100$ V, $\phi_S = -340$ V and $\phi_C = -320$ V.

is taken for the circuit to recover when the pulse is switched off. These induced currents created difficulties in interpreting the first 25 μs of data after the pulse switched on or off and data from these time periods was not used.

5.3 Experimental Results and Discussion

5.3.1 Ion Flux and Density

Ion energy measurements were made with -300 V pulses applied to the RFEA in a 150 W capacitive RF argon plasma at a pressure of 5 mTorr. The pulse width was 200 μs and the pulse period was 800 μs. Figure 5.4(a) shows the ion current and pulse voltage when a -300 V pulse was applied to the RFEA. An enlarged view of the ion current just after the pulse was switched off is shown in figure 5.4(b). The discriminator voltage (ϕ_D) was set to -340 V, allowing all ions to reach the collector. The negative current spike when the pulse was switched on and the positive current spike when the pulse was switched off are due to currents induced in the collector by the switching on or off of the pulse voltage. During the pulse-on period, the ion current rapidly increases during the first 20 μs before decreasing towards a steady state value. After the pulse switches off, the ion current drops rapidly over 30 μs before rising back to the steady state pulse-off value over a time of approximately 300 μs. The shape of the ion current graph is qualitatively similar to measurements made using a Faraday cup in an argon plasma with -2 kV pulses with pulse widths of 20 μs [61].

The mean ion densities and mean ion fluxes, obtained using equations (4.7) and (4.8), for different times during the pulse-on and pulse-off period are shown in figures 5.5(a) and 5.5(b). During the pulse-on period, the ion flux is larger than during the pulse-off period and during the pulse the flux decreases toward a steady state value. During the pulse-on period, the ion density is initially similar to the value at the end of the pulse-off period but during the pulse decreases to a value less than the pulse-off ion density. During the pulse-off period, the ion density increases to a steady state value over the first 300 μs after the pulse switched off.

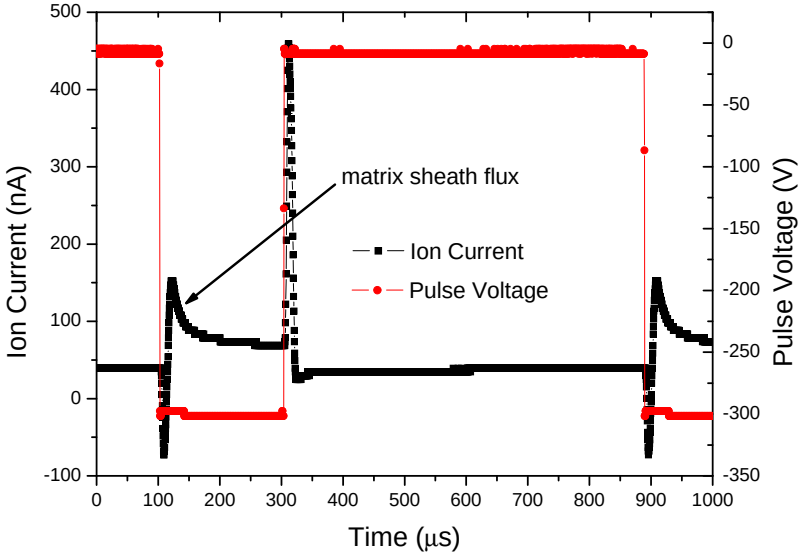

(a)

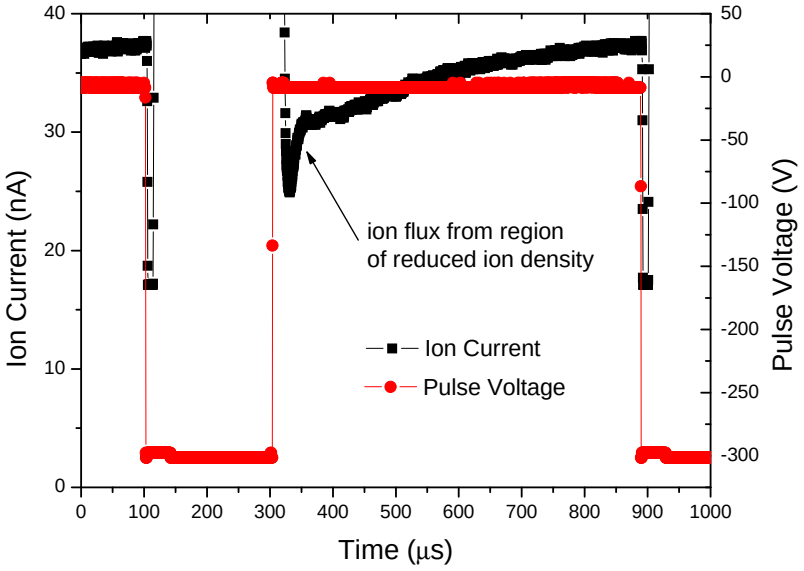

(b)

Figure 5.4: (a) Ion current and pulse voltage during -300 V pulsing of the RFEA in a plasma at 5 mTorr and (b) an enlarged view of the pulse-off ion current. The RFEA discriminator voltage was -340 V, allowing all ions to reach the collector. An increased ion flux at the start of the pulse is attributed to matrix sheath ions. After the pulse switches off, the decrease in ion flux below the background plasma value is attributed to measurement of ions from the region previously occupied by the -300 V sheath.

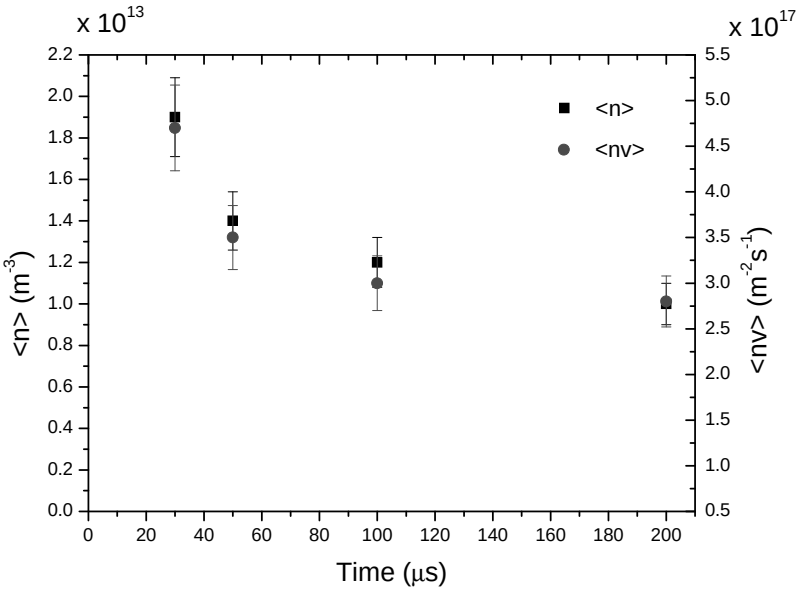

(a) Pulse-On

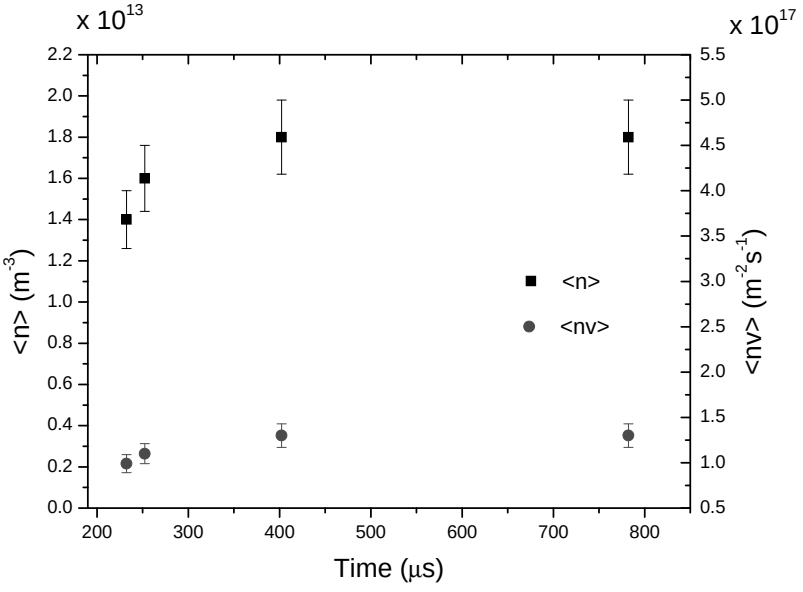

(b) Pulse-Off

Figure 5.5: Mean ion densities and mean ion fluxes during (a) pulse-on and (b) pulse-off periods as a function of time after application of a -300 V pulse to the RFEA in an argon plasma at a pressure of 5 mTorr. The pulse was switched on at t=0 μs and had a pulse width of 200 μs and period of 800 μs. At the start of the pulse, the larger flux values are attributed to measurement of ions from the matrix sheath. After the pulse switches off, reduced density and flux values are explained by measurement of ions from the region previously occupied by the sheath.

The larger ion flux measured during the pulse-on period is explained by the larger plasma-sheath surface area around the RFEA when the pulse is applied which draws in more ions from the plasma. The decrease in ion flux during the pulse-on period is attributed to the depletion of ions from the plasma by the pulse biased RFEA and occurs on a timescale much greater than required for the arrival of ions from the matrix sheath. An estimate of the time taken for the arrival of all ions from the matrix sheath and the time required for formation of a Child law sheath can be made using the Lieberman model discussed in section 3.4. The time taken for all matrix sheath ions to arrive can be estimated by substituting the matrix sheath thickness (s_0) for x_0 in equation (3.16) which describes the ion flight time. For argon ions with a density of 1x10^{13} m^{-3}, this gives a time of 1.9 μs for all matrix sheath ions to arrive. The time taken for the formation of the Child law sheath can be obtained by substitution of the equations for the matrix sheath thickness (2.40) and Child law sheath thickness (2.48) into equation (3.25) which describes the time taken for an ion to cross the sheath. For a -300 V pulse with argon ions at a density of 1x10^{13} m^{-3}, the time taken for Child law sheath formation is 19.2 μs. These times are much shorter than the time taken to approach a steady state ion current in the results in this work. The decrease in ion current during the pulse-on period indicates that the depletion rate of ions is greater than the generation rate of ions in the plasma during pulsing of the RFEA.

The ion density results during the pulse-on period support the idea that during pulsing, the depletion of ions is greater than the generation of ions in the plasma. During the pulse, after the first 20 to 30 μs, the ion density decreases below the value measured during the pulse-off period. This indicates that during pulsing, the larger plasma-sheath surface area around the RFEA allows it to collect a substantial ion current, lowering the plasma density. Secondary electrons accelerated into the plasma from the RFEA surface due to ion bombardment will cause ionisation which would increase the ion density. However, the increase in secondary electron energy produced by the larger sheath potential gives only a small increase in the electron ionisation cross section of argon [115]. It appears that for the measurements made in this work that the small increase in ionisation is overshadowed by the large depletion

of ions produced by pulse biasing of the RFEA.

During the pulse-off period, the measured ion flux is smaller than during the pulse-on period. This is explained by the relatively smaller plasma-sheath surface area around the RFEA which collects fewer ions. The depletion rate of ions is thus much lower during the pulse-off period, allowing the plasma density to rise towards its prepulse value. As shown in figure 5.4(b), after the pulse is switched off, the ion current drops below the value before the pulse was switched on before rising back to the steady state pulse-off value over a time of approximately 300 μs. This is explained by a combination of the measurement of ions from the region previously occupied by the pulse-on sheath and the reduced density of the plasma at the end of the pulse. The density of ions measured from the pulse-on sheath region will be less than from the bulk plasma. The time taken for the sheath thickness to collapse back to the pulse-off value is determined by the Bohm velocity (u_B) with a minimum time of $(s_{\mathrm{ON}} - s_{\mathrm{OFF}})/u_B$ where s_{ON} and s_{OFF} are the Child law sheath thicknesses when the pulse is on and off respectively [84]. For a -300 V sheath collapsing to a sheath with a potential of 20 V and an ion density of 1x10^{13} m^{-3}, the minimum time required is 33.1 μs. This is faster than the several hundred microseconds required for the ion current to return to close to the value before the pulse switched on observed in figure 5.4(b). The slow rise in ion current after the first 30 μs after the pulse switched off is attributed to the plasma requiring a longer time to recover from the ion depletion which occurred during pulsing of the RFEA.

5.3.2 Ion Energy

A graph of the IEDs obtained at different times during the pulse-on period are shown in figure 5.6. The maximum ion energy measured was 327 eV. For all of the IEDs, a peak is measured close to 314 eV and there is a spread of ions measured with energies between zero and the maximum ion energy.

The maximum ion energy measured of 327 eV represents ions which gained the energy of the full pulse potential plus the time averaged plasma potential. Using equation (2.103), the time taken for an ion to cross the sheath is over ten RF periods

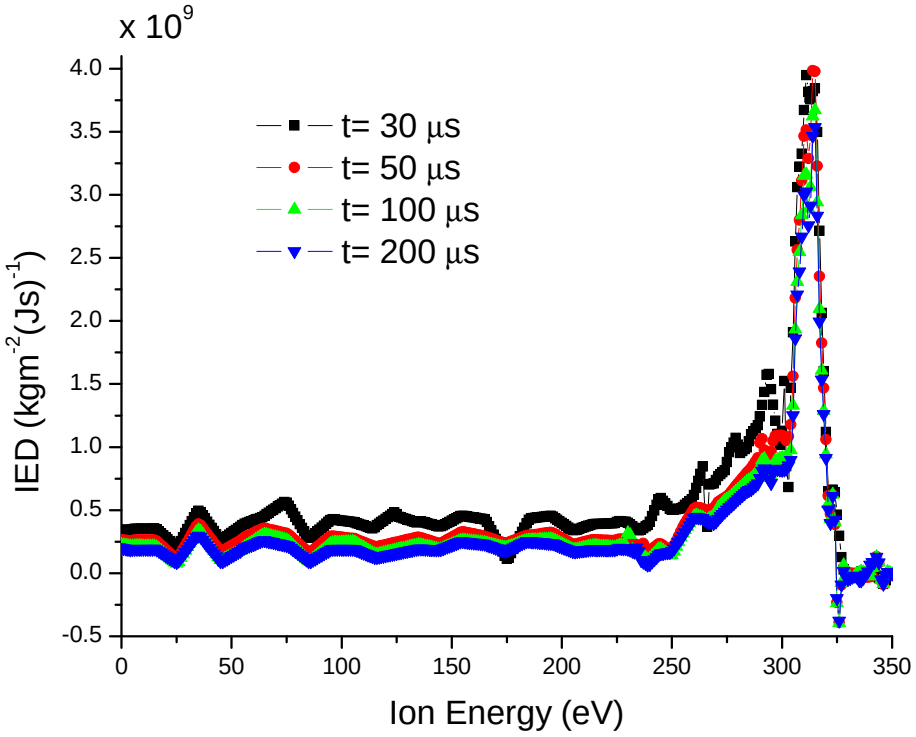

Figure 5.6: IEDs obtained at different times during application of a -300 V pulse to the RFEA in an argon plasma at 5 mTorr. The pulse width was 200 μs and the pulse period was 800 μs. The majority of ions have energies close to the maximum sheath potential of 327 V.

and ions will only experience the time averaged plasma potential. The high energy peak close to 314 eV indicates that a large number of ions gain close to the full sheath potential energy. These ions would experience very few collisions and would arrive at the RFEA with trajectories close to perpendicular to the RFEA front surface.

The spread of ion energies is attributed to ion collisions in the sheath and the measurement of ions with trajectories not perpendicular to the RFEA front surface. The RFEA discriminates ions based on the component of their velocity perpendicular to the RFEA front surface and ions arriving at an angle not equal to ninety degrees to the surface will be measured as having lower energy. At 5 mTorr, using equation (4.14), the mean free path for hard sphere collisions of argon ions is 3.5 cm. Using equation (2.48), for a -300 V Child law sheath with an ion density of 1x10^{-13} m^{-3} and an electron temperature of 3 eV the sheath thickness will be 10.2 cm. This is much larger than the hard sphere collision mean free path and

would produce IEDs with very few ions with close to the maximum sheath potential energy. The IED results in figure 5.6 show the majority of ions gain close to the full sheath potential energy and indicate that the ion densities determined using the IEDs are lower than the actual ion density. As discussed in section 4.6.3, this may be caused by ion losses in the RFEA and due to the finite acceptance angle of the RFEA inlet orifice. For an ion density of 1x10^{-14} m^{-3}, the Child law sheath thickness for a -300 V sheath with an electron temperature of 3 eV is 3.2 cm which is less than the hard sphere collision mean free path and would produce IEDs with the majority of ions with close to the maximum sheath potential energy. The area under the IEDs decreases during the pulse-on period due to the decrease in the ion flux to the RFEA. This flux decreases during the pulse-on period due to depletion of ions from the plasma by the pulsed RFEA body.

The mean random energies for different times during the pulse-on and pulse-off periods are shown in figures 5.7(a) and 5.7(b). The mean ion energy is significantly larger during the pulse-on period than in the pulse-off period. The larger mean ion energy during the pulse is explained by the larger sheath potential and sheath thickness during this period. The larger sheath potential will give the ions a larger velocity and the larger sheath thickness during the pulse-on period increases the chance of ion collisions in the sheath which will increase the randomly directed velocity components of the ions. During the pulse-off period the sheath thickness and sheath potential are smaller which reduces the velocity of ions reaching the RFEA and the number of collisions which they undergo in the sheath. This results in a much smaller mean random ion energy.

5.3.3 Effects of Pulse Amplitude

The effects of pulse amplitude were investigated by pulse biasing the RFEA in an argon plasma at a pressure of 5 mTorr with pulse amplitudes of -100, -200, -300 and -400 V. The pulse width was 200 μs and the pulse period was 800 μs. The mean ion densities and mean ion fluxes obtained 30 and 200 μs after the pulse switched on and 584 μs after the pulse switched off are shown in figures 5.8(a) and 5.8(b) as a

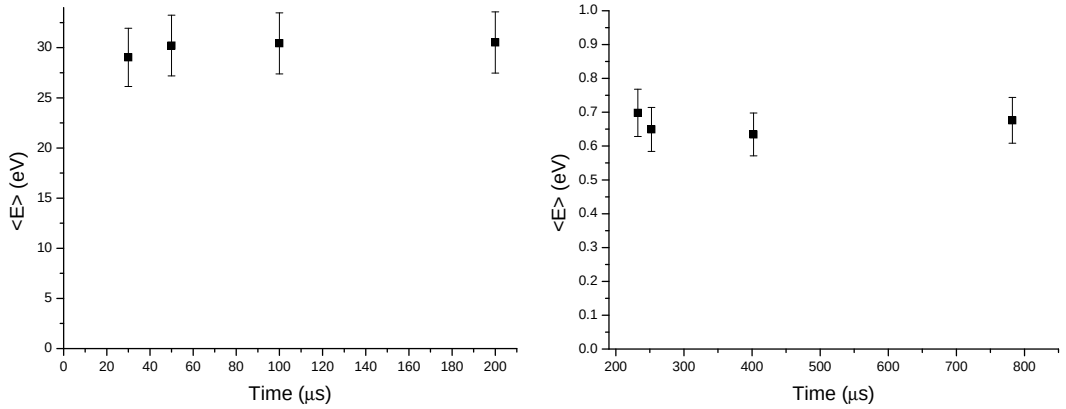

(a) Pulse-On (b) Pulse-Off

Figure 5.7: Mean random ion energies in the direction perpendicular to the RFEA front surface, during the (a) pulse-on and (b) pulse-off periods as a function of time after application of a -300 V pulse to the RFEA in an argon plasma at a pressure of 5 mTorr. The pulse width was 200 μs and the pulse period was 800 μs. The higher random energy during the pulse-on period is a result of ion collisions in the sheath.

function of pulse amplitude. During the pulse-on period, the ion flux is larger than during the pulse-off period and increases with increasing pulse amplitude. Both the ion flux and ion density at the start of the pulse-on period are larger than at the end of the pulse-on period. The ion density during the pulse-on period increases with increasing pulse amplitude but at the end of the pulse-on period remains lower than during the pulse-off period.

The larger ion flux during the pulse-on period compared to the pulse-off period is attributed to the larger plasma-sheath surface area around the RFEA during pulsing which draws in more ions from the plasma. As the pulse amplitude increases, the plasma-sheath surface area will also increase which will increase the measured ion flux. For all pulse amplitudes, the reduction in the ion flux at the end of the pulse-on period compared to the flux in the early stages of the pulse is attributed to the depletion of ions from the plasma by the pulse biased RFEA.

During the pulse-on period, the ion density increases with increasing pulse amplitude. For measurements made in the early stages of the pulse this is attributed to measurement of a larger number of ions from the matrix sheath. At the end of the pulse-on period the slight increase in ion density with increasing pulse amplitude is explained by increased ionisation in the plasma. With increasing pulse

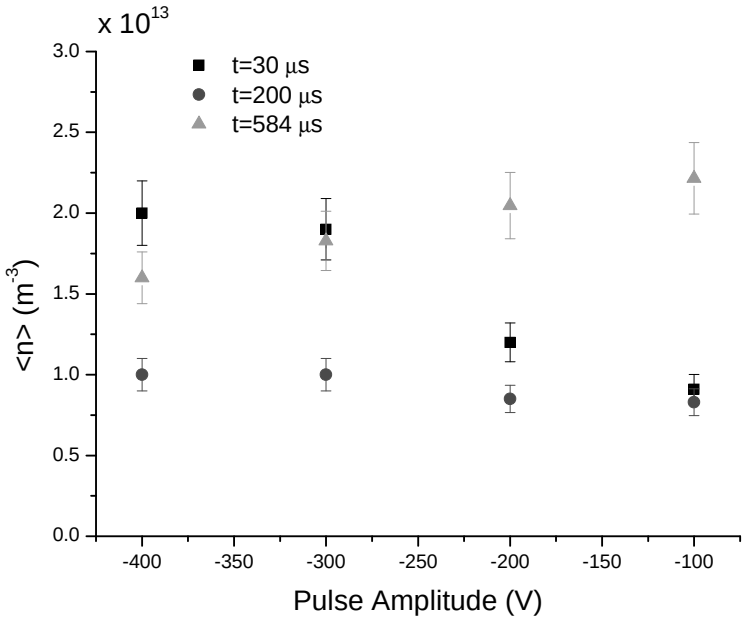

(a) Mean Ion Density

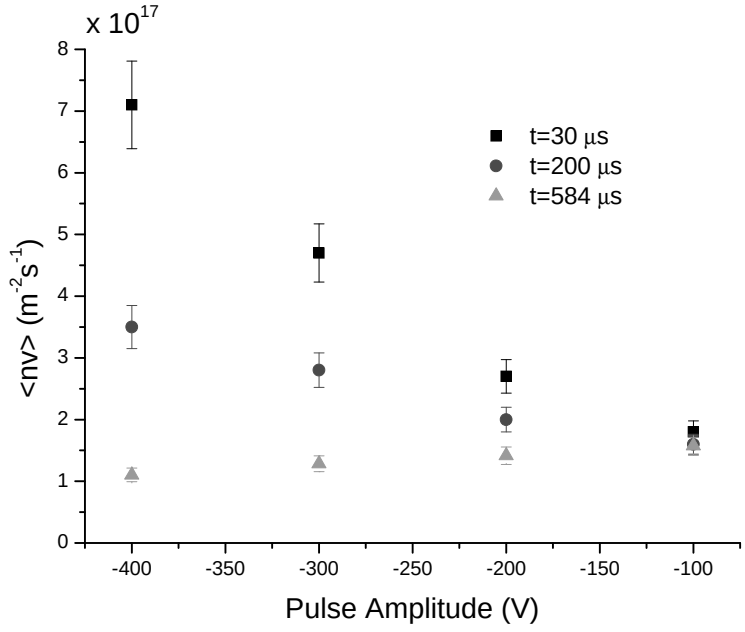

(b) Mean Ion Flux

Figure 5.8: (a) Mean ion densities and (b) mean ion fluxes as a function of pulse amplitude applied to the RFEA in a RF argon plasma at a pressure of 5 mTorr. The pulse width was 200 μs and the pulse period was 800 μs. Results were obtained 30 and 200 μs after the pulse switched on and 584 μs after the pulse switched off.

amplitude there will be an increasing flux of secondary electrons accelerated back into the plasma due to ion impacts on the RFEA. These electrons can ionise neutral argon atoms and increase the ion density. With increasing pulse amplitude, more such electrons will enter the plasma and there will be a greater chance of ionisation. The ion density during the pulse-off period remains larger than at the end of the pulse-on period. This indicates that the depletion rate of ions by the pulsed RFEA is greater than the generation rate of ions in the plasma for all biases tested. With increasing pulse amplitude, the ion density during the pulse-off period decreases. This indicates that the plasma has not fully recovered from the depletion of ions during the pulse-on period which would become larger as the pulse amplitude increases. This idea is supported by the observation that the ion densities measured during the pulse-off period were lower than those measured with a grounded RFEA in section 4.6.3.

A graph of the IEDs obtained for different pulse amplitudes, 30 and 200 μs after the pulse was switched on are shown in figure 5.9. With increasing pulse amplitude, the maximum ion energy measured increases. For all of the pulse amplitudes tested, the IEDs show a peak near the maximum ion energy and there are a number of ions measured with energies between zero and the maximum ion energy. For the IEDs obtained 30 μs after the pulse was switched on, as the pulse amplitude increases, the number of ions measured at all energies increases.

With increasing pulse amplitude, the sheath potential increases which will increase the energy of ions measured by the RFEA. For all pulse amplitudes, the peak produced close to the maximum ion energy indicates that the majority of ions are gaining close to the maximum sheath potential energy. These ions experience very few collisions in the sheath and arrive at the RFEA with trajectories close to perpendicular to the RFEA front surface. As discussed in section 5.3.2, the spread of ions measured with energies between zero and the maximum ion energy is attributed to ion collisions in the sheath and ions with trajectories not perpendicular to the RFEA front surface. For all pulse amplitudes, the area under the IEDs is larger for the IEDs obtained 30 μs after the pulse was switched on compared to the IEDs obtained at the end of the pulse-on period. This is caused by the larger ion flux at

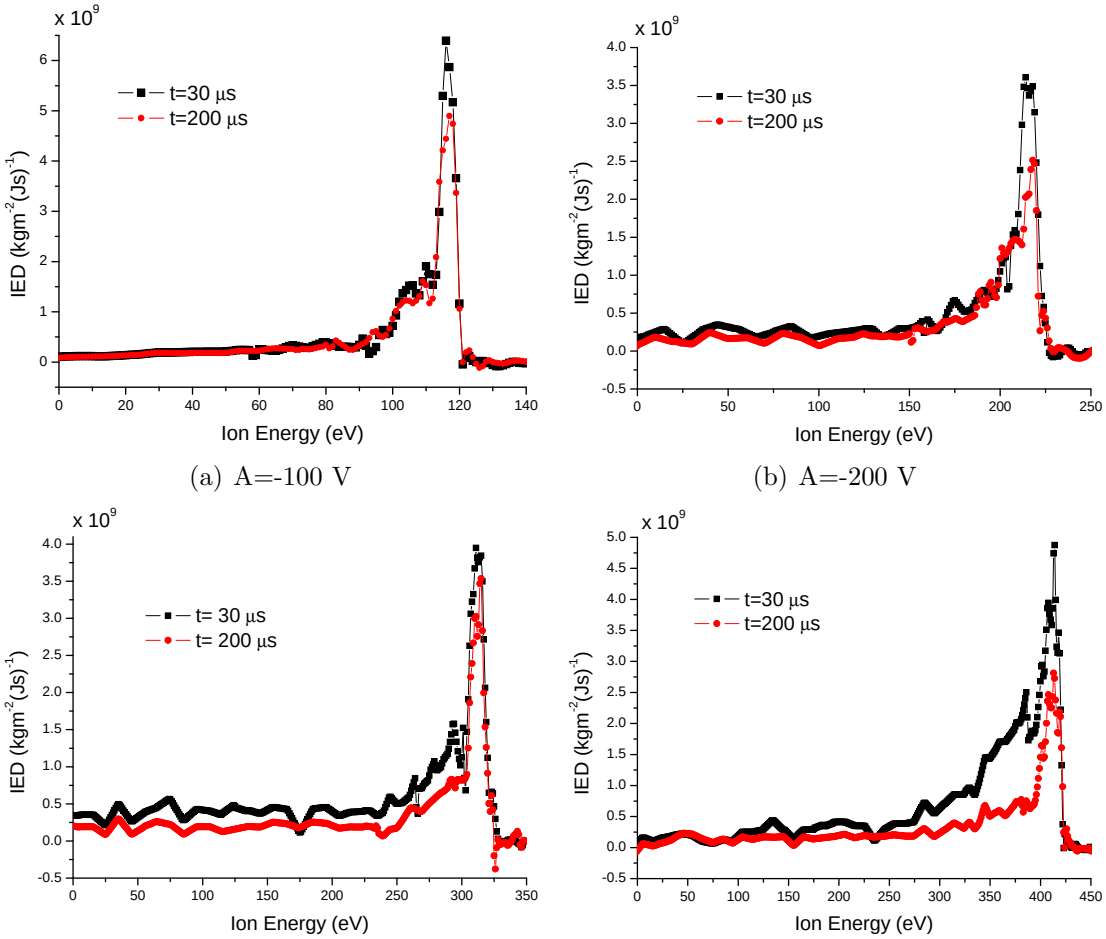

(a) A=-100 V (b) A=-200 V

(c) A=-300 V (d) A=-400 V

Figure 5.9: IEDs obtained during application of (a) -100 V, (b) -200 V, (c) -300 V and (d) -400 V pulses to the RFEA in an argon plasma at 5 mTorr. The pulse width was 200 μs and the pulse period was 800 μs. The IEDs were obtained 30 μs and 200 μs after the pulse switched on. For all pulse amplitudes, the majority of ions have energies close to the maximum sheath potential.

the start of the pulse-on period. This flux decreases during the pulse-on period due to depletion of ions from the plasma by the pulsed RFEA body.

A graph of the mean ion energies associated with motion perpendicular to the RFEA front surface, for different times during pulse-on and pulse-off, are shown in figure 5.10 as a function of pulse amplitude. During the pulse-on time, the mean ion energy increases with increasing pulse amplitude and during the pulse-off time it is smaller and remains relatively constant. The increase in the mean ion energy with pulse amplitude during the pulse is attributed to the increase in sheath potential and sheath thickness. The increase in sheath potential increases the velocity of ions

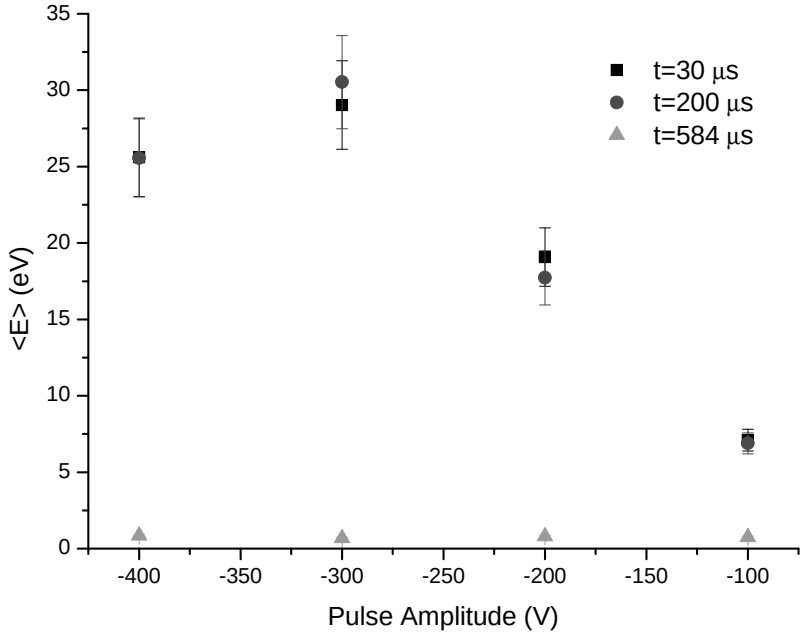

Figure 5.10: Mean ion energies associated with motion perpendicular to the RFEA front surface as a function of pulse amplitude taken 30 and 200 μs after the pulse switched on and 584 μs after the pulse switched off. The pulse width was 200 μs and the pulse period was 800 μs. As pulse amplitude increases, ions experience more collisions in the sheath which increases their mean random energy.

in the direction perpendicular to the RFEA front surface. The increase in sheath thickness increases the number of collisions ions undergo in the sheath which will increase their random velocity. During the pulse-off time, the RFEA body is at 0 V for all pulse amplitudes and the incoming ions have a much smaller velocity than during the pulse-on time. For the -400 V pulse, the mean ion energy decreases. This is attributed to the measurement of ions from the curved regions of the sheath above the RFEA corners which will start to have trajectories which allow them to reach the RFEA collector. Ions with non normal trajectories to the front of the RFEA will be measured by the analyser with less than the full sheath potential energy and this would lower the mean energy measured.

5.4 Simulation Method

A two dimensional, planar computer simulation of ion trajectories in the sheath region was performed to better understand experimental results. The sheath thick-

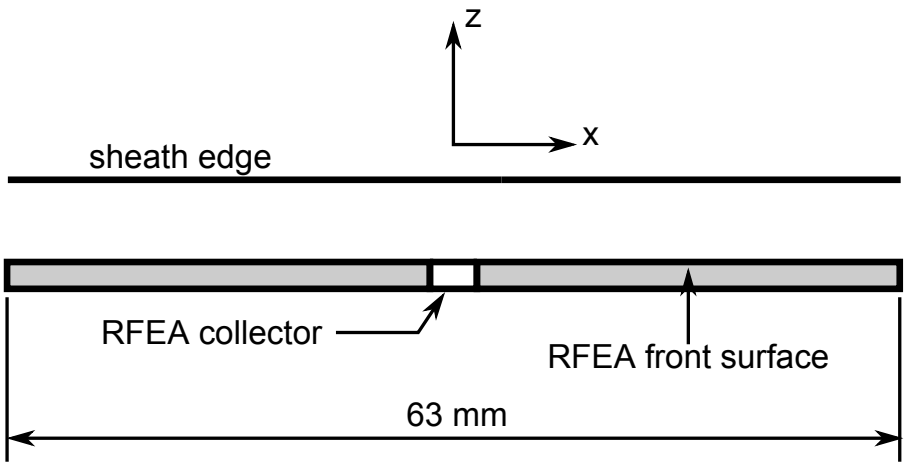

Figure 5.11: Setup of the xz plane used for the simulation of ion trajectories through the sheath region above the RFEA front surface.

ness and potential were approximated by the one dimensional Child law model using equations (2.48) and (2.49). The potential along the plasma-sheath edge was set to 0 V. Ions were launched into the sheath at uniform distances along the sheath edge and ions which reached the RFEA collector were used to construct the IED. Unlike more complicated particle in cell (PIC) simulations, ions were flown through the simulation individually and the position of ions was not used to determine the sheath potential after each time step.

The numerical simulations were performed using GNU Octave and were designed to study effects in the steady state Child law sheath. The sheath region was simulated as an xz plane with x in the plane of the front surface of the RFEA and z, the height above the front surface of the RFEA as shown in figure 5.11. The simulated region was centred on the inlet orifice of the RFEA and was 63 mm wide with potentials determined at 1 mm intervals. To simplify the simulation, the curvature and reduced thickness of the sheath above the RFEA corners was not taken into account.

5.4.1 Ion Motion

Ions were started at 0.05 mm intervals along the sheath edge in a 28 mm wide region centred above the RFEA inlet orifice. One thousand ions were launched from

each start point on the sheath. Each ion started at the Bohm velocity (u_B) with a trajectory perpendicular to the sheath edge. Ions were released individually into the sheath and their position and velocity determined at 0.01 μs intervals using the electric field (E) at each position. At each point in the potential array ($\phi(x, z)$), the electric field in the x and z directions was determined using the potential gradient around the point

$$E_x(x, z) = \frac{-\left(\phi(x + \Delta x, z) - \phi(x - \Delta x, z)\right)}{2\Delta x} \tag{5.1}$$

$$E_z(x, z) = \frac{-\left(\phi(x, z + \Delta z) - \phi(x, z - \Delta z)\right)}{2\Delta z} \tag{5.2}$$

where Δx and Δz are the 1 mm spacings in the x and z directions. For points on the simulation edges where potentials in the $\pm\Delta x$ or $\pm\Delta z$ direction were not all available, the electric field at (x, z) was determined using the potential gradient between $\phi(x, z)$ and its nearest available neighbouring points.

When the ion position (x, z) was not on a potential array point, the electric field was determined using a linear interpolation of the electric field at the nearest neighbouring array points as shown in figure 5.12. The electric field E_{12} at (x, z_1) was determined by linear interpolation between E_1 and E_2

$$\frac{E_{12} - E_1}{x - x_1} = \frac{E_2 - E_1}{x_2 - x_1} \tag{5.3}$$

A similar linear interpolation between E_3 and E_4 was used to determine E_{34} at (x, z_2). A linear interpolation between E_{12} and E_{34} was then used to determine the electric field at (x, z)

$$\frac{E - E_{12}}{z - z_1} = \frac{E_{34} - E_{12}}{z_2 - z_1} \tag{5.4}$$

For points which lay along the lines $x{=}x_1$, $x{=}x_2$, $z{=}z_1$ or $z{=}z_2$, the electric field was determined by a linear interpolation between the two nearest electric field points on the line.

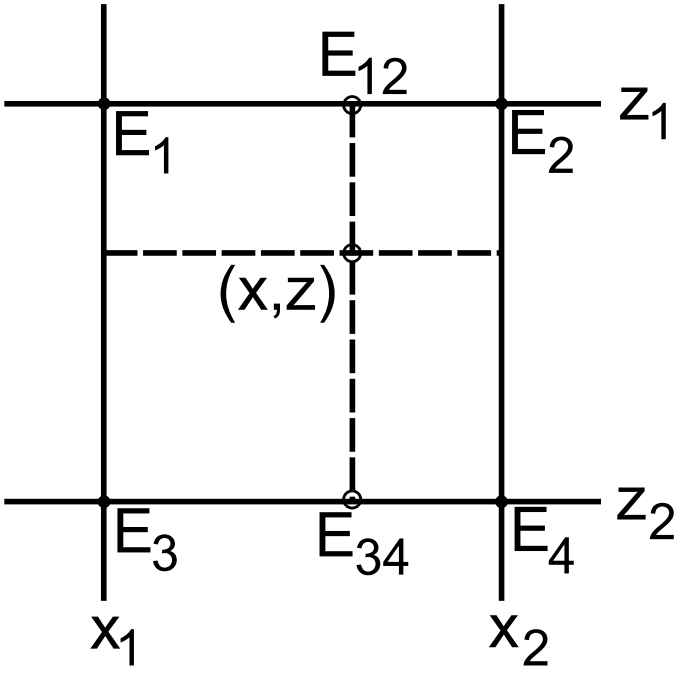

Figure 5.12: Linear interpolation method used to determine the electric field at a point (x,z) not on the potential array.

Using the electric field value, the acceleration (a) of the ion in the x and z directions was determined by substituting $F = qE$ into $F = Ma$, where F is the force, which gives

$$a_{x,z} = \frac{qE_{x,z}}{M} \tag{5.5}$$

where q is the ion charge and M is the ion mass. The displacement ($ds_{x,z}$) and final velocity ($v_{x,z}$) of the ion after each time step (dt) can be determined using the following equations of motion

$$ds_{x,z} = u_{x,z}(dt) + \frac{1}{2}a_{x,z}(dt)^2 \tag{5.6}$$

$$v_{x,z} = u_{x,z} + a_{x,z}(dt) \tag{5.7}$$

where $u_{x,z}$ is the ion velocity at the start of the time step. During each time step, the electric field on the ion in the x and z directions was determined based on the ion's

position and used to calculate the ion's displacement and velocity using equations (5.6) and (5.7). These values were then used to detemine the position and velocity of the ion for the next time step. This process was repeated until the ion experienced a collision with a neutral molecule or the RFEA or moved outside the simulation boundaries.

5.4.2 Collisions

A Monte Carlo approach was used to model collisions between ions and neutral molecules using the velocity independent mean free path (λ) given by equation (4.14). In a real plasma, the collision cross section of an ion, defined in equation (2.7), is dependent on the velocity of the ion. In figure 5.13, a comparison of collision cross section data as a function of ion energy is shown for argon ions in argon gas. The collision cross section data was determined using the computer program SRIM [160] for argon ions at a pressure of 5 mTorr, using experimentally determined values [29] and using equation (4.14) for argon ions. Over the ion energy range between 0 and 500 eV studied in this thesis, the velocity dependent and velocity independent collision cross sections are of the same order of magnitude. To simplify the simulations and reduce calculation time, the velocity independent collision cross section was used.

The probability ($f(x)$) that an ion will travel a distance x before experiencing a collision is given by equation (2.10)

$$f(x) = \left(\frac{\Gamma}{\Gamma_0}\right) = \left(\frac{1}{\lambda}\right) e^{-\frac{x}{\lambda}} \tag{5.8}$$

where the integral of $f(x)$ from 0 to $+\infty$ is equal to unity. The value $f(x)dx$ gives the probability that an ion will travel a distance between x and $x + dx$ without a collision. For a distance x, the distribution function $F(x)$ gives the fraction of ions which experience a collision between 0 and x. $F(x)$ has values between zero and one and is given by the integral of $f(x)$

$$F(x) = \int_0^x f(x)dx = 1 - e^{-\frac{x}{\lambda}} \tag{5.9}$$

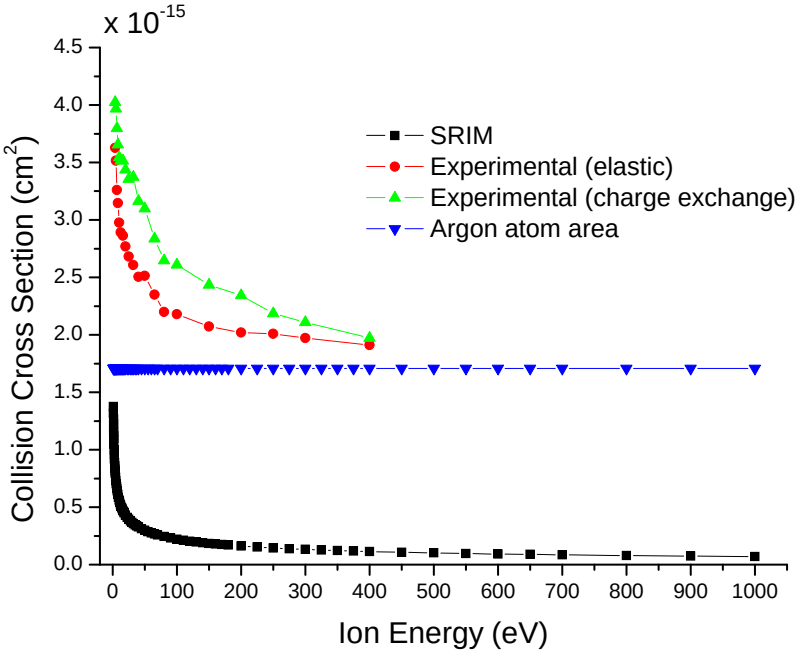

Figure 5.13: Comparison of collision cross section data as a function of ion energy for argon ions in argon gas at a pressure of 5 mTorr. The collision cross section was determined using the computer program SRIM [160], using experimental values [29] and using equation (4.14).

Rearrangement in terms of x gives

$$x = -\lambda \ln(1 - F) \tag{5.10}$$

In the simulations, the value of F was supplied by a random number generator in GNU Octave with a uniform distribution between zero and one. At the start of each ion's flight, equation (5.10) was used to determine the distance an ion was allowed to travel before a collision. If the ion had not reached the simulation boundaries before this distance, it was considered to have undergone a collision and the magnitude and direction of its velocity were recalculated and equation (5.10) was used to determine a new distance the ion could travel before a collision.

The magnitude and direction of the velocity of an ion after a collision with a neutral atom was determined by switching to a new reference frame. As shown in figure 5.14(a), the new axes are defined by the line joining the centres of the ion (m_1) and neutral atom (m_2) and a line perpendicular to this line through the point

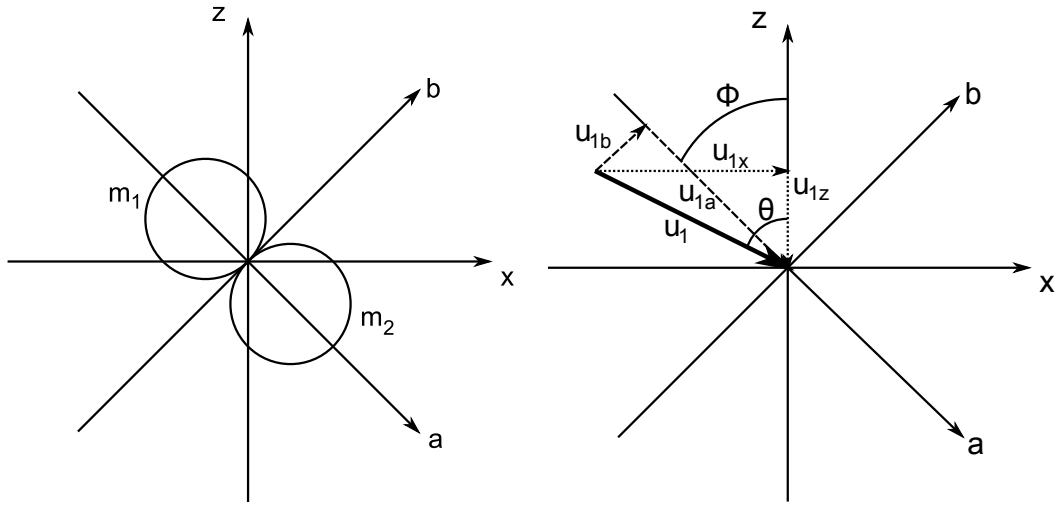

(a) (a, b) and (x, z) axes (b) Ion velocity in (a, b) and (x, z) coordinates

Figure 5.14: (a) The (a, b) axes are defined by the line joining the centres of the two masses and a line perpendicular to this line which passes through the point of contact between the two masses. (b) The angle (ϕ) between the two coordinate systems is used to calculate the magnitude and direction of the velocity of an ion (m_1) after a collision with a neutral atom (m_2).

where the two masses come into contact. In this reference frame, during a collision, the only velocities which need to be considered are along the line joining the two centres. The point on the neutral atom at which the ion makes contact will define the angle ϕ of the (a, b) axes relative to the laboratory axes (x, z). Assuming that the radii of the ion and neutral atom are both r, ϕ is defined by

$$\phi = \sin^{-1}\left(\frac{P}{2r}\right) \tag{5.11}$$

where P is a random number taken from a uniform distribution from $-2r$ to $2r$. In (a, b) coordinates, the initial velocity of the ion is given by

$$u_{1b} = u_1 \sin(\theta - \phi) \tag{5.12}$$

$$u_{1a} = u_1 \cos(\theta - \phi) \tag{5.13}$$

The neutral argon atom is assumed to be initially stationary. For an elastic collision between the ion and neutral atom, the following equations can be defined using

conservation of momentum and kinetic energy

$$m_1 u_{1a} + 0 = m_1 v_{1a} + m_2 v_{2a} \tag{5.14}$$

$$m_1 u_{1b} + 0 = m_1 v_{1b} + 0 \tag{5.15}$$

$$\frac{1}{2} m_1 u_1^2 + 0 = \frac{1}{2} m_1 v_1^2 + \frac{1}{2} m_2 v_2^2 \tag{5.16}$$

where

$$u_1 = \sqrt{u_{1a}^2 + u_{1b}^2}\ , \quad v_1 = \sqrt{v_{1a}^2 + v_{1b}^2}\ , \quad v_2 = v_{2a} \tag{5.17}$$

Assuming $m_1 \approx m_2$, it can be shown, using equations (5.14) to (5.17) that

$$v_{1a} = 0 \quad \text{and} \quad v_{1b} = u_{1b} \tag{5.18}$$

or

$$v_{1a} = u_{1a} \quad \text{and} \quad v_{1b} = u_{1b} \tag{5.19}$$

If $v_{1a} = u_{1a}$ then the neutral atom will not move after the collision and so solution (5.19) is not used. After the collision, the velocity of the ion is determined by converting solution (5.18) back into (x, z) coordinates

$$v_{1x} = u_{1b} \cos\phi \quad \text{and} \quad v_{1z} = u_{1b} \sin\phi \tag{5.20}$$

5.4.3 RFEA Acceptance Angle

An estimate of the effect of the RFEA acceptance angle on ion energy measurements was made by only measuring ions which reached the RFEA collector as shown in figure 5.15. The inlet diameter was set to 4 mm and the inlet depth was estimated to be 3.5 mm. The inside of the RFEA was approximated to be electric field free and

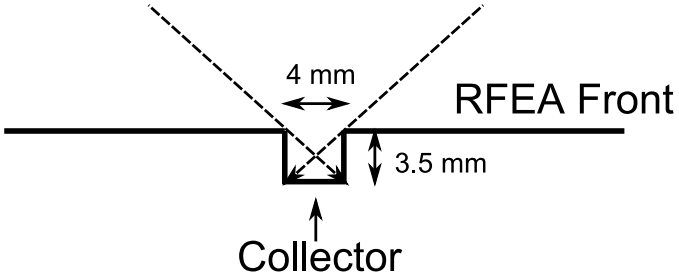

Figure 5.15: An estimate of the acceptance angle of the RFEA was made by only recording ions with trajectories which would have reached the collector.

only ions arriving at the RFEA front surface with trajectories which would reach the collector were recorded.

5.5 Simulation Results and Discussion

In figure 5.16, IEDs are shown from the simulation of a -300 V pulse applied to the RFEA with argon ions at a pressure of 5 mTorr. The IEDs were constructed using all ions which entered the RFEA inlet and using only ions which reached the collector. A total of $5.61 \text{x} 10^5$ ions were used and the height of the peak in the IED at 300 eV was 55690. The majority of ions had an energy of 300 eV and there is also a number of ions with energies between zero and the maximum ion energy of 311 eV. The ions with energies of 300 eV originated from the sheath directly above the RFEA inlet orifice. Ions with energies less than 300 eV experienced collisions in the sheath. Ions which collide with neutral atoms will reduce the component of their velocity perpendicular to the RFEA front surface, causing a spread in the measured energy distribution. Ions which collide more than once lose more of their velocity in the direction perpendicular to the RFEA front surface and have trajectories which do not allow them to reach the RFEA collector. This causes the difference between the collector only IED and the IED determined using all ions which enter the RFEA inlet. The maximum energy of ions was larger than the maximum sheath potential of 301.5 eV due to the pulse amplitude plus the energy associated with the Bohm velocity at which ions enter the sheath. This is due to the finite time step size used which can result in errors in the velocities of ions. Smaller time steps can reduce

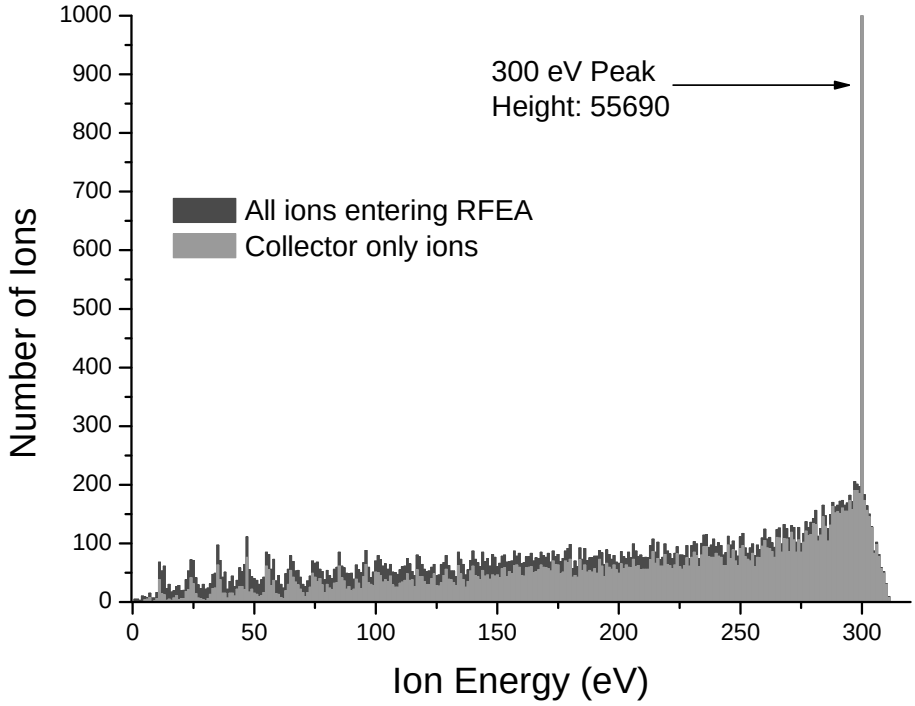

Figure 5.16: IEDs obtained from the simulation of a -300 V pulse applied to the RFEA at a pressure of 5 mTorr with argon ions. IEDs were constructed using all ions which entered the RFEA inlet and using only ions which reached the collector. The majority of ions have an energy of 300 eV and the height of the 300 eV peak is shown on the graph.

this error but significantly increase the time required to complete the simulations.

Comparison of experimental results in an argon plasma at 5 mTorr at the end of the -300 V pulse in figure 5.6 with simulation results in figure 5.16 show similarities in general trends. Both experimental and simulation IEDs show the majority of ions have energies close to the maximum sheath potential with a smaller number of ions with energies between zero and the maximum sheath potential energy. The results show that many ions undergo collisions in the sheath which reduce the component of their velocity perpendicular to the RFEA front surface. The large height of the 300 eV peak in the simulations, compared to the experimental IED results in figure 5.6, is caused by a number of factors. In the simulations, all ions enter the sheath at the Bohm velocity. In a real plasma, the ions entering the sheath will have a range of velocities equal to and above the Bohm velocity and this would spread the energy of ions reaching the collector and reduce the height of the peak in the

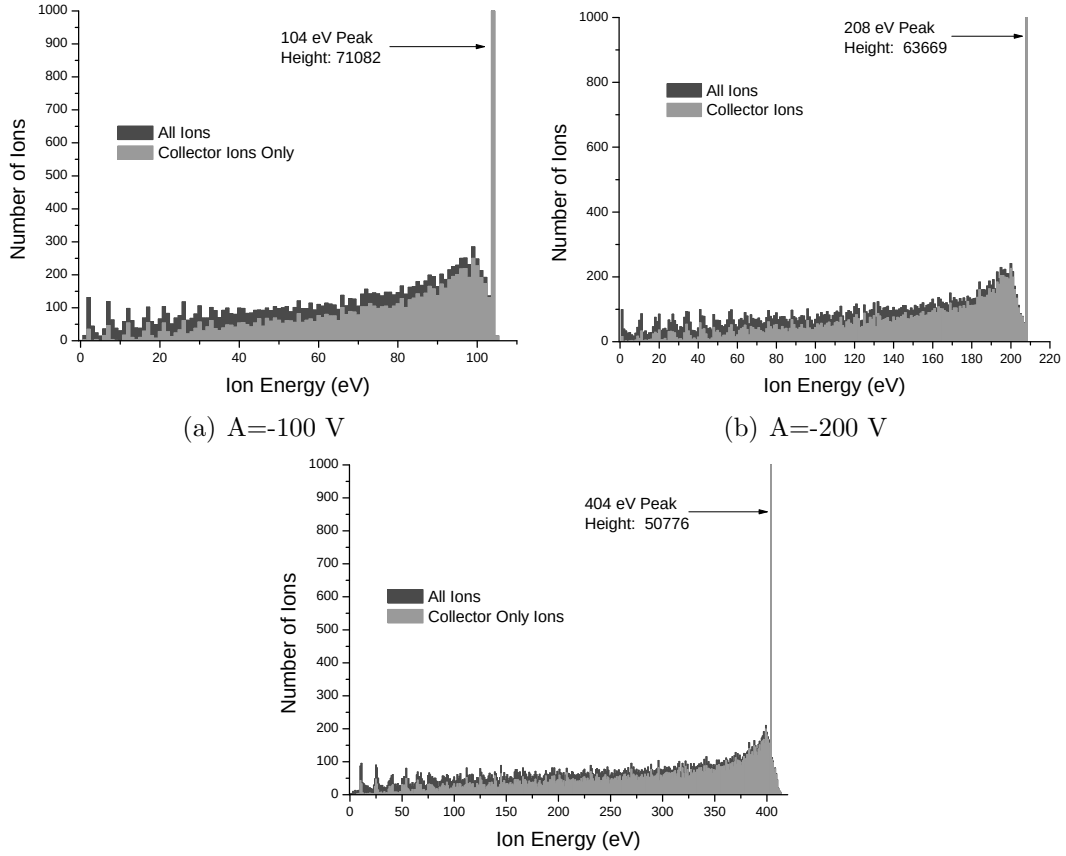

(a) A=-100 V

(b) A=-200 V

(c) A=-400 V

Figure 5.17: IEDs obtained from the simulation of (a) -100 V, (b) -200 V and (c) -400 V pulses applied to the RFEA at a pressure of 5 mTorr with argon ions. IEDs were constructed using all ions which entered the RFEA inlet and using only ions which reached the collector. For each pulse amplitude, a peak is observed close to the pulse amplitude energy. The actual heights of these peaks are shown in each graph.

IED. The large height of the 300 eV peak in the simulation results compared to the experimental IEDs may also be due to the larger ion density of 1x10^{15} m^{-3} assumed in the simulations which would give a narrower sheath thickness and less ion collisions in the sheath than the measured ion densities which were of the order of 1x10^{13} m^{-3}. The use of a velocity independent collision cross section may also have resulted in less low energy ions being measured in the simulations.

IEDs obtained from simulations of pulse amplitudes of -100 V, -200 V and -400 V are shown in figure 5.17. For all of the IEDs, a peak is observed close to the maximum sheath potential and there are a number of ions measured with energies between zero and the maximum sheath potential energy. The position of the IED

peak close to the maximum sheath potential energy indicates that most ions arrive from the sheath directly above the RFEA inlet and experience very few collisions in the sheath. The spread of ion energies between zero and the maximum sheath potential energy is produced by ions which collide in the sheath. Most ions which collide are still able to reach the RFEA collector but some ions experience a number of collisions which significantly alters their trajectories and results in their loss to the side walls of the RFEA. As for the -300 V results, the maximum ion energies are slightly larger than the maximum possible energy gained from the sheath potential plus the energy associated with the Bohm velocity due to the finite time step size used.

The experimental IED results at the end of the pulse-on period in figure 5.9 show similarities in general trends with the simulation results in figure 5.17. Both the simulation and experimental results show that at all pulse amplitudes, the majority of ions gain close to the maximum sheath potential energy and that a number of ions experience collisions in the sheath. The similarity in the shapes of the experimental and simulated IEDs verify that towards the end of the pulse, the sheath potential approaches the Child law sheath potential assumed in the simulation model. The experimental and simulated IEDs show a similar shape to IEDs obtained by other authors in capacitive argon RF plasmas at similar pressures where ion collisions in the sheath caused a spread in ion energy values measured [56, 85]. In the experimental results, the ion flux increased with pulse amplitude due to the increase in the plasma-sheath surface area and due to increased ionisation in the plasma. This effect cannot be observed in the simulations due to the assumption of a planar plasma-sheath edge and the equal number of ions used in each simulation.

5.6 Summary

In this chapter, the first time resolved measurements made using a pulse biased RFEA during PIII were presented. During pulsing, the measured ion flux is larger than during the pulse-off period but the ion density is lower. This is explained by the expanded plasma-sheath surface area around the RFEA during pulsing which

results in the depletion of ions being greater than the generation of ions in the plasma. After the pulse switches off, the ion density and flux drop below the values measured before the pulse switched on. This is attributed to measurement of ions from the region previously occupied by the pulse-on sheath. During the pulse-off period, the ion density remains less than measured during DC biasing of the RFEA which indicates that the plasma has not fully recovered from the depletion of ions which occurred during pulsing of the RFEA. With increasing pulse amplitude, the ion flux increases due to an increased plasma-sheath surface area. The ion density also increases slightly with increasing pulse amplitude and this is attributed to increased ionisation in the plasma.

With increasing pulse amplitude, the mean random energy of ions increased. This is explained by the increased sheath potential and increased chance of ion collisions in the sheath. IEDs showed a high energy peak close to the maximum sheath potential and a spread of ions with energies between zero and the maximum ion energy measured. The ion densities determined using the IEDs were lower than expected which may be caused by ion losses in the RFEA and due to the finite acceptance angle of the RFEA inlet orifice. Simulation results showed that the high energy peak is produced by ions from the sheath above the RFEA inlet and that the spread of ions with lower energies is produced by ions which collide in the sheath and/or arrive at the RFEA with trajectories not perpendicular to the RFEA front surface.

Chapter 6

Ion Energy Measurements During Mesh Assisted PIII

6.1 Introduction

For the PIII treatment of insulators, a conductive mesh can be placed around the object and pulse biased with the aim of minimising the effects of surface charging. In this chapter, a RFEA is used for the first time to investigate the effects of a metal mesh on the ion dose and energy during PIII of a metal surface. The experimental results are compared with those obtained from a two dimensional (r,z) numerical simulation. In section 6.2, the experimental setup used is discussed. Simulations were performed by calculating the trajectories of ions through the sheath and mesh regions and in section 6.3, the simulation method used is presented. In section 6.4, the effects of covering sections of mesh, pulse amplitude, mesh height and measurement position are investigated both experimentally and with simulation.

6.2 Experimental Method

The experimental setup used was the same as for the studies of pulse amplitude shown in figure 5.1. Measurements were made in a capacitive 13.56 MHz radio frequency (RF) argon plasma at a pressure of 5 mTorr. Stainless steel mesh cylinders with diameters of 36 mm and heights of either 1, 2 or 3 cm were attached to the

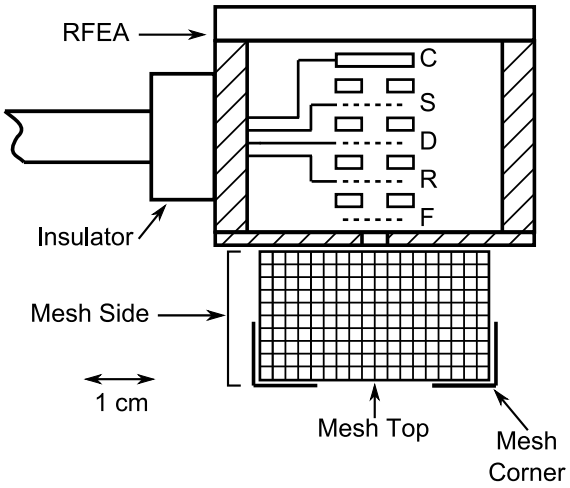

Figure 6.1: Cutaway diagram of the RFEA with a cylindrical mesh attached. The mesh diameter was 36 mm and the mesh height was either 1, 2 or 3 cm. The grids and spacers inside the RFEA are not drawn to scale.

front of the RFEA as shown in figure 6.1. The mesh thickness was 0.72 ± 0.02 mm with 1 mm square holes with a transparency of sixty nine percent. The RFEA inlet orifice was located at the centre of the mesh cylinder base. Both the RFEA and mesh were pulse biased with amplitudes ranging from -100 to -400 V.

Ion energy measurements were made using the same method described in section 5.2. Ion current was recorded at the collector using an oscilloscope for each discriminator grid voltage as the discriminator was stepped upwards from below the pulse amplitude to 100 V. Using this data, ion current versus discriminator voltage graphs were constructed for different times during the pulse-on period.

6.3 Simulation Method

A two dimensional, numerical simulation in cylindrical coordinates (r,z) was used to study the trajectories of ions in the sheath and mesh regions. The simulations were performed using GNU Octave.

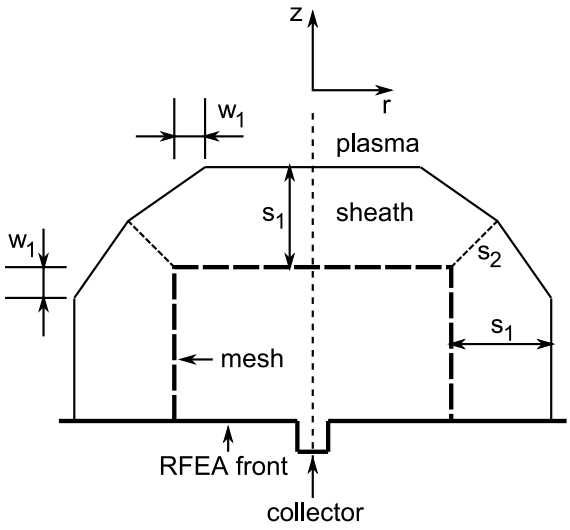

Figure 6.2: Sheath thicknesses used in the simulations. Above the planar regions of the mesh the sheath thickness was set to the one dimensional Child law value (s_1). Above the mesh corners a reduced sheath thickness (s_2) was used.

6.3.1 Sheath Edge

As shown in figure 6.2, above the planar sections of the mesh, the sheath thickness (s_1) was set to the one dimensional, planar Child law value given by equation (2.48). Around the mesh corners, the sheath thickness is less than the one dimensional Child law value [122, 146]. To approximate the reduced sheath thickness above the mesh corner, the sheath thickness along the bisector of the mesh corner (s_2) was set to seventy percent of the one dimensional Child law value based on the analytical solution of Donolato [34]. A linear interpolation between s_2 and s_1 was made between the mesh corner bisector and a point a distance w_1 into the planar sheath region. The distance w_1 was set to maintain a smooth sheath shape around the mesh corner and for the -100 V sheath was 3 mm, for the -200 and -300 V sheaths was 4 mm and for the -400 V sheath was 5 mm.

6.3.2 Potential Array

The potential in the sheath and mesh regions was determined by using the relaxation method to solve Poisson's equation, taking into account the decrease in ion density as the ions accelerate. The potential along the plasma-sheath edge was set to 0

V. Due to the cylindrical symmetry of the RFEA, the potential was solved in two dimensional (r, z) coordinates. The kinetic energy of an ion in the sheath is given by

$$\frac{1}{2}Mu^2(r,z) = -e\phi(r,z) + e\phi_s \tag{6.1}$$

where $u(r, z)$ is the ion velocity and $e\phi_s$ is the initial energy associated with the ion entering the sheath at the Bohm velocity (u_B) and is given by

$$e\phi_s = \frac{1}{2}Mu_B^2 \tag{6.2}$$

The ion flux is given by

$$en(r,z)u(r,z) = J_0 \tag{6.3}$$

The ion density is obtained by substitution of (6.1) into (6.3)

$$n(r,z) = \left(\frac{J_0}{e}\right)\left(\frac{2e}{M}\right)^{-\frac{1}{2}}(\phi_s - \phi)^{-\frac{1}{2}} \tag{6.4}$$

Due to the large negative voltages applied to the RFEA during pulsing, the electron density in the mesh and sheath is assumed to be zero. Substitution of (6.4) into Poisson's equation in cylindrical coordinates gives

$$\frac{\partial^2\phi}{\partial r^2} + \left(\frac{1}{r}\right)\left(\frac{\partial\phi}{\partial r}\right) + \left(\frac{\partial^2\phi}{\partial z^2}\right) = -\left(\frac{J_0}{\epsilon_0}\right)\left(\frac{2e}{M}\right)^{-\frac{1}{2}}(\phi_s - \phi)^{-\frac{1}{2}} \tag{6.5}$$

Equation (6.5) can be expressed as a finite difference equation and solved numerically for potential $(\phi(r, z))$. A more detailed description of the method used is given in appendix B. The equation for the potential array is solved using the relaxation method and the potential at (r, z) is dependent on the potentials of the points to the left and right $(\pm\Delta r)$ and above and below $(\pm\Delta z)$. For each iteration, the potential at every point is solved using the equations in appendix B and the process repeated until the largest difference in potential between iterations, at each array

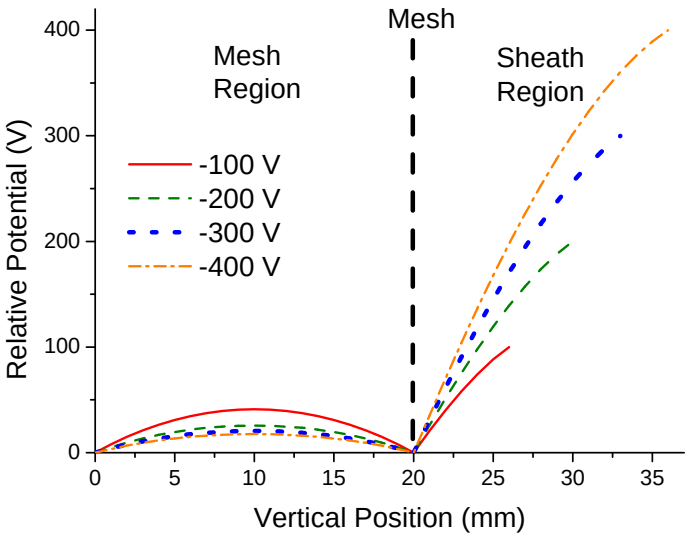

Figure 6.3: Simulation results for the relative potential (actual potential minus potential on mesh) versus vertical distance (z) along the centre line ($r = 0$) through a 2 cm high mesh for different potentials on the mesh. Inside the mesh a potential hump is produced by a space charge build up.

point, is less than 1x10^{-7} percent.

A graph of the relative potential (actual potential minus potential on the mesh), along the r=0 centre line in figure 6.2, for a 2 cm high mesh is shown in figure 6.3 for different potentials applied to the mesh. A space charge potential forms inside the mesh and is greatest for an applied potential of -100 V when the ions are moving at their slowest.

6.3.3 Ion Motion and Collisions

The motion of ions through the sheath and mesh regions was determined using the same method described in section 5.4.1. Ions were started at 0.05 mm intervals along the sheath edge, at the Bohm velocity, with trajectories perpendicular to the sheath edge. Ions were launched individually into the sheath and their position and velocity determined at 0.02 μs intervals using the electric field at each point. One thousand ions were launched from each start site on the sheath edge.

To account for the sixty nine percent transparency of the mesh, when an ion passed through the mesh it was given a random number from a uniform distribution from zero to one. Ions with a number greater than 0.69 were considered to have

collided with the mesh wires and were removed from the simulation.

Ion collisions were modelled using the same method described in section 5.4.2. The collisions were modelled as hard sphere collisions with neutral gas molecules using a Monte Carlo approach and velocity independent collision cross section.

The acceptance angle of the RFEA was accounted for by only measuring ions with trajectories which would have reached the RFEA collector, as shown in figure 5.15. For ions which reached the RFEA collector, the simulated IEDs were constructed using the component of velocity perpendicular to the RFEA front surface.

6.4 Results and Discussion

6.4.1 Effects of Covering Mesh Sections

A 2 cm high mesh was attached to the RFEA and pulse biased at -300 V with a square wave with a pulse-on time of 200 μs and period of 800 μs. Figure 6.4 shows the IEDs obtained 190 μs after the start of the pulse when different sections of the mesh were covered. The location of the covered mesh sections are as shown in figure 6.1. A high energy peak at 310 eV is observed for all IEDs except for the top covered mesh. The position of the high energy peak close to the maximum ion energy of 330 eV indicates many ions experienced very few collisions and gained close to the maximum sheath potential of the pulse amplitude plus the time averaged plasma potential. The plasma potential oscillates on a timescale much faster than the time taken by an ion to cross the sheath [59] so that ions will only experience the time averaged plasma potential. The number of ions in the high energy peak is only slightly affected by covering the mesh sides or corners. A medium energy peak is observed at 175 eV. This peak decreases in size when the mesh sides are covered and disappeared when a 1 cm section around the mesh corners was covered. A low energy peak close to zero energy, observed when the mesh sides were covered is believed to be low energy ions trapped by the covered side walls and the potential hump observed inside the mesh in figure 6.3. When the mesh cylinder top is covered almost no ions are measured.

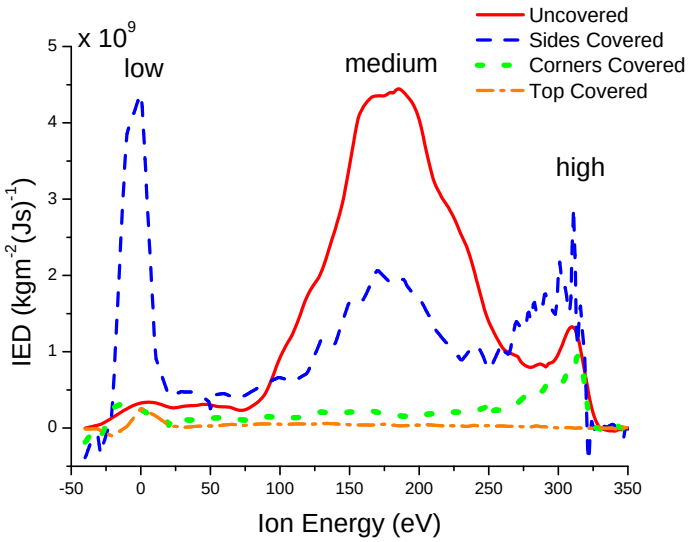

Figure 6.4: IEDs obtained when different sections of a 2 cm high mesh were covered during PIII with a -300 V pulse with a pulse-on time of 200 μs and period of 800 μs. The location of the covered mesh sections are as shown in figure 6.1. IEDs were obtained 190 μs after the start of the pulse.

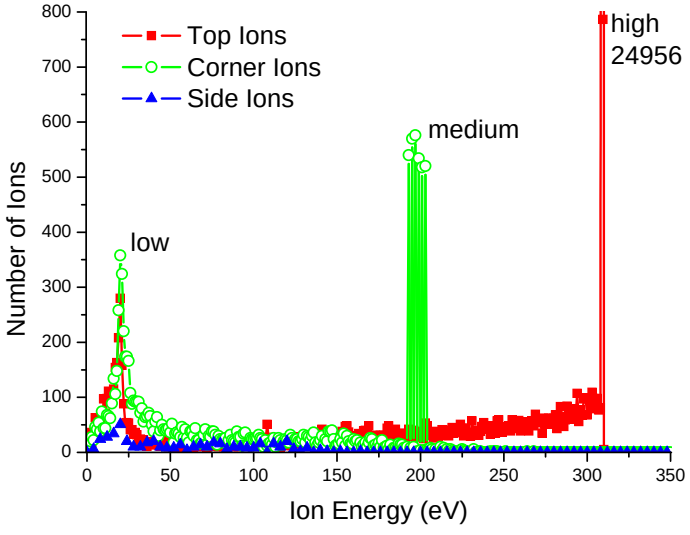

Figure 6.5: Simulation results showing the components of the IED obtained for a -300 V pulse applied to a 2 cm high cylindrical mesh and the RFEA at a pressure of 5 mTorr. The height of the high energy peak at 309 eV was 24956.

The mean ion flux for the uncovered mesh IED was (13 ± 1) x 10^{17} $m^{-2}s^{-1}$ which was larger than the no mesh IED value of (2.8 ± 0.3) x 10^{17} $m^{-2}s^{-1}$, in figure 5.5(a), for the same pulse conditions. This is explained by the larger plasma-sheath surface area around the mesh which results in a larger number of ions collected. The IEDs obtained with a mesh on the RFEA have a different shape with a significant number of ions with less than the maximum sheath potential energy.

Figure 6.5 shows the simulation results for the origins of the components of the IED obtained for a -300 V pulse applied to a 2 cm high cylindrical mesh and the RFEA at a pressure of 5 mTorr. The high energy peak at 309 eV has a height of 24956 and is due to uncollided ions originating from the sheath above the mesh top. The large height of this peak compared to the rest of the IED is due to the assumption that all ions enter the sheath at the Bohm velocity. In a real plasma, ions enter the sheath with a range of velocities greater than the Bohm velocity and this would spread the high energy peak and reduce its height. The peak position is slightly larger than 300 eV due to the finite time step size used in the simulations which results in small errors in the ion velocity. Smaller time steps can reduce this error but significantly increase the time required for each simulation. The majority of ions from the sheath sections above the mesh corners which reach the RFEA collector do not collide and form a medium energy peak at 200 eV due to their off normal incidence. While these ions have both a r and z component to their velocities, the RFEA only discriminates ions based on the z component of their velocity. Ions from the top and corner sheath sections with energies less than these peaks have undergone collisions in the sheath and/or mesh regions. The low energy peak at 20 eV is due to ions which collided inside the mesh on the probe side of the 20 V potential hump shown in figure 6.3. Ions from the side sections of the mesh do not contribute significantly to the IED. These results help explain the origins of the high, medium and low energy peaks in figure 6.4. The high energy peak is caused by ions originating from the sheath edge directly above the RFEA inlet, the medium energy peak are ions from above the mesh corners and the low energy peak is due to ions trapped by the potential hump formed inside the mesh. The collision of ions inside the mesh and sheath regions causes a spread in ion energies from zero to the

maximum sheath potential.

6.4.2 Effects of Pulse Amplitude

The effects of pulse amplitude on the IED were investigated using a 2 cm high mesh and pulses with a pulse-on time of 200 μs and a period of 800 μs. The IEDs obtained 190 μs after the pulse switched on are shown in figure 6.6. For each IED, a high energy peak was observed close to the maximum ion energy which indicates that the majority of ions gained close to the maximum sheath potential of the pulse amplitude plus the time averaged plasma potential. For the -200, -300 and -400 V IEDs, medium energy peaks occurred at 98, 175 and 298 eV respectively. Low energy peaks are also observed close to 0 eV for both the -100 and -200 V IEDs. The low energy peaks are believed to be due to ions which have collided and are trapped by the potential hump inside the mesh seen in figure 6.3. The relative height of this potential hump is more significant for the -100 and -200 V pulses and affects their IEDs more than for the -300 and -400 V IEDs.

Figure 6.7 shows the simulation results for the effects of pulse amplitude on the IED for a 2 cm high cylindrical mesh at a pressure of 5 mTorr. For each amplitude, high energy peaks are seen close to the pulse amplitude energy. These represent uncollided ions from the sheath above the top section of mesh. Additional medium energy peaks are observed at 77, 134, 197 and 264 eV for the -100, -200, -300 and -400 V IEDs respectively. These represent uncollided ions which originated from the sheath sections above the mesh corners. While these ions have both a r and z component to their velocities the analyser only discriminates the ions based on the z component of their velocities. The low energy peaks formed between 0 and 65 eV represent ions which collided on the probe side of the potential hump inside the mesh region. These results help explain the IED structure seen in figure 6.6. The high energy peaks are caused by ions from directly above the analyser inlet, the medium energy peaks are caused by ions from above the mesh corners and the low energy peaks are caused by ions trapped by the potential hump inside the mesh. The broad structure of the -100 V IED in figure 6.6 is due to the large height of the

potential hump inside the mesh region for the -100 V pulse.

A graph of the mean ion densities and mean ion fluxes for the IEDs in figure 6.6 are shown in figure 6.8 as a function of pulse amplitude. As the pulse amplitude increases, the mean ion flux increases. This is attributed to the increase in the plasma-sheath surface area around the mesh. The mean ion densities are larger than those measured with no mesh, shown in figure 5.8(a). This may be due to a larger flux of secondary electrons emitted back into the plasma when a mesh is used which could increase ionisation and ion density. As the pulse amplitude increases, the flux of ions to the mesh and RFEA would increase which would increase secondary electron emission and ionisation. The ion density is largest for the -200 V pulse and decreases for the -300 V and -400 V pulses. This may be due to the depletion of ions by the larger plasma-sheath surface area at these amplitudes being greater than the generation rate of ions in the plasma.

6.4.3 Effects of Mesh Height

The effects of mesh height were investigated for a -300 V pulse with a period of 800 μs and a pulse-on time of 200 μs. The IEDs obtained for cylindrical meshes of various heights 190 μs after the pulse switched on are shown in figure 6.9. A high energy peak is measured at 312 eV for all mesh heights and is close to the maximum ion energy measured. The decrease in height of this peak with increasing mesh height is attributed to the greater distance travelled by ions through the mesh region which increases their chance of experiencing a collision which will reduce their velocity in the z direction perpendicular to the RFEA front surface. For the 2 and 3 cm high meshes, medium energy peaks are also observed at approximately 175 and 250 eV respectively. These peaks are not seen in the IEDs for the 1 cm high mesh and no mesh results. As the mesh height increases, the number of ions in the medium energy peak increases and this is attributed to an increase in the plasma-sheath surface area around the mesh with increasing mesh height.

Figure 6.10 shows the simulation results for the effects of mesh height on the IEDs obtained for a -300 V pulse at a pressure of 5 mTorr. For all mesh heights, a high

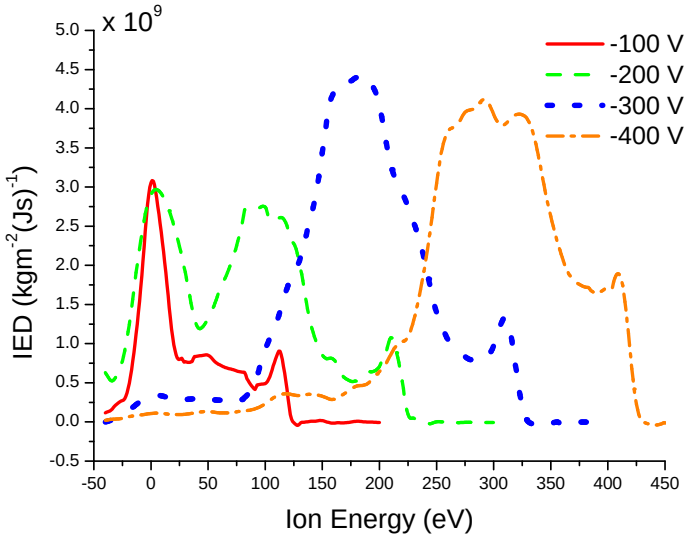

Figure 6.6: IEDs obtained 190 μs after the pulse switched on for different pulse amplitudes applied to the RFEA and a 2 cm high mesh in an argon plasma. The pulse period was 800 μs and the pulse-on time was 200 μs.

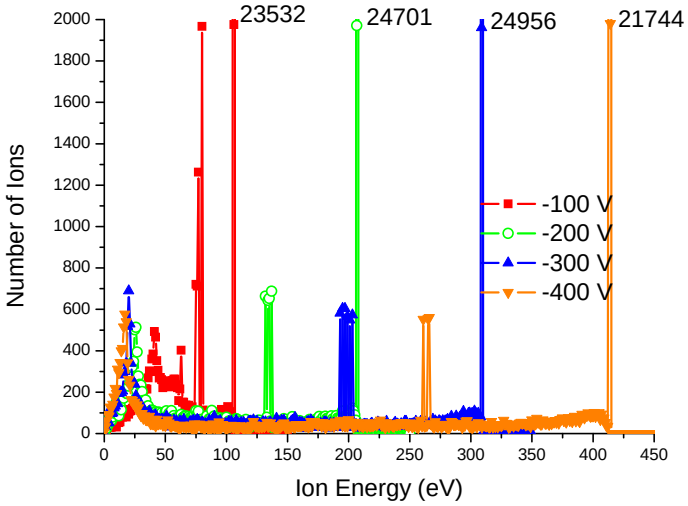

Figure 6.7: Simulation results showing the effects of pulse amplitude on the IEDs obtained using a 2 cm high cylindrical mesh at a pressure of 5 mTorr. The heights of the high energy peaks are shown next to each peak.

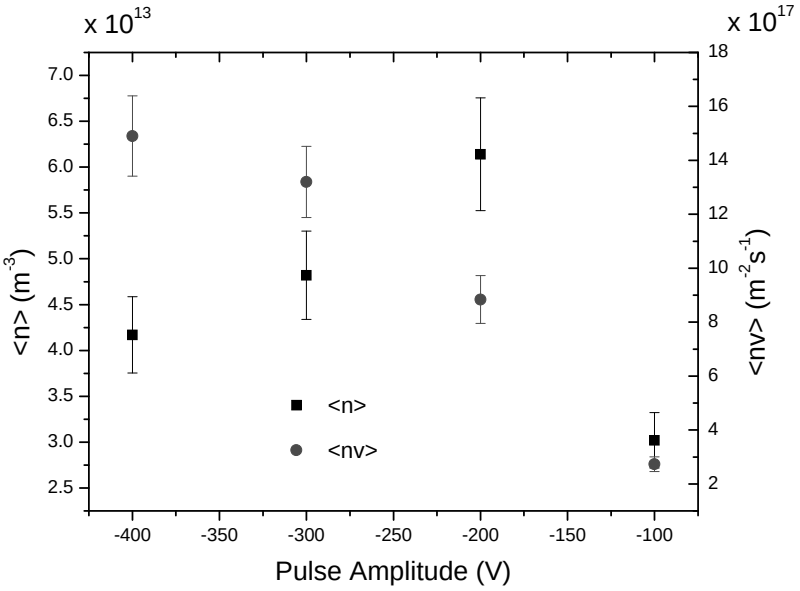

Figure 6.8: Mean ion densities and mean ion fluxes, as a function of pulse amplitude, for the IEDs in figure 6.6 using a 2 cm high cylindrical mesh. Measurements were made 190 μs after the application of a pulse with a period of 800 μs and pulse-on time of 200 μs.

energy peak is seen close to 305 eV which is caused by uncollided ions originating from the sheath section directly above the probe inlet aperture. When a mesh is present, the height of this peak decreases due to ion losses to the mesh. The peak height also decreases with increasing mesh height due to increased ion collisions in the mesh. For the 2 and 3 cm high mesh IEDs, medium energy peaks are observed at 197 and 260 eV respectively. These peaks are due to uncollided ions which originated from the sheath regions above the mesh corners. As the mesh height increases, the z component of the velocity of the ions reaching the collector from the sheath above the mesh corners becomes larger, shifting the medium energy peak to a higher energy. For the 1 cm mesh, ions from the sheath above the mesh corners are beyond the acceptance angle of the collector and are not measured. This is similar to the experimental results in figure 6.9 which show no medium energy peak for the 1 cm mesh and no mesh IEDs.

A graph of the mean ion density and mean ion flux, as a function of mesh height, for the IED results in figure 6.9 are shown in figure 6.11. As the mesh height increases, the mean ion flux increases. This is attributed to the increase in the

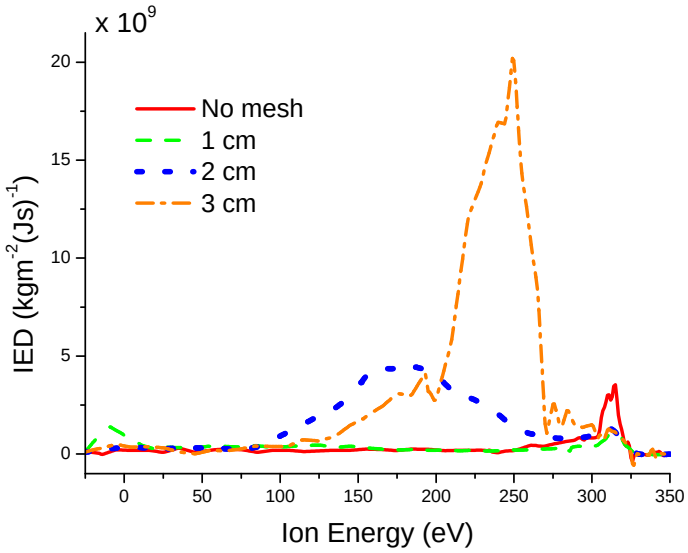

Figure 6.9: IEDs obtained 190 μs after the pulse switched on for various mesh heights with a -300 V pulse with a period of 800 μs and a pulse-on time of 200 μs. As the mesh height increases, the number of ions in the medium energy peak increases and the position of the medium peak shifts upward in energy due to the increase in the z component of velocity of these ions measured by the RFEA.

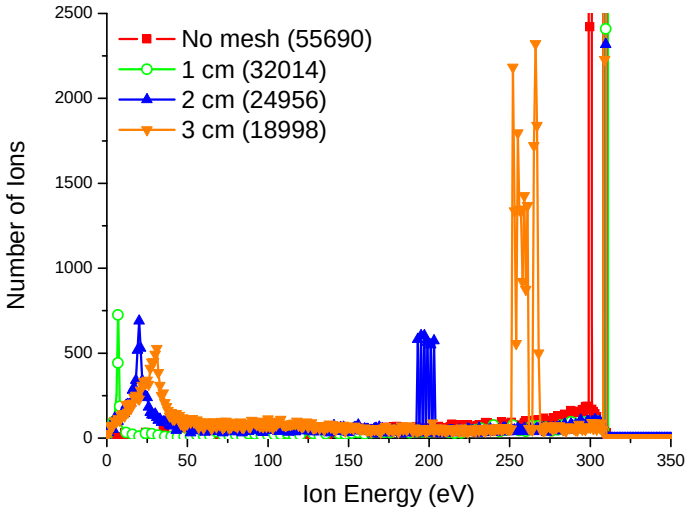

Figure 6.10: Simulation results showing the effects of mesh height on the IEDs obtained for a -300 V pulse at a pressure of 5 mTorr. The heights of the high energy peaks for each mesh height are shown in the legend.

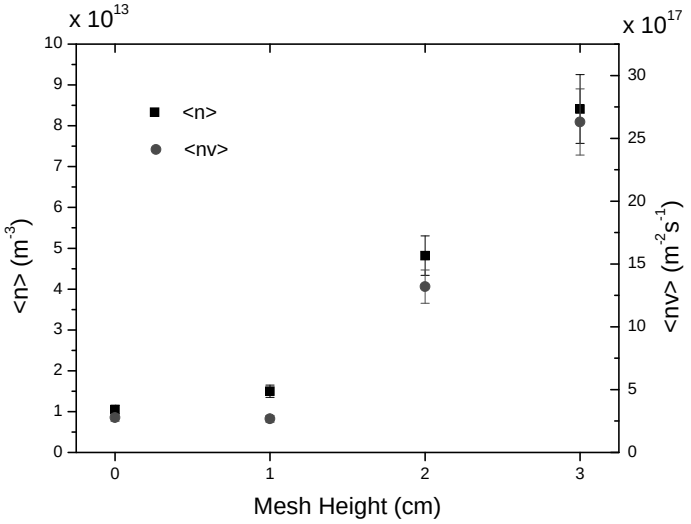

Figure 6.11: Mean ion densities and mean ion fluxes for the IEDs shown in figure 6.9 as a function of mesh height. Measurements were made 190 μs after the application of a -300 V pulse with a period of 800 μs and pulse-on time of 200 μs.

surface area of the plasma-sheath boundary. The increase in ion flux would result in an increased emission of secondary electrons which would increase ionisation and ion density. The slight decrease in ion flux between the no mesh and one centimetre high mesh results may be caused by the loss of ions to the mesh wires outweighing the increase in ion flux caused by the larger plasma-sheath surface area for this case. The measured ion densities are much lower than the density of 1x10^{15} m^{-3} used in the simulations. As discussed in chapter 5, this lower density may be due to the finite acceptance angle of the RFEA and due to ion losses inside the energy analyser. In the simulations, a lower ion density would result in a larger sheath thickness which would result in more ion collisions which would reduce the height of the high energy peak and result in a larger number of lower energy ions being measured.

6.4.4 Effects of Measurement Position

Simulations were used to study the IED at different positions on the RFEA front surface with a 2 cm high cylindrical mesh attached to the RFEA. The RFEA and mesh were biased at -300 V at a pressure of 5 mTorr. The different positions at

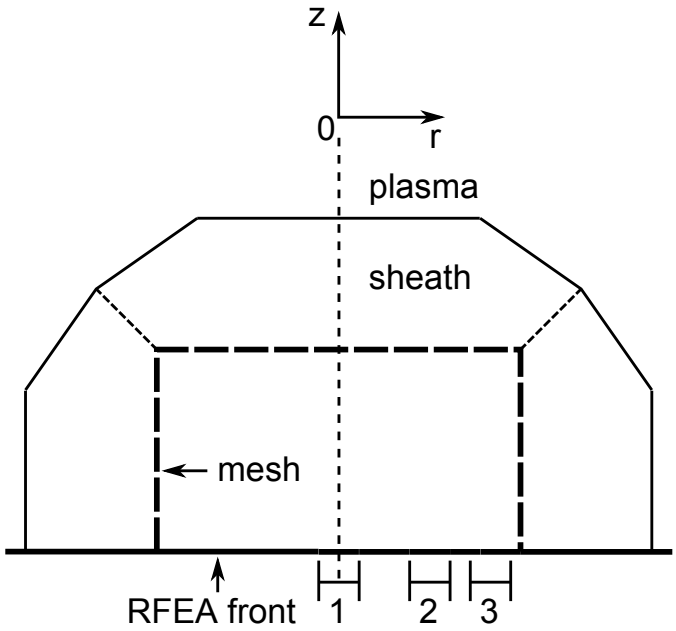

Figure 6.12: In the simulations in section 6.4.4, IEDs were determined using ions which struck the (1) centre (r=-2 to 2 mm), (2) middle (r=7 to 11 mm) and (3) edge (r=13.5 to 17.5 mm) positions on the RFEA front surface under a 2 cm high cylindrical mesh.

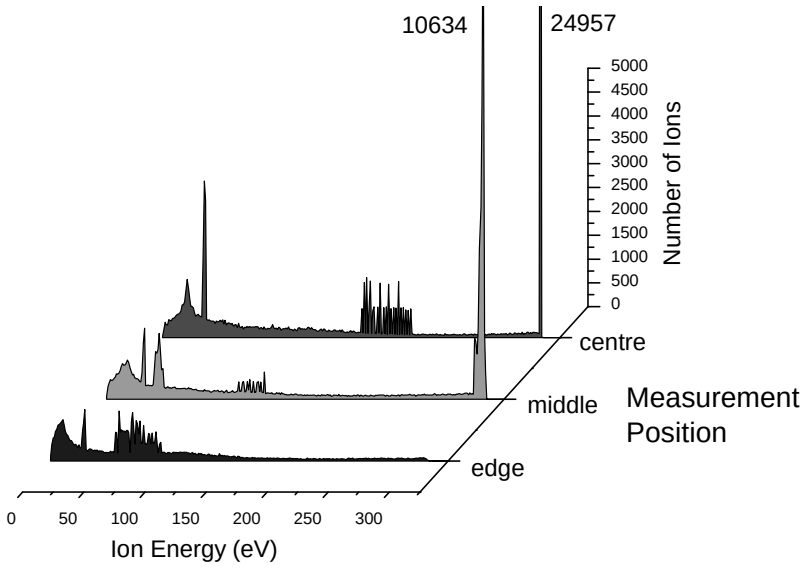

Figure 6.13: Simulation results showing the IEDs measured at the centre, middle and edge positions on the RFEA front surface in figure 6.12. The pulse amplitude was -300 V and the pressure was 5 mTorr. The high energy peak heights of the centre and middle position IEDs are also shown.

which the IEDs were measured are shown in figure 6.12. The IEDs shown in figure 6.13 were obtained using the energy associated with the z component of velocity of all ions which struck the centre (r=-2 to 2 mm), middle (r=7 to 11 mm) and edge (r=14 to 18 mm) sections. The centre position IED is very similar to the simulated IED in figure 6.5 which took into account ion losses to the side walls inside the RFEA. Medium energy peaks are measured at the edge, middle and centre position IEDs at 80, 125 and 200 eV respectively due to ions from the sheath edge above the mesh corners. The position of the medium energy peak is dependent on the z component of velocity of the ions and shifts to lower energies for positions closer to the mesh edge. Both the centre and middle position IEDs have high energy peaks close to 309 eV due to ions from the sheath above the mesh top. This peak is not observed in the edge position IED as above the mesh corner the sheath edge is not parallel to the mesh surface and no ions arrive with trajectories perpendicular to the RFEA front surface. For all IEDs, a low energy peak between 0 to 50 eV is measured due to ions which are trapped by the space charge potential hump formed inside the mesh region. The sharp peaks observed within the low energy peak are due to ions from the mesh sides. The short and sharp nature of these peaks are due to the finite spacing between the launch sites of ions at the sheath edge. A finer spacing between launch sites would help to smooth over these peaks but would also increase the time required for each simulation.

6.5 Summary

In this chapter, a RFEA was used for the first time to investigate the effects of a mesh during PIII of a metal surface. Both experiment and simulation results showed that the majority of ions originate from sheath sections above the mesh top and corners. The IEDs obtained at the base of the centre of a cylindrical mesh during PIII had a low, medium and high energy peak. Simulation shows that the high energy peak is caused by ions from the sheath directly above the RFEA inlet. The low energy peak is caused by ions which collide on the RFEA side of the potential hump formed inside the mesh. The medium energy peak is caused by ions from the sheath sections

above the mesh corners. As the mesh height increases, simulation results show that the z component of the velocity of the medium energy peak ions increases, which shifts the medium energy peak to a higher energy. As pulse amplitude and/or mesh height increases, the mean ion flux increases. This is attributed to the increase in the surface area of the plasma-sheath boundary.

Simulation results showed that the IED is dependent on position on the RFEA front surface. The high energy peak, caused by ions from the sheath above the mesh top, is not present in IEDs near the mesh cylinder. This is due to the curvature of the sheath edge around the mesh corner. The medium energy peak, produced by ions from the sheath above the mesh corner, shifts to lower energies for IEDs at positions closer to the mesh cylinder. This is caused by the decrease in the z component of velocity of ions measured from the sheath corners at positions closer to the mesh cylinder. Compared to the case with no mesh, the use of a mesh increases the ion flux to the surface and significantly modifies the IED shape.

Chapter 7

Ion Energy Measurements During PIII of an Insulator

7.1 Introduction

When an insulator is placed in a plasma and negatively biased with a conductive electrode it will accumulate a positive charge and its surface potential will increase. This affects the energy distribution of incoming ions and the extent of surface modifications. In this chapter, a RFEA is used for the first time to investigate the effects of insulator surface charging during PIII with and without a metal mesh present. IED measurements were made through an orifice cut into the centre of a piece of Mylar fixed to the RFEA front surface. A two dimensional numerical simulation was used to interpret these results. In section 7.2, the accumulation of charge on an insulator during PIII and its effects on the sheath shape, ion flux and energy are discussed. In section 7.3, the experimental setup used is given and in section 7.4 the simulation method used is discussed. In section 7.5, the results of experimental ion energy measurements made at the orifice cut into the insulator both with and without a mesh are presented and compared with simulation results.

7.2 Insulator Charging During PIII

PIII is increasingly being used in the treatment of insulator materials to improve surface properties such as wetability and adhesiveness. In PIII, when an electrically conductive object is pulse biased, the surface potential will equal the applied pulse amplitude. For an insulator, during negative biasing, the implantation of positive ions and the release of secondary electrons will result in surface charging. The charging of the insulator will continue until the insulator reaches the floating potential, given by equation (2.36), where the flux of ions and electrons to the surface is equal. The surface potential ($V(t)$) of an insulator is given by [44]

$$V(t) = V_0 - \Delta V(t) \tag{7.1}$$

where V_0 is the metal substrate potential and $\Delta V(t)$ is the potential drop across the insulator. If the insulator is approximated as a parallel plate capacitor of thickness d and cross sectional area A, the potential drop across the insulator is given by

$$\Delta V(t) = \frac{Q(t)}{C} = \frac{Q(t)d}{\epsilon_0 \epsilon_r A} \tag{7.2}$$

where C is the sample capacitance, $Q(t)$ is the surface charge and ϵ_r is the insulator dielectric constant. The surface charge is given by

$$Q(t) = \int_0^t j_i(t)\,(1+\gamma)\,dt \tag{7.3}$$

where γ is the secondary electron emission coefficient and $j_i(t)$ is the ion current density. The ion current density is equal to the Child law ion current density, given by equation (2.46), plus a displacement current term due to the electric field across the sheath. The displacement current (j_d) across the sheath is given by

$$j_d = \epsilon_0 \frac{\partial E}{\partial t} \tag{7.4}$$

where E is the electric field. If the sheath is considered to be a parallel plate capacitor with cross sectional area A, using Gauss's law, the electric field across the

sheath is given by

$$E = \frac{Q}{\epsilon_0 A} \tag{7.5}$$

where Q is the charge on the capacitor plates. For a sheath of thickness $s(t)$, with a potential V_0 across it, the capacitance (C) is given by

$$C = \frac{\epsilon_0 A}{s(t)} = \frac{Q}{V_0} \tag{7.6}$$

Substitution of (7.5) and (7.6) into (7.4) gives

$$j_d(t) = -\frac{V_0 \epsilon_0}{s^2(t)} \left(\frac{ds}{dt} \right) \tag{7.7}$$

Substitution of the expression for the sheath position given by equation (3.9) into (7.7) gives the displacement current

$$j_d(t) = -\frac{1}{9} u_0 e n_i \left(\frac{2}{3} \omega_{pi} t + 1 \right)^{-\frac{4}{3}} \tag{7.8}$$

where n_i is the ion density, u_0 is the ion velocity given by equation (3.4) and ω_{pi} is the ion plasma frequency given by equation (2.19). The total ion current density ($j_i(t)$) is given by the Child law current density in equation (2.46) plus the displacement current in equation (7.8) which gives

$$j_i(t) = \frac{4}{9} \epsilon_0 \left(\frac{2e}{M} \right)^{\frac{1}{2}} V_0^{\frac{3}{2}} \left(\frac{1}{s^2(t)} + \frac{s_0^2}{2s^4(t)} \right) \tag{7.9}$$

where s_0 is the matrix sheath thickness given by (2.40) and M is the ion mass.

The surface potential obtained using equations (7.1) to (7.9) for a Mylar disc, of thickness 70 μm, covering the RFEA front surface biased at -300 V is shown in figure 7.1 for several different secondary electron emission coefficient (γ) values. The potentials are shown only until the insulator reached the floating potential of -14 V or until a time of 200 μs. The floating potential was determined using equation (2.36) for argon ions and an electron temperature of 3 eV. The Mylar disc diameter

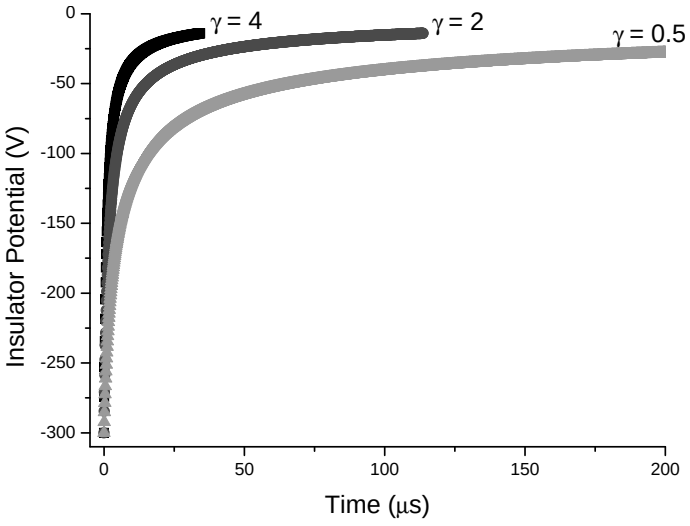

Figure 7.1: The insulator surface potential obtained using equations (7.1) to (7.9) for a 70 μm thick Mylar disc covering the RFEA front surface biased at -300 V for several different secondary electron emission coefficients (γ). The disc diameter was 36 mm with a circular section with a diameter of 4 mm removed from the centre.

was 36 mm with a circular section with a diameter of 4 mm removed from the centre to allow ions to enter the RFEA. The Mylar dielectric constant was taken to be 3.1 [40] and the ion density to be 1x10^{13} m^{-3}. The secondary electron emission coefficient of γ=4 was based on data for electron bombardment of Mylar [17]. For smaller secondary electron emission coefficients, the number of electrons released from each ion bombardment is reduced and the rate of increase in the insulator potential decreases.

To date, there have been limited experimental studies of the effects of surface charging on the IED during PIII of insulators. Experimental studies have shown the use of metal grids over the insulator can improve the depth of treatment [44] and that the thickness and dielectric properties of the insulator also affect the ion implantation depth [41]. Simulation studies at DC biased [62] and RF biased substrates [63] have shown that near an insulator/conductor interface the ion trajectories and energy distributions are significantly affected by sheath distortion. Due to charging of the insulator, the sheath thickness above the insulator is reduced which focuses more ions to the conductor and increases the spread of the IED.

In this chapter, the effects of the surface charging of an insulator during PIII are

investigated experimentally and using computer simulation. Direct measurement of the IED at the insulator surface is not possible and IED measurements were made through a metal mesh covered orifice in the centre of a Mylar insulator. To distinguish between the effects of the metal orifice and the effects of insulator surface charging on the IED, a two dimensional numerical simulation of ion trajectories in the plasma sheath and mesh regions was performed. The effects of placing a metal mesh cylinder over the Mylar were investigated and compared with simulation results.

7.3 Experimental Method

Ion energy and flux measurements during PIII were made by pulse biasing the RFEA with a Mylar sheet fixed to the front of the analyser. The experimental setup used was the same as shown in figure 5.1. Measurements were made in an argon capacitive 13.56 MHz RF plasma at a pressure of 5 mTorr. The Mylar sheet was cut to the same shape as the metal front of the RFEA, shown in figure 4.5, and was fixed to the RFEA front using the four M3 screws which attached the front lid to the main body of the RFEA. A four millimetre diameter hole was cut out of the centre of the Mylar above the RFEA inlet orifice to allow ions to enter the analyser. The Mylar thickness was $70 \pm 1\ \mu m$.

Measurements were made using a -300 V pulse both with and without a 2 cm high cylindrical mesh attached to the RFEA front. The mesh dimensions were the same as described in section 6.2. The pulse width was 200 μs and the pulse period was 800 μs.

7.4 Simulation Method

As the IED cannot be measured directly at the insulator surface using the RFEA, a two dimensional numerical simulation in cylindrical (r,z) coordinates was used to interpret experimental results and study the effects of insulator surface charging. The simulations were performed using GNU Octave. Using the same method dis-

cussed in section 6.3, the potentials in the mesh and sheath regions were determined by using the relaxation method to solve Poisson's equation, taking in to account the decrease in ion density as the ions accelerate. The effects of secondary electron emission were not included in the simulation.

For each simulation, the potential on the mesh and the RFEA inlet was set to the pulse amplitude of -300 V. The potential along the plasma-sheath edge was set to 0 V. To simulate the effects of surface charging, the insulator potential was set to a value between -300 V and the floating potential of -14 V. The floating potential was determined using equation (2.36) for argon ions and an electron temperature of 3 eV.

7.4.1 Sheath Edge and Ion Motion

For the simulations of an insulator with a mesh, the location of the sheath edge was determined using the method discussed in section 6.3.1. For the insulator with no mesh simulations, the location of the sheath edge, which was fixed at 0 V, was determined using a linear interpolation between the one dimensional Child law sheath thickness (h_1) above the RFEA inlet orifice and the Child law sheath thickness above the insulator (h_2) as shown in figure 7.2. The sheath thickness above the inlet orifice is determined by the potential of the metal front grid of the RFEA which remains at -300 V. The sheath thickness above the insulator is determined by the insulator potential which is dependent on the effects of surface charging. The linear interpolation between h_1 and h_2 was extended a distance w_1 above the insulator with w_1 set to 1 mm.

For the simulations of an insulator with no mesh, the potential array was solved from r=0 mm to r=36 mm. To impose boundary conditions on the potential array, the potential along the z-axis at r=36 mm was set to the one dimensional Child law sheath potential above the insulator and the potential array was assumed to be symmetrical about r=0 mm. The potential values in the sheath must be less than the potential at the plasma sheath edge. To ensure all values of potential in the sheath were less than the potential at the plasma sheath edge, the sheath thickness

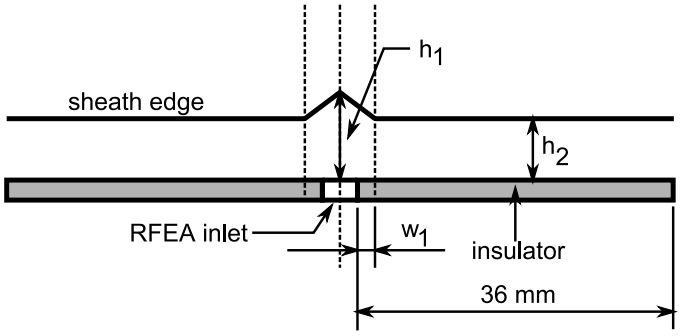

Figure 7.2: In the simulations with no mesh cylinder, the position of the sheath edge was determined by taking a linear interpolation between the sheath thickness above the RFEA inlet orifice (h_1) and the sheath thickness above the insulator (h_2). The linear interpolation between h_1 and h_2 was extended a distance w_1 over the insulator.

h_1 was reduced in height until the relaxation method solution gave all potential values less than zero.

For the simulations, ions were started at 0.05 mm intervals along the sheath edge as described in section 5.4.1. One thousand ions were launched from each start point at the Bohm velocity with trajectories perpendicular to the sheath edge. Ions were released individually into the potential array and their position determined at 0.002 μs intervals using the electric field at each position. Collisions between ions and neutral gas molecules were modelled using the Monte Carlo approach described in section 5.4.2. Ions with trajectories which reached the RFEA collector were used to construct the simulated IEDs.

7.5 Results and Discussion

7.5.1 Insulator With No Mesh

A piece of Mylar was attached to the RFEA front surface and ion energy measurements were made with the RFEA pulse biased in an argon plasma with a RF power of 150 W and a pressure of 5 mTorr. The pulse amplitude was -300 V with a pulse-on time of 200 μs and a pulse period of 800 μs. A graph of the IEDs obtained at different times during the pulse-on period are shown in figure 7.3 along with an

IED obtained with no Mylar present, 30 μs after the pulse switched on. With no insulator, a high energy peak is observed at 313 eV along with ions with a range of energies between zero and the maximum ion energy of 325 eV. With an insulator, in the early stages of the pulse, a high energy peak is also observed at 313 eV but during the pulse this peak height decreases and a medium energy peak between 100 and 300 eV increases in height.

For the IED with an insulator present, the maximum energy measured was 325 eV which represents ions which gained the maximum sheath potential of the pulse amplitude plus the time averaged plasma potential. A high energy peak is observed at 313 eV which indicates a large number of ions gain close to the maximum energy. These ions experience very few collisions and arrive at the RFEA with trajectories close to perpendicular to the RFEA front surface.

The spread of ion energies measured between zero and the maximum ion energy has several possible causes. After the pulse is switched on, the formation of a matrix sheath results in the measurement of ions with a range of energies between zero and the full sheath potential depending on the ion's initial position in the sheath. This would be most significant for the earliest measurements taken after the pulse was switched on. At later times during the pulse, the spread of ion energies is caused by the measurement of ions which collide in the sheath and by the measurement of ions with trajectories not perpendicular to the RFEA front surface. As discussed in section 4.5.1, ion collisions may be hard sphere momentum transfer collisions or charge exchange collisions which at a pressure of 5 mTorr have mean free paths of approximately 36 and 12 mm respectively. The RFEA discriminates ions based on the component of their velocity perpendicular to the RFEA front surface and ions arriving at the RFEA front surface at an angle not equal to ninety degrees will be measured as having a lower energy.

A graph of the mean ion densities and mean ion fluxes for the IEDs in figure 7.3 are shown in figure 7.4 as a function of time after the pulse was switched on. Both the mean ion density and mean ion flux increase during the pulse-on period. This is attributed to the increase in the curvature of the plasma-sheath edge over the RFEA inlet/insulator interface region as the insulator potential increases. As the insulator

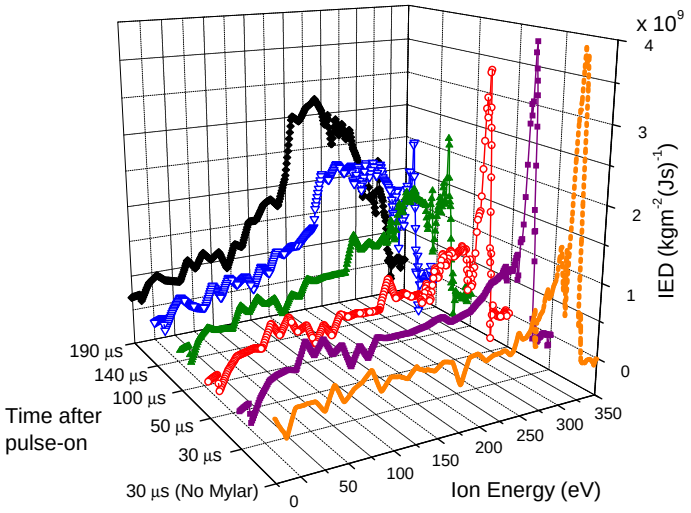

Figure 7.3: IEDs obtained at different times during the application of a -300 V pulse to the RFEA with a piece of Mylar around the RFEA inlet orifice. An IED obtained 30 μs after the pulse switched on with no Mylar present is shown for comparison. The pulse-on time was 200 μs and the pulse period was 800 μs. During the pulse, the height of the high energy peak at 313 eV decreases and the height of the medium energy peak between 100 to 300 eV increases.

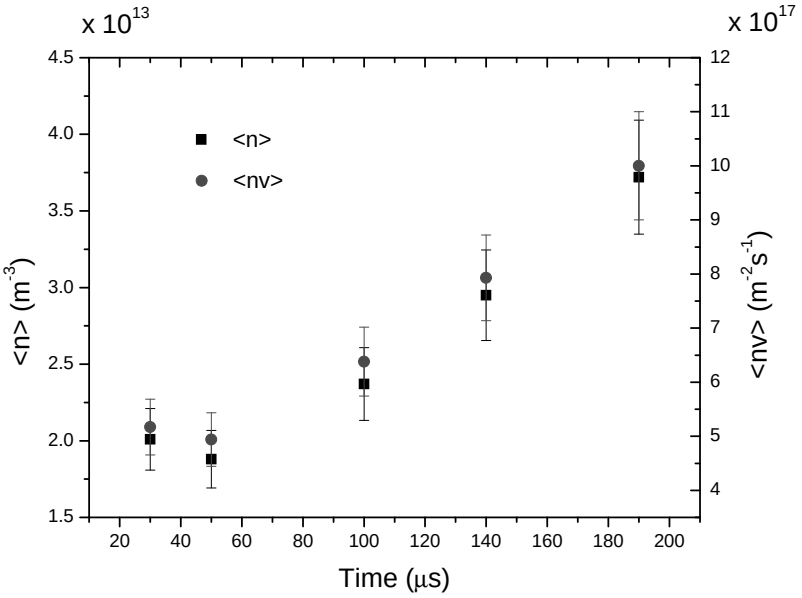

Figure 7.4: The mean ion densities $\langle n \rangle$ and mean ion fluxes $\langle nv \rangle$ for the IEDs in figure 7.3 as a function of time after the application of a -300 V pulse to the RFEA with a piece of Mylar around the RFEA inlet.

potential increases, the sheath thickness above the insulator decreases which causes the sheath edge to curve over the RFEA inlet/insulator interface region. This directs more ions into the RFEA inlet orifice which increases the ion flux and the measured ion density as the insulator potential increases. For the ion densities measured at the start of the pulse which were of the order of $1x10^{13}$ m^{-3}, the Child law sheath thickness is approximately 10.2 cm for an electron temperature of 3 eV and pulse amplitude of -300 V. This is larger than the mean free paths for hard sphere and charge exchange collisions at 5 mTorr which are approximately 36 mm and 12 mm respectively. In figure 7.3, the IEDs obtained in the early stages of the pulse show that the majority of ions experience very few collisions in the sheath. This result indicates that the ion densities measured using the IEDs may be lower than the actual plasma density. As discussed in chapter 5, this may be due to ion losses in the RFEA or due to the finite acceptance angle of the RFEA inlet orifice.

To assess the expected effects of surface charging during pulsing, simulations were carried out with different potentials on an insulator around the RFEA inlet orifice. The RFEA potential was -300 V and the pressure was 5 mTorr. In figure 7.5, the calculated potentials in the sheath are shown for the case where the potential on the insulator was set to -50 V and the potential on the RFEA inlet mesh was -300 V. Figure 7.6 shows the simulation results for the effects on the IED of different potentials on the insulator. The maximum insulator potential tested was -14 V which is the floating potential for an argon plasma with an electron temperature of 3 eV. The simulation IEDs show similar trends to the experimental IEDs. A high energy peak is observed at 301 eV which is close to the maximum energy measured of 305 eV. This peak is due to ions originating from the sheath edge directly above the RFEA inlet. The maximum ion energy is larger than the maximum sheath potential of the pulse amplitude plus the energy associated with ions entering the sheath at the Bohm velocity due to the finite time step size used in the simulations. Smaller time steps can reduce this error but significantly increase the time required for each simulation. As the potential on the insulator becomes more positive, the height of the high energy peak decreases and more ions with energies between 150 and 300 eV are measured. This is caused by the increase in insulator potential which increases

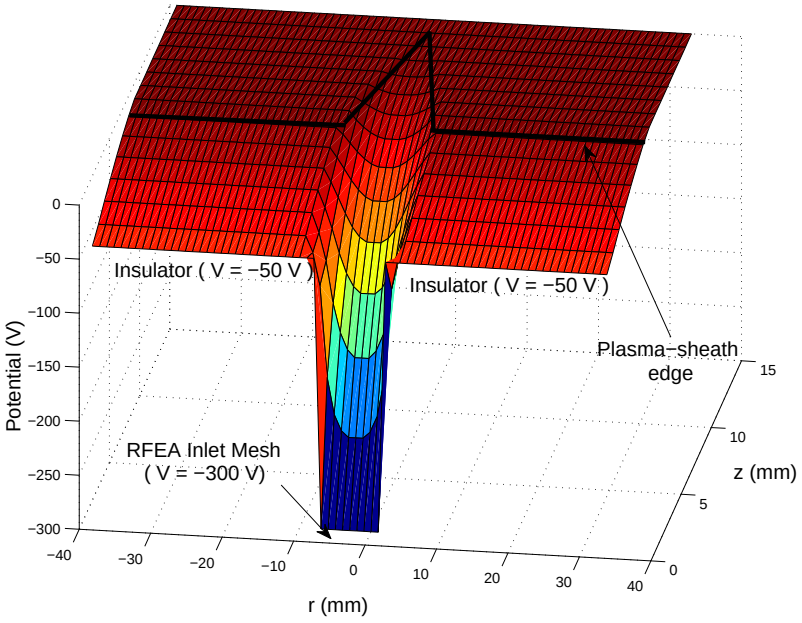

Figure 7.5: Calculated potentials in the sheath for the case where the potential on the insulator was set to -50 V and the potential of the RFEA inlet mesh was set to -300 V. The plasma-sheath edge is shown by the black line.

the curvature of the sheath over the metal RFEA inlet/insulator interface region as shown in figure 7.5. The increase in sheath curvature in this region focuses more ions which previously travelled to the insulator toward the RFEA inlet at angles less than ninety degrees to the RFEA front surface. The increase in the sheath curvature also causes more ions from the plasma-sheath edge directly above the RFEA inlet to arrive at the RFEA with trajectories which are not perpendicular to the RFEA front surface. Ions which arrive at the RFEA with trajectories not perpendicular to the RFEA front surface will be measured as having lower energy as the RFEA discriminates ions based only on the z component of their velocity. The increase in sheath curvature is seen in the IEDs as a decrease in the number of ions in the high energy peak and an increase in the number of lower energy ions measured as the insulator potential increases which is a similar trend to the experimental IEDs in figure 7.3 and to simulation results obtained by others [62, 63].

Comparison of the experimental and simulated IEDs in figures 7.3 and 7.6 allow some estimates of the insulator surface potential to be made. After the pulse has been on for 100 μs the increase in the number of ions between 175 and 300 eV in the

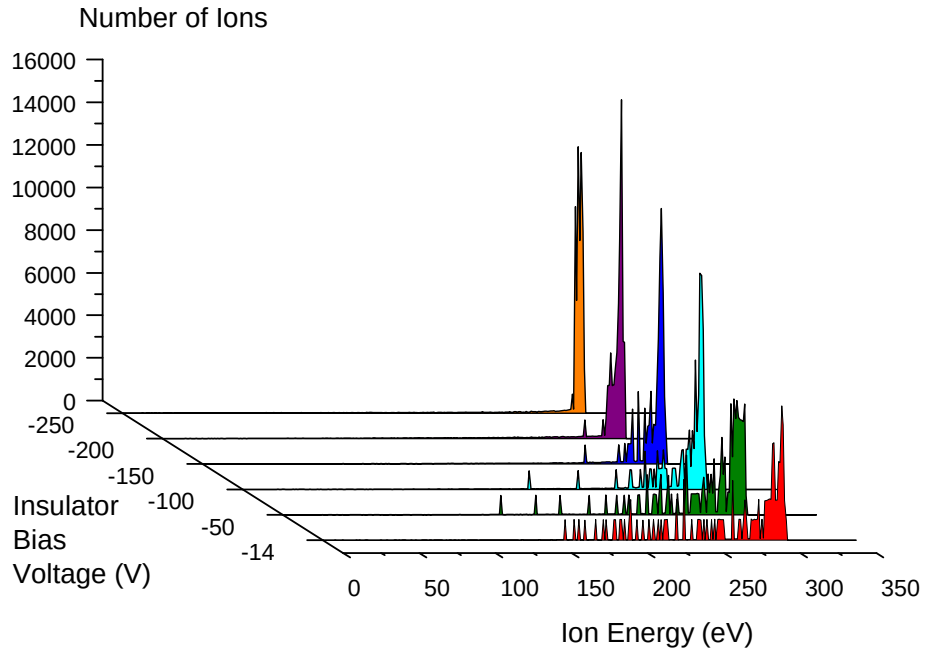

Figure 7.6: Simulation results at a pressure of 5 mTorr for different potentials on an insulator fixed around the RFEA inlet. The RFEA front surface potential was -300 V. As the insulator potential increases, the spread of the IED to lower energies increases due to the increase in the curvature of the sheath over the metal-insulator region.

experimental IED most closely matches simulated IEDs with insulator potentials of -150 or -100 V. After a pulse-on time of 140 μs, the experimental IEDs most closely match the simulation results obtained with insulator potentials of -50 and -14 V indicating that the insulator is close to the floating potential. From these results it appears that the Mylar is approaching the floating potential after approximately 100 to 150 μs. Using the insulator potential graphs in figure 7.1, these results indicate that the Mylar secondary electron emission cofficient (γ) may be somewhere close to two. Further simulations at different insulator potentials would be necessary to more accurately determine the insulator potential during pulsing.

7.5.2 Effects of Measurement Position with Insulator and No Mesh

As the IED cannot be measured directly at the insulator surface using the RFEA, simulations were used to study the IED at different positions on the insulator. To

simulate the effects of insulator surface charging, simulations were performed with the insulator potential set at different values. As shown in figure 7.7, the IEDs were determined using ions which struck the RFEA metal mesh inlet (r=-2 to 2 mm), the insulator surface next to the RFEA inlet (r=2.5 to 6.5 mm) and a section of insulator further away from the RFEA inlet (r=6.5 to 10.5 mm). Simulations were carried out at a pressure of 5 mTorr and with a potential of -300 V applied to the RFEA. The IEDs were constructed using the energy associated with the z component of velocity of ions which struck the surface. Graphs of the IEDs obtained at the three different locations are shown in figures 7.8, 7.9 and 7.10.

The IEDs obtained using ions which impacted on the RFEA metal inlet are very similar to those shown in figure 7.6 which were measured 3.5 mm below the inlet at the RFEA collector. A high energy peak is measured at 301 eV. As the insulator potential increases, the height of this peak decreases and more ions with energies between 25 and 300 eV are measured. This is due to increase in the curvature of the sheath over the metal-insulator interface region which results in more ions being directed to the RFEA inlet at angles less than ninety degrees to the RFEA front surface as the insulator potential increases.

For ions arriving at the insulator surface, the maximum ion energy is determined by the insulator potential. For the IEDs at the insulator surface, high energy peaks are measured close to the energy associated with the insulator potential along with a number of ions with energies between zero and the maximum sheath potential energy. The spread of ions with energies between zero and the maximum ion energy is caused by ion collisions in the sheath and the measurement of ions with trajectories not perpendicular to the RFEA front surface. Compared to the insulator further away from the RFEA inlet, at the insulator next to the RFEA inlet the height of the high energy peak is lower and as the insulator potential increases, more ions are measured with energies within 50 eV of the high energy peak. This is caused by the curvature of the sheath over the metal-insulator interface region which increases as the insulator potential becomes larger. This results in more ions being directed toward the RFEA metal inlet and in a larger number of ions arriving at the insulator next to the inlet at angles less than ninety degrees to the RFEA front surface. At

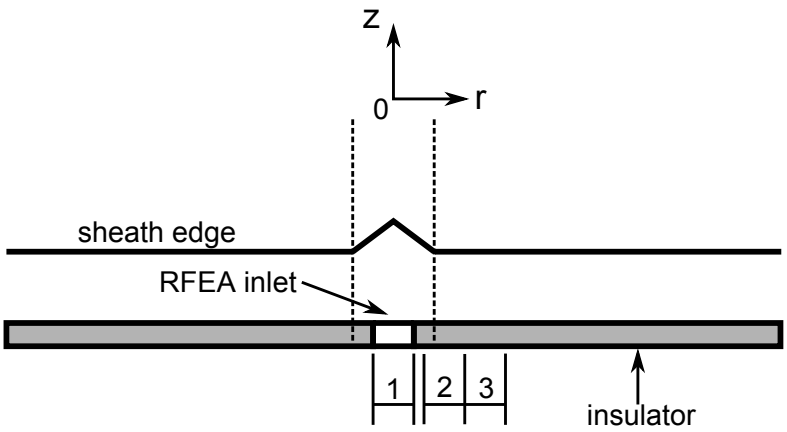

Figure 7.7: In the computer simulations in section 7.5.2, IEDs were determined using ions which struck (1) the RFEA metal mesh inlet (r=-2 to 2 mm), (2) the insulator surface next to the RFEA inlet (r=2.5 to 6.5 mm) and (3) a section of insulator further away from the RFEA inlet (r=6.5 to 10.5 mm).

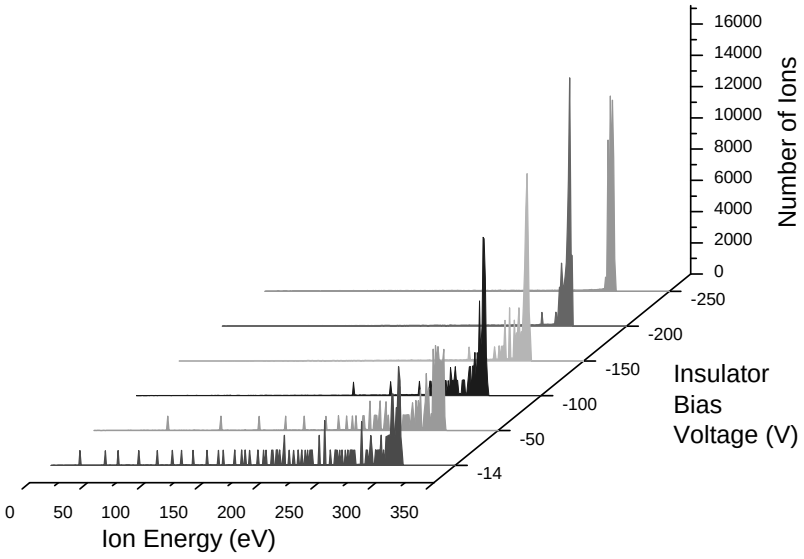

Figure 7.8: Simulated IEDs measured at the RFEA metal mesh inlet (r=-2 to 2 mm) as a function of potential on the insulator surface. As the insulator potential increases, the curvature of the sheath over the metal/insulator interface results in the measurement of more ions with less than the full sheath potential energy.

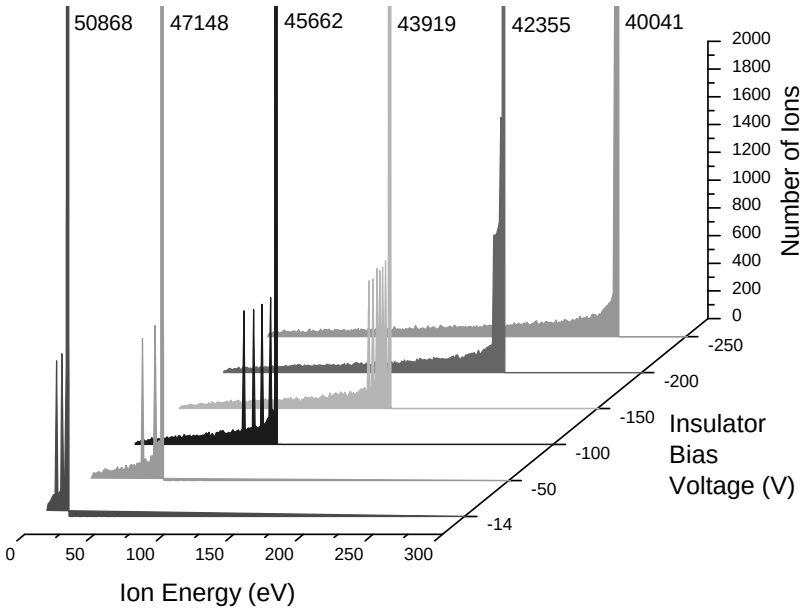

Figure 7.9: Simulated IEDs and corresponding peak heights measured at the insulator next to the RFEA inlet (r=2.5 to 6.5 mm) as a function of potential on the surface of the insulator. As the insulator potential increases, the curvature of the sheath over the metal/insulator interface reduces the number of ions reaching this section of insulator and reduces the measured energy of incoming ions.

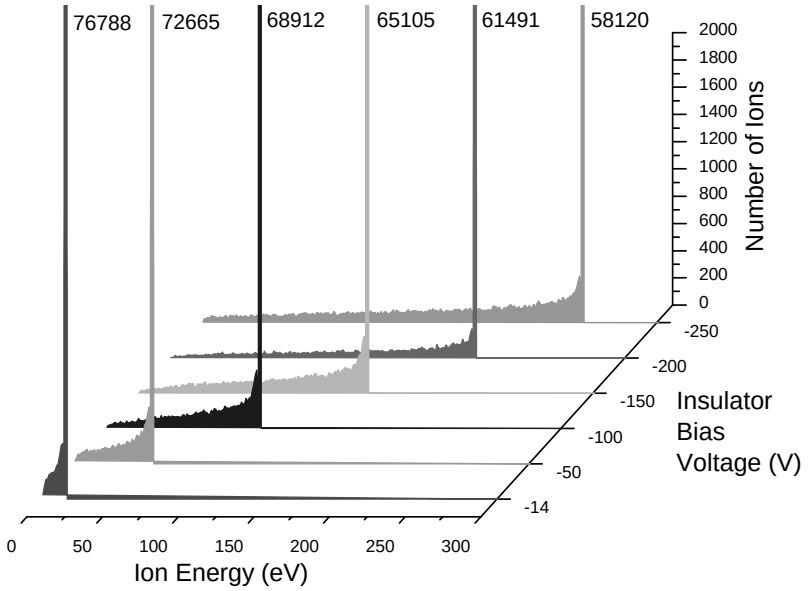

Figure 7.10: Simulated IEDs and corresponding peak heights measured at the insulator (r=6.5 to 10.5 mm) as a function of potential on the surface of the insulator. The majority of ions are measured with energies close to the insulator potential.

the insulator section further away from the RFEA inlet, as the insulator potential increases, the sheath edge remains parallel to the insulator surface and the majority of ions arrive with energies close to the insulator potential.

7.5.3 Insulator With Mesh

Ion energy measurements were made with a piece of Mylar and a 2 cm high cylindrical mesh fixed to the RFEA front surface in the same manner as shown in figure 6.1. Measurements were made with the RFEA pulse biased in an argon RF plasma with a RF power of 100 W and a pressure of 5 mTorr. The pulse amplitude was -300 V with a pulse-on time of 200 μs and a pulse period of 800 μs. A graph of the IEDs obtained at different times during the pulse-on period are shown in figure 7.11 along with an IED obtained with only the 2 cm high mesh cylinder and no Mylar present, 30 μs after the pulse switched on. For the IED with a mesh and no Mylar, a high energy peak is observed at 312 eV along with a medium energy peak at approximately 186 eV and a low energy peak near 25 eV. With a mesh and Mylar, in the early stages of the pulse, a high energy peak is observed at 314 eV along with a large low energy peak at 75 eV. During the pulse, the high energy peak height decreases and the low energy peak appears to move upward in energy to 150 eV and decrease in height.

As shown in figure 6.4, for the IED with the mesh cylinder and no Mylar, the high energy peak at 312 eV is formed by ions originating from the sheath above the mesh top. The wide medium energy peak at approximately 186 eV is formed by ions originating from the sheath above the mesh corners and the low energy peak near 25 eV is formed by ions which are trapped on the RFEA side of the space charge potential hump which forms inside the mesh region. Compared to the case with no Mylar, for the IED with the mesh cylinder and Mylar present, obtained 30 μs after the pulse switched on, the high energy peak at 314 eV is smaller, there is no medium energy peak and there is a much larger lower energy peak at 75 eV. These differences indicate that insulator surface charging has a significant effect on the IEDs measured by the RFEA.

For the IEDs with an insulator and mesh cylinder, the maximum ion energy measured was 324 eV which represents ions which gained the maximum sheath potential of the pulse amplitude plus the time averaged plasma potential. The small high energy peak observed at 314 eV indicates that very few ions arrive at the RFEA collector with close to the full sheath potential energy and that many ions are colliding and/or reaching the RFEA with trajectories not perpendicular to the RFEA front surface. The change in the shape of the IED during the pulse indicates that the surface charging of the insulator is having a significant effect on the trajectories of ions which are being measured by the RFEA.

Figure 7.12 shows the mean ion densities and ion fluxes for the IEDs in figure 7.11 as a function of time after application of the pulse. Compared to the case with no mesh, the total ion flux during the pulse is larger. The ion flux at the start of the pulse is also larger than the case with no mesh. This is attributed to the larger plasma-sheath surface area produced by the mesh which draws in more plasma ions. The decrease in the ion flux and density measured by the RFEA during the pulse are explained by the change in the potential inside the mesh region as the insulator surface potential increases. This results in less ions from the sheaths above the mesh top, sides and corners reaching the RFEA collector which decreases both the ion flux and density measured by the RFEA.

To investigate the effects of insulator surface charging, simulations were performed with different potentials on the insulator attached to the front of the RFEA with a 2 cm high cylindrical mesh attached. The IEDs obtained at different insulator potentials are shown in figure 7.13 and in figure 7.14 an enlarged view of figure 7.13 is given showing the origins of the ions in the simulations. The potential of the RFEA and 2cm high mesh was -300 V. The simulation IEDs show similar trends to those observed in the experimental IEDs. A high energy peak is observed at 302 eV which decreases in height as the insulator potential increases. As shown in figure 7.14, these ions originate from the sheath above the mesh top. As the potential of the insulator increases, more of these ions arrive at the RFEA collector with trajectories not perpendicular to the RFEA front surface and are measured as having lower energy. While the heights of the simulation peaks may not be correct due to

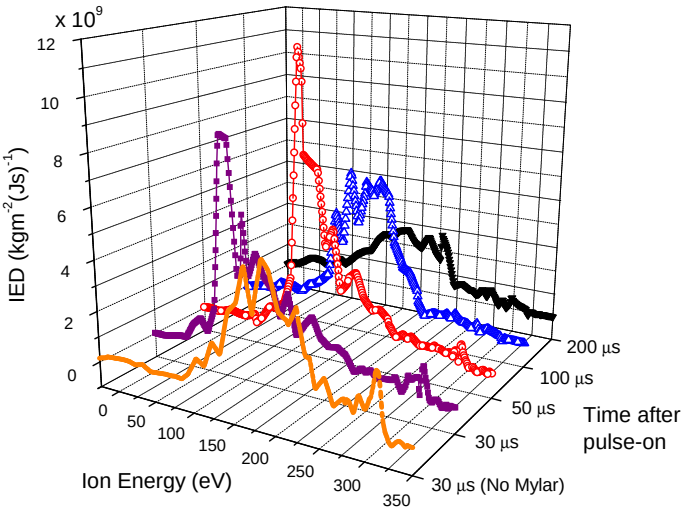

Figure 7.11: IEDs obtained at different times during the application of a -300 V pulse to the RFEA and a 2 cm high cylindrical mesh with a piece of Mylar attached to the RFEA front surface. An IED obtained 30 μs after the pulse switched on with no Mylar is shown for comparison. The pulse-on time was 200 μs and the pulse period was 800 μs. During the pulse, a low energy peak at 75 eV moves upward in energy to 150 eV and decreases in height.

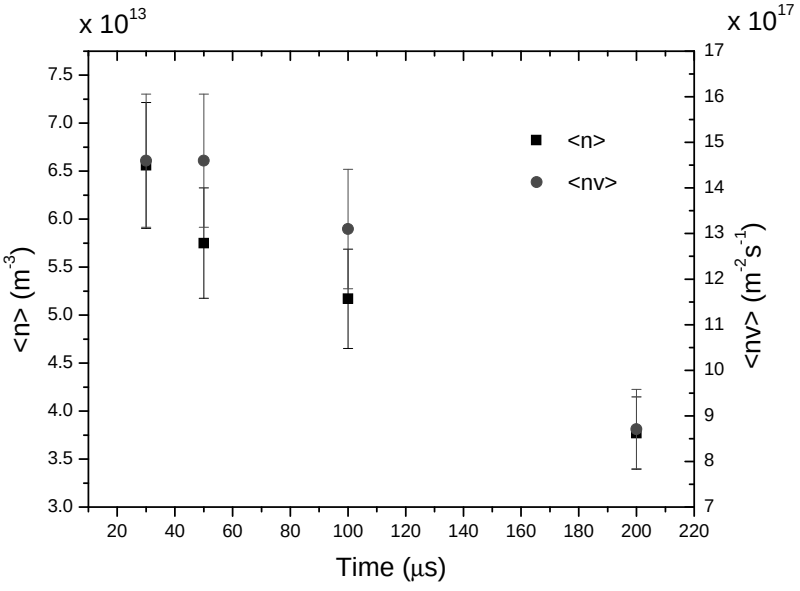

Figure 7.12: Mean ion densities $\langle n \rangle$ and mean ion fluxes $\langle nv \rangle$ from the IEDs in figure 7.11 as a function of time after application of a -300 V pulse to the RFEA with a Mylar insulator and 2 cm high cylindrical mesh fixed to the front surface of the RFEA.

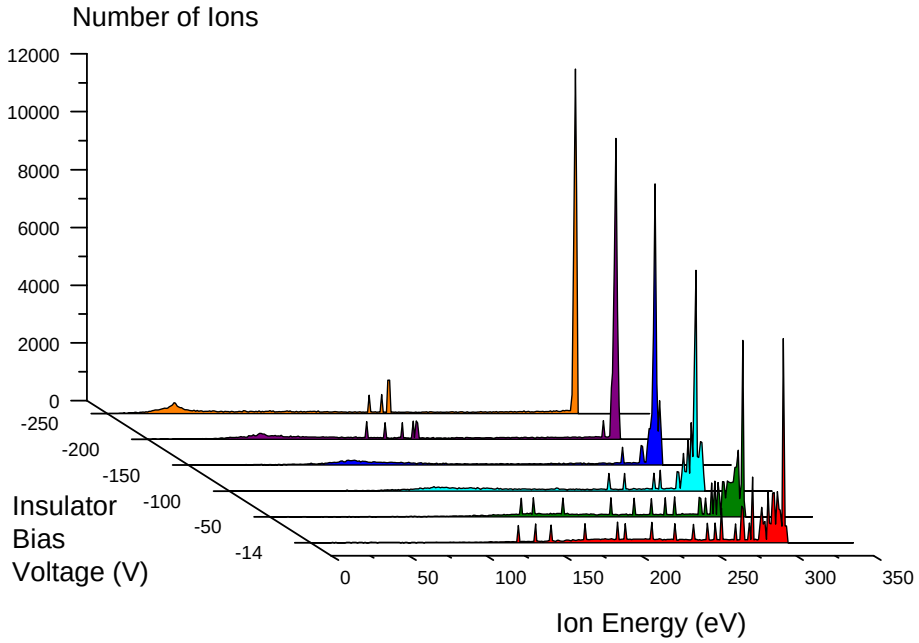

Figure 7.13: Simulation results for different potentials on an insulator fixed around the RFEA inlet orifice with a 2 cm high cylindrical mesh attached to the RFEA front surface at a pressure of 5 mTorr. The RFEA inlet orifice and mesh potential were -300 V.

the assumption that all ions enter the sheath at the Bohm velocity, the decrease in the high energy peak height with increasing insulator potential matches the experimental results in figure 7.11. The broad IED which results with increasing insulator potential also explains the wide medium energy peak which forms in the experimental results 200 μs after the pulse switched on. The isolated peaks, between 150 and 300 eV, in the -14 V and -50 V insulator bias IEDs in figure 7.14 are caused by the finite spacing between the ion starting positions on the sheath edge. A smaller spacing between starting locations would produce a smoother IED but also increase the time required for each simulation.

In figure 7.13, a medium energy peak is observed for insulator potentials of -250 V and -200 V at approximately 180 eV and 160 eV respectively. As shown in figure 7.14, this peak is caused by ions originating from the sheath above the mesh corners. For these ions, as the potential of the insulator increases, the component of velocity perpendicular to the RFEA front surface decreases as does the number of these ions reaching the RFEA collector. This decrease in peak height explains the decrease in

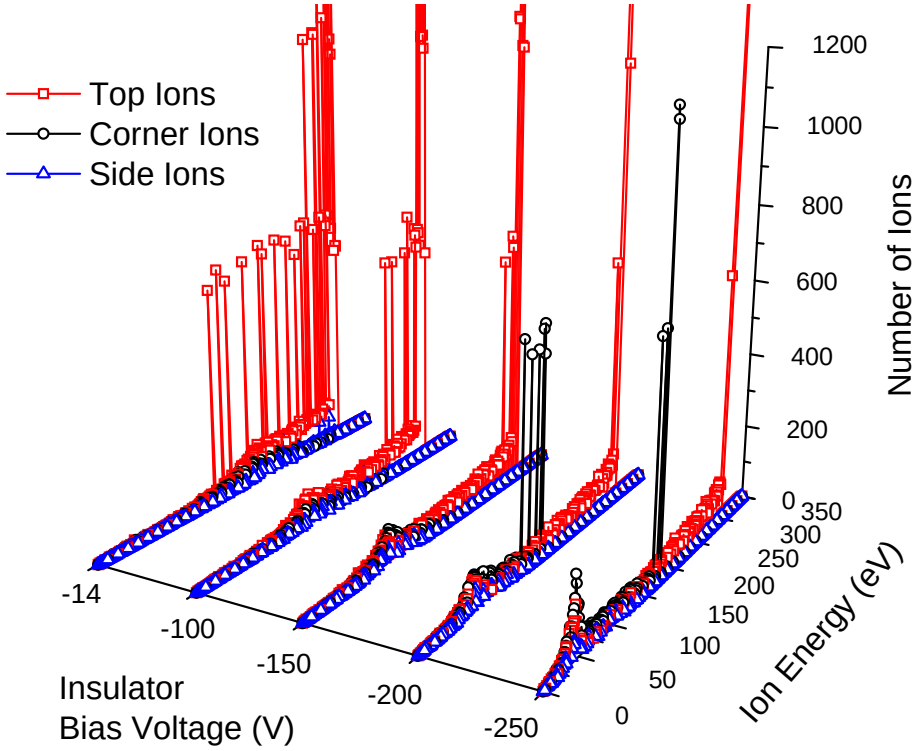

Figure 7.14: An enlarged view of the origins of the ions in the simulation results in figure 7.13. As the insulator potential increases, ions from the sheath above the mesh top are spread to lower energies and ions originating from the sheath above the mesh corners no longer reach the RFEA collector.

height of the medium energy peak in the experimental results in figure 7.11.

In figure 7.14, a low energy peak is observed for insulator potentials of -250 V, -200 V and -150 V at approximately 43 eV, 72 eV and 104 eV respectively. This peak is caused by a combination of ions originating from the sheaths above the mesh sides, corners and top which collide inside the sheath and/or mesh but still have trajectories which allow them to reach the RFEA collector. As the insulator potential increases, the position of the low energy peak also increases which explains the upward shift of the medium energy peak in the experimental results in figure 7.11.

Comparison of the experimental and simulation results in figures 7.11 and 7.14 allow some estimates of the insulator surface potential to be made. After the pulse has been on for 50 μs, the upward shift in energy of the medium energy peak toward 125 eV most closely matches the trends observed for the low and medium energy

peaks in the simulated IEDs if the insulator potential is assumed to be -200 or -150 V. After a pulse-on time of 100 μs, the broad spread of the medium energy peak at 150 eV most closely matches the simulation results with insulator potentials of -50 and -14 V, indicating that the insulator is now much closer to the floating potential as a result of surface charging. Further simulations at different insulator potentials would be necessary to more accurately determine the insulator potential during pulsing.

7.5.4 Effects of Measurement Position with Insulator and Mesh

As it is not possible to measure the IED at the insulator surface, simulations were used to study the IED at different positions on the insulator. As shown in figure 7.15, IEDs were determined using the z component of velocity of ions which struck the insulator next to the RFEA metal mesh inlet (r=2.5 to 6.5 mm), in the middle section of the RFEA front surface (r=7 to 11 mm) and next to the metal mesh cylinder edge (r=13.5 to 17.5 mm). Simulations were performed at a pressure of 5 mTorr and with a potential of -300 V applied to the RFEA and 2 cm high mesh cylinder. Graphs of the IEDs obtained are shown in figures 7.16, 7.17 and 7.18.

The maximum energy of ions arriving at the insulator is determined by the insulator potential. The IEDs obtained at the insulator next to the RFEA inlet and in the middle of the RFEA front surface have high energy peaks close to the energy associated with the insulator potential and a number of ions with energies between zero and the maximum sheath potential energy. The ions in the high energy peak originate from the sheath edge above the mesh top. The spread of ions measured with energies between zero and the maximum sheath potential energy are produced by ions which have undergone collisions and/or have arrived at the insulator with trajectories not perpendicular to the RFEA front surface. At the insulator next to the RFEA metal inlet, a larger number of ions with less than the energy associated with the insulator potential are measured. This is caused by the lower potential of the RFEA metal inlet which distorts ion trajectories and results in the measurement

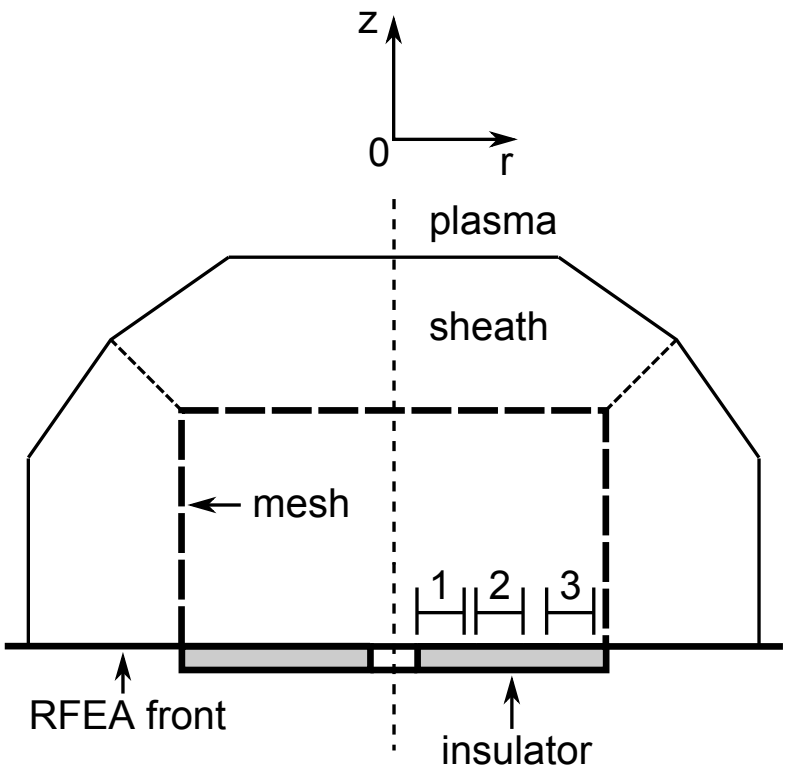

Figure 7.15: In the computer simulations in section 7.5.4, IEDs were determined using ions which struck the insulator (1) next to the RFEA metal mesh inlet (r=2.5 to 6.5 mm), (2) in the middle of the RFEA front surface (r=7 to 11 mm) and (3) next to the mesh cylinder edge (r=13.5 to 17.5 mm).

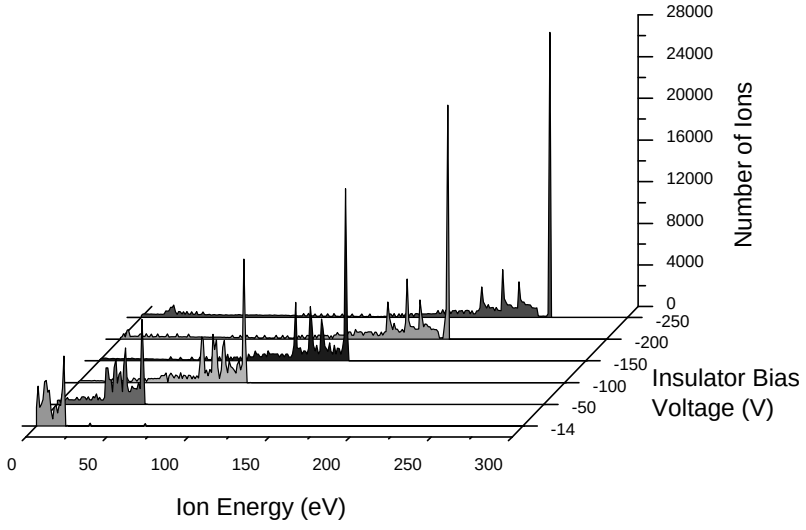

Figure 7.16: Simulated IEDs measured at the insulator next to the RFEA metal mesh inlet (r=2.5 to 6.5 mm) as a function of potential on the surface of the insulator. Ions originating from the sheath above the mesh corner are measured with energies less than the insulator potential.

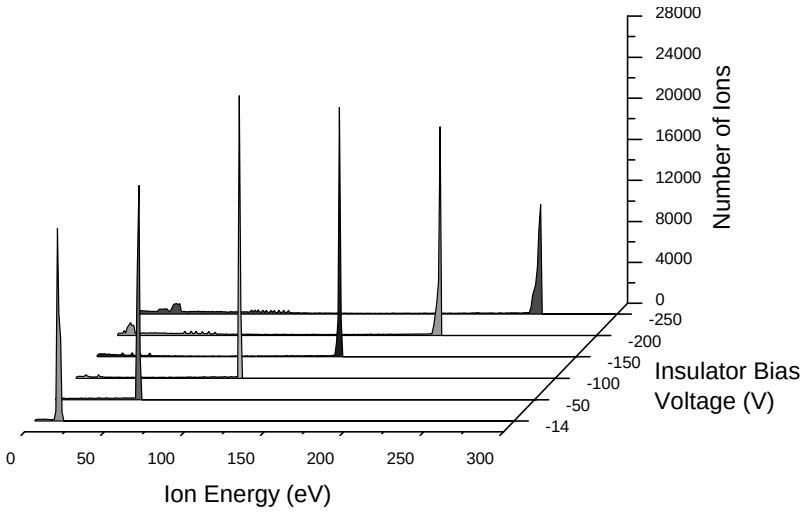

Figure 7.17: Simulated IEDs measured at the insulator in the middle of the RFEA front surface (r=7 to 11 mm) as a function of potential on the surface of the insulator. The maximum energy of ions is determined by the insulator potential.

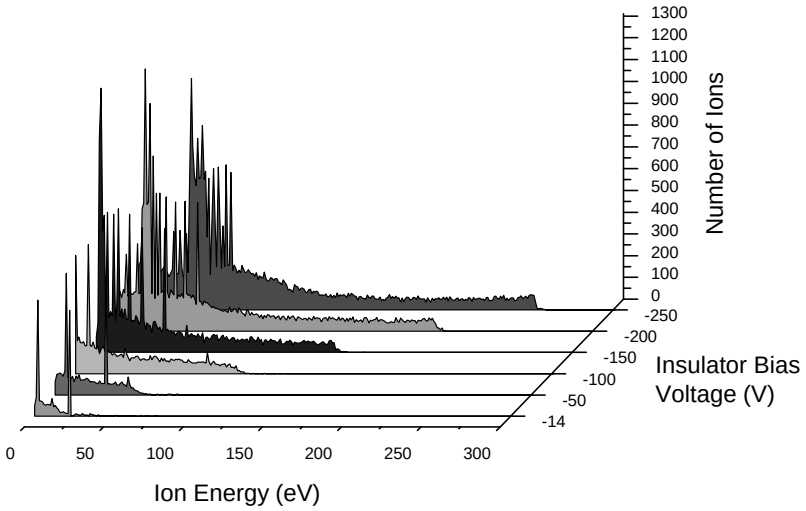

Figure 7.18: Simulated IEDs measured at the insulator next to the metal mesh cylinder (r=13.5 to 17.5 mm) as a function of potential on the surface of the insulator. The curvature of the sheath around the mesh corner results in less ions being measured with energy close to the insulator potential.

of a larger number of ions from the sheath edge above the mesh corners. These ions arrive at the insulator with trajectories not normal to the surface and are measured with energies less than associated with the insulator potential.

At the insulator next to the mesh cylinder, less ions are measured and no peak is observed close to the energy associated with the insulator potential. This is due to the curvature of the sheath around the mesh corner which results in less ions from the sheath above the mesh top reaching the insulator. Ions which reach the insulator surface arrive at angles not perpendicular to the surface and are measured with a spread of energies from zero up to the insulator potential.

7.6 Summary

In this chapter, the effects of the surface charging of a Mylar insulator during PIII were investigated with and without a metal mesh cylinder present. Qualitative agreement was found between experimental and simulation results. With no mesh, the number of lower energy ions measured by the RFEA through the orifice in the Mylar increased during the pulse-on time. Simulation results suggest that this is caused by the increase in the curvature of the sheath over the orifice region as the insulator potential increases as a result of surface charging. With increasing insulator potential, ions which previously travelled to the insulator are directed towards the RFEA collector with trajectories less than ninety degrees to the RFEA front surface. Simulations of IEDs at the insulator surface away from the orifice, show that the insulator potential determines the maximum energy of ions in the energy distribution.

Compared to the case with no mesh, the use of a mesh increased the ion flux during the early stages of the pulse but did not eliminate surface charging. During the pulse-on time, compared to the no mesh case, a larger number of lower energy ions were measured. Simulation results suggest that this is caused by the potential in the mesh region which affects the trajectories of ions from the sheath edges above the mesh top and corners and results in more ions being measured with trajectories not perpendicular to the RFEA front surface. Simulations suggested

that the IED at the insulator surface is dependent on position under the mesh and the insulator potential. The maximum energy of ions measured at the insulator surface is determined by the insulator potential. A high energy peak, produced by ions from the sheath edge above the mesh cylinder is not observed in IEDs at positions close to the mesh cylinder. This is due to the curvature of the sheath around the mesh corner. At positions on the insulator near the centre of the base of the mesh, peaks in the IED are observed close to the energy associated with the insulator potential. The use of a mesh during PIII of an insulator increases the total ion flux to the surface and significantly affects the IED structure.

Chapter 8

Conclusion

This chapter summarises the important findings of this thesis in relation to PIII.

At a metal surface during PIII, experimental and simulation results showed that the majority of ions gained close to the maximum sheath potential energy. The remaining ions were measured with energies between zero and the full sheath potential energy. In the early stages of the pulse, the presence of ions with less than the full energy is attributed to matrix sheath ions which fall through a fraction of the full sheath potential difference. In the later stages of the pulse, simulation results show that the presence of these ions is due to ion collisions in the sheath and the measurement of ions with trajectories not perpendicular to the RFEA front surface. The RFEA discriminates ions based only on the component of their velocity perpendicular to the RFEA front surface (the z component). A decreasing ion density was measured during the pulse which indicated that the depletion of ions was greater than the generation of ions in the plasma. These results were in contrast to measurements made by others at larger pulse amplitudes which showed an increase in ion density during pulsing [61]. The results of the work in this thesis show that longer pulse-on periods result in more mono-energetic ion implantation but that the ion flux and density will decrease during these longer pulses.

Experimental and simulation results for the IED at an orifice cut into an insulator on the RFEA front surface showed that the insulator potential increases during the PIII pulse. Simulation results for IEDs at the insulator surface away from the orifice had a peak close to the energy associated with the insulator potential. The

ions which produced this peak were from the sheath directly above the region on the insulator where the IED was measured. To maximise the energy of ions bombarding the insulator during PIII, the results of this work show that short pulse lengths must be used to minimise surface charging.

Experimental measurements during PIII with a metal mesh over a metal surface showed that the mesh increased ion flux to the surface. Both experimental and simulation results showed that the IEDs were comprised of a high, medium and low energy peak. Simulations showed that the high energy peak was due to ions from the sheath above the mesh top and the low energy peak was due to ions which collided in the sheath and/or mesh and were able to overcome the space charge potential hump inside the mesh. The medium energy peak was produced by ions from the sheath above the mesh corners which had both a r and z component to their velocity. Both experiment and simulation showed that by increasing the mesh height, the medium energy peak increased in energy. The results of this work showed that larger mesh heights increase the flux of ions to the surface but result in more ions arriving at the surface at angles not perpendicular to the surface and/or with less than the full sheath potential energy.

Simulation results showed that the IED was dependent on position on the RFEA front surface. The high energy peak, produced by ions from the sheath edge above the mesh top, was not observed in IEDs at positions near the mesh cylinder. This was caused by the curvature of the sheath around the mesh corners. This effect could be minimised by keeping the sample being treated well away from the mesh sides so that the sheath edge remains parallel to the sample surface. The medium energy peak, produced by ions from the sheath above the mesh corners, shifted downward in energy for IEDs at positions closer to the mesh cylinder. The variation in the energy distribution with position would produce a non-uniform treatment profile of the surface.

Experimental measurements made through an orifice cut into an insulator showed that insulator surface charging still occurs during PIII when a mesh is fixed over the insulator. The use of the mesh increased the ion flux to the surface. Simulation results of IEDs at the insulator surface showed that the maximum energy of ions

was determined by the insulator surface potential. At positions on the insulator away from the mesh edges, a peak in the IED was observed close to the energy of the insulator surface potential. These ions originated from the sheath edge above the mesh top. In the IEDs at positions close to the mesh edge, the high energy peak is not observed. This is due to the curvature of the sheath around the mesh corners. As for the case with a mesh and no insulator, the placement of the sample well away from the mesh edge would reduce this effect. The results of this work show that to maximise the energy of implanted ions during mesh assisted PIII of an insulator, short pulse lengths must be used to minimise surface charging.

Appendix A

RFEA Circuit Diagram

A diagram of the three stage amplifier circuit used for time resolved ion current measurements is shown in figure A.1. The circuit was designed and built by Mr Phil Denniss at The School of Physics at The University of Sydney.

Ion current from the collector is converted to a voltage signal across a 1 kΩ resisitor (R23) which is then amplified by an OP27 amplifier. Diodes were placed in front of the OP27 to provide protection from current spikes caused by arcing in the RFEA. A LF412 two stage amplifier was used to provide the second and third stages of amplification. The offset of the signal was controlled using a LM611 reference control amplifier. The RFEA collector and circuit board plane of the first three amplifier stages were biased at the collector voltage. A HCPL7800 high voltage isolation amplifier was used to pass the voltage signal from the high voltage side of the circuit board to the grounded side of the circuit board. An AMP03 differential amplifier took the difference between the two outputs of the HCPL7800 which gave the collector ion current as a voltage signal amplified by $8\text{x}10^6$ VA^{-1}.

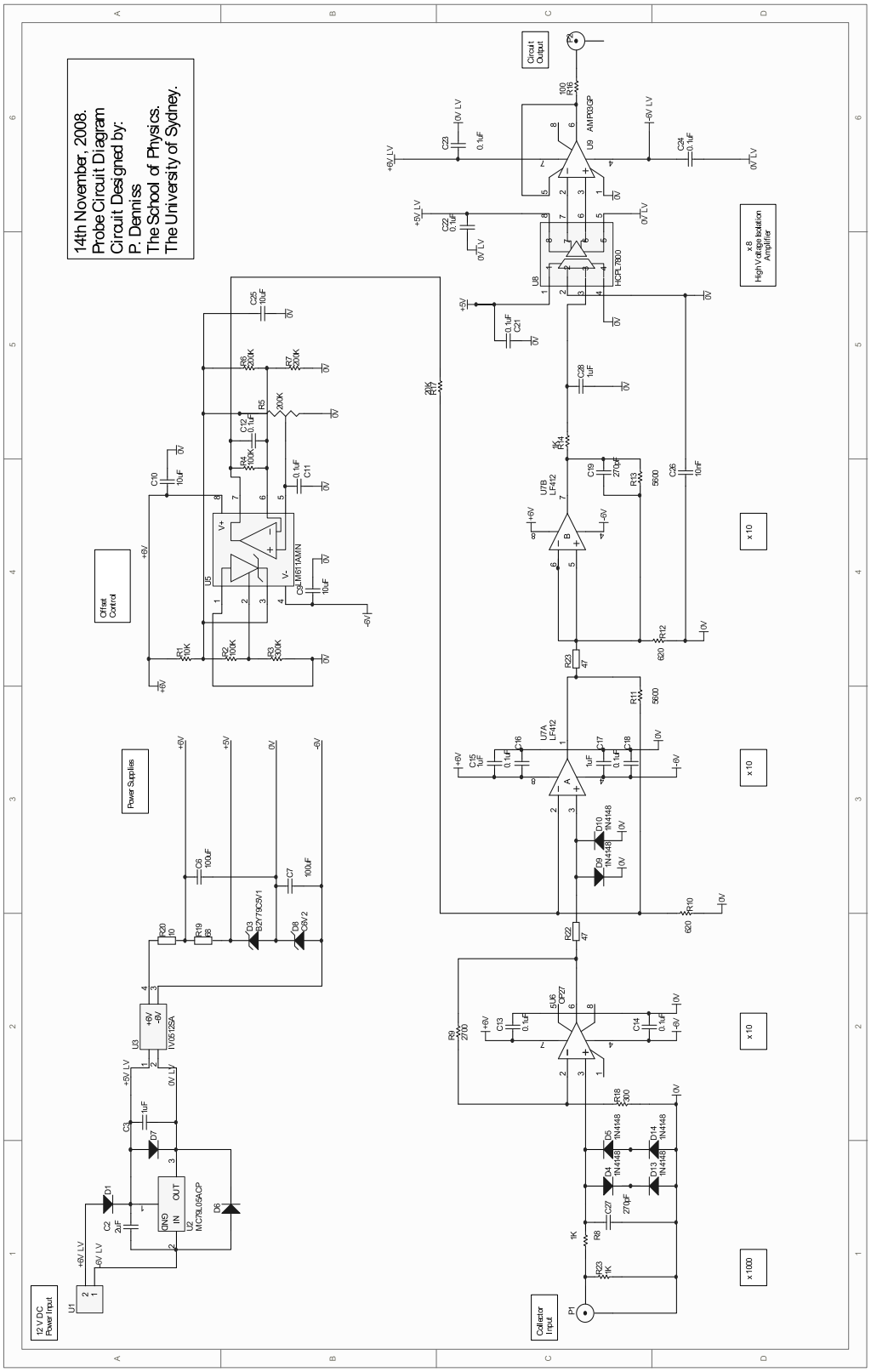

Figure A.1: A diagram of the amplifier circuit used for time resolved ion current measurements with the RFEA.

Appendix B

Simulation of Mesh and Sheath Potentials

In the simulations of ion trajectories, the potentials in the sheath and mesh were determined by solving Poisson's equation, taking into account the decrease in ion density as ions accelerate. The potential in the mesh and sheath regions can be expressed as a finite difference equation. From section 6.3.2, the potential in the mesh and sheath regions is given by equation (6.5)

$$\frac{\partial^2\phi}{\partial r^2} + \left(\frac{1}{r}\right)\left(\frac{\partial\phi}{\partial r}\right) + \left(\frac{\partial^2\phi}{\partial z^2}\right) = K\left(\phi_s - \phi\right)^{-\frac{1}{2}} \tag{B.1}$$

where

$$K = -\left(\frac{J_0}{\epsilon_0}\right)\left(\frac{2e}{M}\right)^{-\frac{1}{2}} \tag{B.2}$$

Equation (B.1) can be expressed as a finite difference equation

$$\begin{aligned} \frac{\phi(r+\Delta r,z) - 2\phi(r,z) + \phi(r-\Delta r,z)}{\Delta r^2} \quad &+ \quad \left(\frac{1}{r}\right)\frac{\phi(r+\Delta r,z) - \phi(r,z)}{\Delta r} + \\ \frac{\phi(r,z+\Delta z) - 2\phi(r,z) + \phi(r,z-\Delta z)}{\Delta z^2} \quad &= \quad K(\phi_s - \phi(r,z))^{-\frac{1}{2}} \end{aligned} \tag{B.3}$$

which can be rearranged to give

$$A\phi(r,z) + B + C(\phi_s - \phi(r,z))^{-\frac{1}{2}} = 0 \tag{B.4}$$

where

$$\begin{aligned} A &= -2r(\Delta z^2 + \Delta r^2) - \Delta r \Delta z^2 && \text{(B.5)} \\ B &= r\Delta z^2(\phi(r+\Delta r, z) + \phi(r-\Delta r, z)) + \Delta r \Delta z^2 \phi(r+\Delta r, z) \\ &\quad + r\Delta r^2(\phi(r, z+\Delta z) + \phi(r, z-\Delta z)) && \text{(B.6)} \\ C &= -r\Delta r^2 \Delta z^2 K && \text{(B.7)} \end{aligned}$$

A final rearrangement gives

$$\phi(r,z) + F + G(\phi_s - \phi)^{-\frac{1}{2}} = 0 \tag{B.8}$$

where

$$F = \left(\frac{B}{A}\right) \quad \text{and} \quad G = \left(\frac{C}{A}\right)$$

Using the computer program Mathematica, the three solutions to equation (B.8) are

$$\phi = \frac{1}{3}(\phi_s - 2F) - \frac{2^{\frac{1}{3}}M}{3N} + \frac{1}{3\left(2^{\frac{1}{3}}\right)}N \tag{B.9}$$

$$\phi = \frac{1}{3}(\phi_s - 2F) + \frac{\left(1+i\sqrt{3}\right)M}{3\left(2^{\frac{2}{3}}\right)N} - \frac{1}{6\left(2^{\frac{1}{3}}\right)}\left(1-i\sqrt{3}\right)N \tag{B.10}$$

$$\phi = \frac{1}{3}(\phi_s - 2F) + \frac{\left(1-i\sqrt{3}\right)M}{3\left(2^{\frac{2}{3}}\right)N} - \frac{1}{6\left(2^{\frac{1}{3}}\right)}\left(1+i\sqrt{3}\right)N \tag{B.11}$$

where

$$M = -\phi_s^2 - 2\phi_s F - F^2 \tag{B.12}$$

$$N = \left(2\phi_s^3 + 6\phi_s^2 F + 6\phi_s F^2 + 2F^3 - 27G^2\right)^{\frac{1}{3}} + \left(3\sqrt{3}\sqrt{-4\phi_s^3 G^2 - 12\phi_s^2 F G^2 - 12\phi_s F^2 G^2 - 4F^3 G^2 + 27G^4}\right)^{\frac{1}{3}} \tag{B.13}$$

For each iteration in the program, equations (B.9), (B.10) and (B.11) were used to determine the value of potential at each point in the array. This process was repeated until the maximum difference in potential, at each point, between iterations was less than $1\text{x}10^{-7}$ percent. Equation (B.9) was found to produce non-converging solutions while equations (B.10) and (B.11) converged to the same solution. The potential array was plotted using the converged, real value solution of equation (B.10).

References

[1] I. C. Abraham, J. R. Woodworth, M. E. Riley, P. A. Miller, and T. W. Hamilton. Ion energy distributions versus frequency and ion mass at the rf-biased electrode in an inductively driven discharge. *Journal of Vacuum Science and Technology A*, 20(5):1759–1768, 2002.

[2] A. Agarwal and M. J. Kushner. Characteristics of pulsed plasma doping sources for ultrashallow junction formation. *Journal of Applied Physics*, 101:063305–1–063305–16, 2007.

[3] A. Anders. Metal plasma immersion ion implantation and deposition: a review. *Surface and Coatings Technology*, 93:158–167, 1997.

[4] A. Anders. Energetic deposition using filtered cathodic arc plasmas. *Vacuum*, 67:673–686, 2002.

[5] J. Banský, A. Brockhaus, J. Engemann, Y. Yuan, L. Livovský, and S. Slosarčík. Integrated 3D-LTCC sensors for "in-situ" plasma diagnositcs. In *ISHM 1995. International Symposium on Microelectronics*, volume 2649, pages 119–124, Los Angeles CA, USA, 1995. SPIE-International Society of Optical Engineers.

[6] E. V. Barnat, T.-M. Lu, and J. Little. Pulse bias sputtering of copper onto insulating surfaces. *Journal of Applied Physics*, 90(10):4946–4950, 2001.

[7] N. P. Barradas, A. J. H. Maas, S. Mändl, and R. Günzel. Alpha-elastic recoil detection analysis of the energy distribution of oxygen ions implanted into

silicon with plasma immersion ion implantation. *Journal of Applied Physics*, 81(10):6642–6650, 1997.

[8] E. C. Benck, A. Goyette, and Y. Wang. Ion energy distribution and optical measurements in high-density, inductively coupled C_4F_6 discharges. *Journal of Applied Physics*, 94(3):1382–1389, 2003.

[9] P. Benoit-Cattin and L. Bernard. Anomalies of the Energy of Positive Ions Extracted from High-Frequency Ion Sources. A Theoretical Study. *Journal of Applied Physics*, 39(12):5723–5726, 1968.

[10] M. G. Blain, J. E. Stevens, and J. R. Woodworth. High-resolution submicron retarding field energy analyzer for low-temperature plasma analysis. *Applied Physics Letters*, 75(25):3923–3925, 1999.

[11] C. Blawert, B. L. Mordike, G. A. Collins, K. T. Short, and J. Tendys. Influence of process parameters on the nitriding of steels by plasma immersion ion implantation. *Surface and Coatings Technology*, 103-104:240–247, 1998.

[12] C. Böhm and J. Perrin. Retarding-field analyzer for measurements of ion energy distributions and secondary electron emission coefficients in low-pressure radio frequency discharges. *Review of Scientific Instruments*, 64(1):31–44, 1993.

[13] R. W. Boswell and D. Vender. An experimental study of breakdown in a pulsed Helicon plasma. *Plasma Sources Science and Technology*, 4:534–540, 1995.

[14] P. Briaud, G. Turban, and B. Grolleau. Energy distribution of ions in plasma etching reactors. *Materials Research Society Symposia Proceedings*, 68:109–114, 1986.

[15] B. Briel and H. M. Urbassek. Simulation of sheath dynamics and current nonuniformity in plasma-immersion ion implantation of a patterned surface. *Journal of Applied Physics*, 93(8):4420–4431, 2003.

[16] J. Brückner, R. Günzel, E. Richter, and W. Möller. Metal plasma immersion ion implantation and deposition (MPIIID): chromium on magnesium. *Surface and Coatings Technology*, 103-104:227–230, 1998.

[17] E. A. Burke. Secondary emission from polymers. *IEEE Transactions on Nuclear Science*, NS-27(6):1760–1764, 1980.

[18] Y. Chang and D. Wang. Corrosion behaviour of electroless nickel-coated AISI 304 stainless steel enhanced by titanium ion implantation. *Surface and Coatings Technology*, 200:2187–2191, 2005.

[19] C. K. Chao and S. Y. Su. On accuracy of RPA measurements of ion fluxes. *Advances in Space Research*, 23(8):1537–1540, 1999.

[20] B. Chapman. *Glow Discharge Processes*. John Wiley and Sons, New York, 1980.

[21] C. Charles, R. W. Boswell, A. Bouchoule, C. Laure, and P. Ranson. Plasma diffusion from a low pressure radio frequency source. *Journal of Vacuum Science and Technology A*, 9(3):661–663, 1991.

[22] C. Charles, A. W. Degeling, T. E. Sheridan, J. H. Harris, M. A. Lieberman, and R. W. Boswell. Absolute measurements and modeling of radio frequency electric fields using a retarding field energy analyzer. *Physics of Plasmas*, 7(12):5232–5241, 2000.

[23] S. -M. Chen, R. M. Gwilliam, and B. J. Sealy. Computer simulation of plasma immersion ion implantation. *Radiation Effects and Defects in Solids*, 141:149–159, 1997.

[24] Y. Cho, H. June Lee, C. Park, H. Lee, and S. Lee. Ion beam generation from sheath field of grid electrode and its application to surface treatment. *Journal of Applied Physics*, 100:123303–123303–5, 2006.

[25] J. W. Coburn and E. Kay. Positive-ion bombardment of substrates in rf diode glow discharge sputtering. *Journal of Applied Physics*, 43(12):4965–4971, 1972.

[26] G. A. Collins, R. Hutchings, K. T. Short, J. Tendys, X. Li, and M. Samandi. Nitriding of austenitic stainless steel by plasma immersion ion implantation. *Surface and Coatings Technology*, 74-75:417–424, 1995.

[27] J. R. Conrad, J. L. Radtke, R. A. Dodd, F. J. Worzala, and N. C. Tran. Plasma source ion-implantation technique for surface modification of materials. *Journal of Applied Physics*, 62(11):4591–4596, 1987.

[28] G. D. Conway and A. J. Perry. Design and operation of a high power water cooled retarding field energy analyser (RFEA). Technical report, Plasma Research Laboratory, Research School of Physical Sciences and Engineering, Australian National University, February 1996.

[29] W. H. Cramer. Elastic and inelastic scattering of low-velocity ions: Ne^+ in A, A^+ in Ne, and A^+ in A. *The Journal of Chemical Physics*, 30(3):641–642, 1959.

[30] Y. Cui, Y. Zou, A. Valfells, M. Reiser, M. Walter, I. Haber, R. A. Kishek, S. Bernal, and P. G. O'Shea. Design and operation of a retarding field energy analyzer with variable focusing for space-charge-dominated electron beams. *Review of Scientific Instruments*, 75(8):2736–2745, 2004.

[31] C. P. DeNeef and A. J. Theiss. Effect of finite analyzer size on the distribution functions measured in field-free plasmas. *The Review of Scientific Instruments*, 50(3):378–381, 1979.

[32] M. Dhayal, D. Forder, K. L. Parry, R. D. Short, and J. W. Bradley. Using an afterglow plasma to modify polystyrene surfaces in pulsed radio frequency (RF) argon discharges. *Surface and Coatings Technology*, 173-174:872–876, 2003.

[33] H. Dong and T. Bell. State-of-the-art overview: ion beam surface modification of polymers towards improving tribological properties. *Surface and Coatings Technology*, 111:29–40, 1999.

[34] C. Donolato. Application of Green's differential equation to the analysis of ion-matrix sheaths around wedge-shaped cathodes. *Journal of Physics D: Applied Physics*, 38:397–402, 2005.

[35] B. Drevillon, J. Perrin, J. M. Siefert, J. Huc, A. Lloret, G. de Rosny, and J. P. M. Schmitt. Growth of hydrogenated amorphous silicon due to controlled ion bombardment from a pure silane plasma. *Applied Physics Letters*, 42(9):801–803, 1983.

[36] E. A. Edelberg, A. Perry, N. Benjamin, and E. S. Aydil. Compact floating ion energy analyzer for measuring energy distributions of ions bombarding radio-frequency biased electrode surfaces. *Review of Scientific Instruments*, 70(6):2689–2698, 1999.

[37] E. A. Edelberg, A. Perry, N. Benjamin, and E. S. Aydil. Energy distribution of ions bombarding biased electrodes in high density plasma reactors. *Journal of Vacuum Science and Technology A*, 17(2):506–516, 1999.

[38] W. Ensinger, K. Volz, and T. Höchbauer. Three-dimensional dose uniformity of plasma immersion ion implantation shown with the example of macro-trenches. *Surface and Coatings Technology*, 120-121:347–352, 1999.

[39] W. Ensinger, K. Volz, and T. Höchbauer. Plasma immersion ion implantation of complex-shaped objects: experimental study on the treatment homogeneity. *Surface and Coatings Technology*, 128-129:265–269, 2000.

[40] DuPont Teijin Films. *Mylar Polyester Film Product Information*. Hopewell, VA, USA, 2003. `http://usa.dupontteijinfilms.com/informationcenter/downloads/Electrical_Properties.pdf`.

[41] R. K. Y. Fu, P. K. Chu, and X. Tian. Influence of thickness and dielectric properties on implantation efficacy in plasma immersion ion implantation of insulators. *Journal of Applied Physics*, 95(7):3319–3323, 2004.

[42] R. K. Y. Fu, K. Y. Fu, X. Tian, and P. K. Chu. Effects of mesh-assisted carbon plasma immersion ion implantation on the surface properties of insu-

lating silicon carbide ceramics. *Journal of Vacuum Science and Technology A*, 22(2):356–360, 2004.

[43] R. K. Y. Fu, Y. F. Mei, G. J. Wan, G. G. Siu, P. K. Chu, Y. X. Huang, X. B. Tian, S. Q. Yang, and J. Y. Chen. Surface composition and surface energy of Teflon treated by metal plasma immersion ion implantation. *Surface Science*, 573:426–432, 2004.

[44] R. K. Y. Fu, X. Tian, and P. K. Chu. Enhancement of implantation energy using a conducting grid in plasma immersion ion implantation of dielectric/polymeric materials. *Review of Scientific Instruments*, 74(8):3697–3700, 2003.

[45] V. Georgieva, A. Bogaerts, and R. Gijbels. Numerical investigation of ion-energy distribution functions in single and dual frequency capacitively coupled plasma reactors. *Physical Review E*, 69:026406–1–026406–11, 2004.

[46] L. Godet, Z. Fang, S. Radovanov, S. Walther, E. Arevalo, F. Lallement, J. T. Scheuer, T. Miller, D. Lenoble, G. Cartry, and C. Cardinaud. Plasma doping implant depth profile calculation based on ion energy distribution measurements. *Journal of Vacuum Science and Technology B*, 24(5):2391–2397, 2006.

[47] V. A. Godyak. *Soviet Radio Frequency Discharge Research.* Delphic Associates, Falls Church, VA, USA, 1987.

[48] A. Hallil, O. Zabeida, M. R. Wertheimer, and L. Martinu. Mass-resolved ion energy distributions in continuous dual mode microwave/radio frequency plasmas in argon and nitrogen. *Journal of Vacuum Science and Technology A*, 18(3):882–891, 2000.

[49] E. Hoffmann and V. Stroobant. *Mass Spectrometry. Principles and Applications.* John Wiley and Sons Ltd., England, 3rd edition, 2008.

[50] J. H. Hong, Y. Lee, S. Han, and K. Kim. Improvement of adhesion properties for Cu films on the polyimide by plasma source ion implantation. *Surface and Coatings Technology*, 201:197–202, 2006.

[51] Y. X. Huang, X. B. Tian, S. Q. Yang, R. K. Y. Fu, and P. K. Chu. Particle-in-cell numerical simulation of non-uniform plasma immersion ion implantation. *Surface and Coatings Technology*, 201:5458–5462, 2007.

[52] P. Huber, D. Manova, S. Mändal, and B. Rauschenbach. Formation of TiN, TiC and TiCN by metal plasma immersion ion implantation and deposition. *Surface and Coatings Technology*, 174-175:1243–1247, 2003.

[53] D. A. Huchital and J. D. Rigden. Resolution and sensitivity of the spherical-grid retarding potential analyzer. *Journal of Applied Physics*, 43(5):2291–2302, 1972.

[54] I. H. Hutchinson. Plasma particle flux. In *Principles of Plasma Diagnostics*, pages 50–87. Cambridge University Press, New York, 1987.

[55] T. Ikehata, K. Shioya, N. Y. Sato, and K. Yukimura. Positive pulse bias method for a high-throughput PBII processing system. *Surface and Coatings Technology*, 186:209–213, 2004.

[56] S. G. Ingram and N. St. J. Braithwaite. Ion and electron energy analysis at a surface in an RF discharge. *Journal of Physics D: Applied Physics*, 21:1496–1503, 1988.

[57] N. Iwama, T. Lehner, H. Noziri, and M. Okada. Three-dimensional reconstruction of the ion velocity distribution of plasma with a retarding-grid analyzer. *Applied Physics Letters*, 52(2):96–97, 1988.

[58] E. C. Jones and N. W. Cheung. Characteristics of Sub-100-nm p^+/n Junctions Fabricated by Plasma Immersion Ion Implantation. *IEEE Electron Device Letters*, 14(9):444–446, 1993.

[59] E. Kawamura, V. Vahedi, M. A. Lieberman, and C. K. Birdsall. Ion energy distributions in rf sheaths; review, analysis and simulation. *Plasma Sources Science and Technology*, 8:R45–R64, 1999.

[60] G. Keller, S. Mändl, U. Rüde, and B. Rauschenbach. Ion mass and scaling effects in PIII simulation. *Surface and Coatings Technology*, 136:117–121, 2001.

[61] P. L. Kellerman, J. D. Bernstein, and M. P. Bradley. Ion Energy Distributions in Plasma Immersion Ion Implantation- Theory and Experiment. In *Conference on Ion Implantation Technology 2000*, pages 484–487, 2000.

[62] D. Kim and D. J. Economou. Simulation of a two-dimensional sheath over a flat wall with an insulator/conductor interface exposed to a high density plasma. *Journal of Applied Physics*, 94(5):2852–2857, 2003.

[63] D. Kim and D. J. Economou. Simulation of a two-dimensional sheath over a flat insulator-conductor interface on a radio frequency biased electrode in a high density plasma. *Journal of Applied Physics*, 95(7):3311–3318, 2004.

[64] D. Kim, D. J. Economou, J. R. Woodworth, P. A. Miller, R. J. Shul, B. P. Aragon, T. W. Hamilton, and C. G. Willison. Plasma Molding Over Surface Topography: Simulation and Measurement of Ion Fluxes, Energies and Angular Distributions Over Trenches in RF High Density Plasmas. *IEEE Transactions on Plasma Science*, 31(4):691–702, 2003.

[65] Y. Kim, Y. Lee, S. Han, and K. Kim. Improvement of hydrophobic properties of polymer surfaces by plasma source ion implantation. *Surface and Coatings Technology*, 200:4763–4769, 2006.

[66] K. Köhler, J. W. Coburn, D. E. Horne, and E. Kay. Plasma potentials of 13.56-MHz rf argon glow discharges in a planar system. *Journal of Applied Physics*, 57(1):59–66, 1985.

[67] A. Kondyurin, B. K. Gan, M. M. M. Bilek, K. Mizuno, and D. R. McKenzie. Etching and structural changes of polystyrene films during plasma immersion ion implantation from argon plasma. *Nuclear Instruments and Methods in Physics Research B*, 251:413–418, 2006.

[68] B. Koo, Z. Fang, L. Godet, S. B. Radovanov, C. Cardinaud, G. Cartry, A. Grouillet, and D. Lenoble. Plasma Diagnostics in Pulsed Plasma Dop-

ing (P^2LAD) System. *IEEE Transactions on Plasma Science*, 32(2):456–463, 2004.

[69] K. G. Kostov, J. J. Barroso, and M. Ueda. Two Dimensional Computer Simulation of Plasma Immersion Ion Implantation. *Brazilian Journal of Physics*, 34(4B):1689–1695, 2004.

[70] H. M. Küdyan. Interpretation of electrostatic energy analyzer data of a flowing plasma. *The Review of Scientific Instruments*, 49(1):8–10, 1978.

[71] D. T. K. Kwok and C. Cornet. Numerical Simulation of Metal Plasma Immersion Ion Implantation (MePIIID) on a Sharp Cone and a Fine Tip by a Multiple-Grid Particle-in-Cell (PIC) Method. *IEEE Transactions on Plasma Science*, 34(5):2434–2442, 2006.

[72] S. C. H. Kwok, G. J. Wan, J. P. Y. Ho, P. K. Chu, M. M. M. Bilek, and D. R. McKenzie. Characteristics of phosphorus-doped diamond-like carbon films synthesized by plasma immersion ion implantation and deposition (PIII and D). *Surface and Coatings Technology*, 201:6643–6646, 2007.

[73] F. Lallement, A. Grouillet, M. Juhel, J.-P. Reynard, D. Lenoble, Z. Fang, S. Walther, Y. Rault, L. Godet, and J. Scheuer. Fabrication of N^+/P ultra-shallow junctions by plasma doping for 65 nm CMOS technology. *Surface and Coatings Technology*, 186:17–20, 2004.

[74] E. Leal-Quiros and M. A. Prelas. An Enhancement of Ion Energy Spectra Resolution and Sensitivity in a Multigrided Energy Analyzer with a Retarding Grid Potential: The Variable Energy Analyzer (VEA). *IEEE Transactions on Plasma Science*, 16(6):661–666, 1988.

[75] D. H. Lee, X. M. He, K. C. Walter, M. Nastasi, J. R. Tesmer, M. Tuszewski, and D. R. Tallant. Diamondlike carbon deposition on silicon using radio-frequency inductive plasma of Ar and C_2H_2 gas mixture in plasma immersion ion deposition. *Applied Physics Letters*, 73(17):2423–2425, 1998.

[76] L. H. Li, J. Z. Tian, X. Cai, Q. L. Chen, M. Xu, Y. Q. Wu, R. K. Y. Fu, and P. K. Chu. Influence of ion energies on the surface morphology of carbon films. *Surface and Coatings Technology*, 196:241–245, 1005.

[77] J. H. Liang, C. S. Wang, W. F. Tsai, and C. F. Ai. Parametric study of nitrided AISI 304 austenite stainless steel prepared by plasma immersion ion implantation. *Surface and Coatings Technology*, 201:6638–6642, 2007.

[78] M. Lieberman. Analytical Solution for Capacitive RF Sheath. *IEEE Transactions on Plasma Science*, 16(6):638–644, 1988.

[79] M. Lieberman. Dynamics of a Collisional, Capacitive RF Sheath. *IEEE Transactions on Plasma Science*, 17(2):338–341, 1989.

[80] M. A. Lieberman. Model of plasma immersion ion implantation. *Journal of Applied Physics*, 66(7):2926–2929, 1989.

[81] M. A. Lieberman and A. J. Lichtenberg. *Principles of Plasma Discharges and Materials Processing*. John Wiley and Sons Inc., New York, 1994.

[82] B. P. Linder and N. W. Cheung. Plasma Immersion Ion Implantation with Dielectric Substrates. *IEEE Transactions on Plasma Science*, 24(6):1383–1388, 1996.

[83] B. P. Linder and N. W. Cheung. The Effect of Collisions on Pulsed and DC Plasma Immersion Ion Implantation. In J. Matsuo, G. Takaoka, and I. Yamada, editors, *1998 International Conference on Ion Implantation Technology*, volume 2, pages 1183–1186, Kyoto, Japan, 1998.

[84] B. P. Linder and N. W. Cheung. Modeling of energy distributions for plasma implantation. *Surface and Coatings Technology*, 136:132–137, 2001.

[85] J. Liu, G. L. Huppert, and H. H. Sawin. Ion bombardment in rf plasmas. *Journal of Applied Physics*, 68(8):3916–3934, 1990.

[86] J. Lutz, A. Lehmann, and S. Mändl. Nitrogen diffusion in medical CoCrNiW alloys after plasma immersion ion implantation. *Surface and Coatings Technology*, 202:3747–3753, 2008.

[87] S. Mändl, N. P. Barradas, J. Brutscher, R. Günzel, and W. Möller. Comparison of measured and calculated dose for plasma source ion implantation into 3-D objects. *Nuclear Instruments and Methods in Physics Research B*, 127/128:996–999, 1997.

[88] S. Mändl, J. Brutscher, R. Günzel, and W. Möller. Ion energy distribution in plasma immersion ion implantation. *Surface and Coatings Technology*, 93:234–237, 1997.

[89] S. Mändl, D. Manova, and B. Rauschenbach. Transparent AlN layers formed by metal plasma immersion ion implantation and deposition. *Surface and Coatings Technology*, 186:82–87, 2004.

[90] A. Manenschijn, G. C. A. M. Janssen, E. van der Drift, and S. Radelaar. Measurement of ion impact energy and ion flux at the rf electrode of a parallel plate reactive ion etcher. *Journal of Applied Physics*, 69(3):1253–1262, 1991.

[91] D. Martin and H. Oechsner. Time resolved analysis of ion motion in an oscillating plasma sheath. *Vacuum*, 47(6-8):1017–1022, 1996.

[92] S. Masamune and K. Yukimura. Model for ion extraction from pulsed plasma source for plasma based ion implantation (PBII). *Review of Scientific Instruments*, 71(2):1187–1190, 2000.

[93] J. N. Matossian, R. W. Schumacher, and D. M. Pepper. U.S. Patent Number 5374456. Surface potential control in plasma processing of materials, Hughes Aircraft Company, Los Angeles CA, 1994.

[94] J. Meichsner, M. Zeuner, B. Krames, M. Nitschke, R. Rochotzki, and K. Barucki. Plasma diagnostics for surface modification of polymers. *Surface and Coatings Technology*, 98:1565–1571, 1998.

[95] A. Meige, M. Jarnyk, D. T. K. Kwok, and R. W. Boswell. Particle-in-cell simulation of an electron shock wave in a rapid rise time plasma immersion ion implantation process. *Physics of Plasmas*, 12:435031–435034, 2005.

[96] Y. Miyagawa, H. Nakadate, M. Tanaka, M. Ikeyama, S. Nakao, and S. Miyagawa. PIC simulation of N_2 and C_2H_2 plasma behavior around plural objects. *Surface and Coatings Technology*, 201:8414–8419, 2007.

[97] N. Mizutani and T. Hayashi. Ion energy distribution at an r.f.-biased electrode in an inductively coupled plasma affected by collisions in a sheath. *Thin Solid Films*, 374:167–174, 2000.

[98] A. W. Molvik. Large acceptance angle retarding-potential analyzers. *The Review of Scientific Instruments*, 52(5):704–711, 1981.

[99] H. M. Mott-Smith and I. Langmuir. The theory of collectors in gaseous discharges. *Physical Review*, 28:727–763, 1926.

[100] N. J. Nosworthy, J. P. Y. Ho, A. Kondyurin, D. R. McKenzie, and M. M. M. Bilek. The attachment of catalase and poly-L-lysinie to plasma immersion ion implantation-treated polyethylene. *Acta Biomaterialia*, 3:695–704, 2007.

[101] T. W. H. Oates, D. R. McKenzie, and M. M. M. Bilek. Plasma immersion ion implantation using polymeric substrates with a sacrificial conductive surface layer. *Surface and Coatings Technology*, 156:332–337, 2002.

[102] S. Okuji, M. Sekiya, M. Nakabayashi, H. Endo, N. Sakudo, and K. Nagai. Surface modification of polymeric substrates by plasma-based ion implantation. *Nuclear Instruments and Methods in Physics Research B*, 242:353–356, 2006.

[103] M. Paulus, B. Rauschenbach, L. Stals, and U. Rüde. Simulation of Plasma-Immersed Implantation of Trenches. In J. Matsuo, G. Takaoka, and I. Yamada, editors, *International Conference on Ion Implantation Technology*, volume 2, pages 1187–1190, Kyoto, Japan, 1998.

[104] J. Pelletier and A. Anders. Plasma-Based Ion Implantation and Deposition: A Review of Physics, Technology and Applications. *IEEE Transactions on Plasma Science*, 33(6):1944–1959, 2005.

[105] J. Perrin, Y. Takeda, N. Hirano, H. Matsuura, and A. Matsuda. Effect of Ion Bombardment on the Growth and Properties of Hyrdogenated Amorphous Silicon-Germanium Alloys. *Japanese Journal of Applied Physics*, 28(1):5–11, 1989.

[106] I. Pintér, A. H. Abdulhadi, Zs. Makaró, N. Q. Khanh, M. Ádám, I. Bársony, J. Poortmans, S. Sivoththaman, Hai-Zhi Song, and G. J. Adriaenssens. Plasma immersion ion implantation for shallow junctions in silicon. *Applied Surface Science*, 138-139:224–227, 1999.

[107] R. A. Pitts, R. Chavan, S. J. Davies, S. K. Erents, G. Kaveney, G. F. Matthews, G. Neill, J. E. Vince, JET-EFDA workprogramme contributors, and I. Duran. Retarding field energy analyzer for the JET plasma boundary. *Review of Scientific Instruments*, 74(11):4644–4657, 2003.

[108] A. M. Pointu. Model of electrical properties of rf diode discharges. *Revue de Physique Appliquee*, 24(3):257–76, 1989.

[109] R. C. Powles, D. T. K. Kwok, D. R. McKenzie, and M. M. M. Bilek. Simulation of a semitransparent conducting mesh electrode for plasma immersion ion implantation. *Physics of Plasmas*, 12:0935071–0935076, 2005.

[110] S. Qi, W. Zhiwei, G. Changxin, and H. Zhongyi. Study on the treatment capability of a plasma-based ion implanting trench-shaped target. *Modelling and Simulation in Materials Science and Engineering*, 13:829–839, 2005.

[111] S. Qin, C. Chan, and Z. Jin. Plasma immersion ion implantation model including multiple charge state. *Journal of Applied Physics*, 79(7):3432–3437, 1996.

[112] S. Qin, C. Chan, and N. E. McGruer. Energy distribution of boron ions during

plasma immersion ion implantation. *Plasma Sources Science and Technology*, 1(1):1–6, 1992.

[113] S. Radovanov, L. Godet, R. Dorai, Z. Fang, B. W. Koo, C. Cardinaud, G. Cartry, D. Lenoble, and A. Grouillet. Ion energy distributions in a pulsed plasma doping system. *Journal of Applied Physics*, 98:1133071–1133078, 2005.

[114] Rajkumer, M. Kumar, P. J. George, S. Mukherjee, and K. S. Chari. Effects of nitrogen and argon plasma-immersion ion implantation on silicon and its oxidation. *Surface and Coatings Technology*, 156:253–257, 2002.

[115] D. Rapp and P. Englander-Golden. Total Cross Sections for Ionization and Attachment in Gases by Electron Impact. I. Positive Ionization. *The Journal of Chemical Physics*, 43(5):1464–1479, 1965.

[116] D. L. Rudakov, M. G. Shats, R. W. Boswell, C. Charles, and J. Howard. Overview of probe diagnostics on the H-1 heliac. *Review of Scientific Instruments*, 70(1):476–479, 1999.

[117] Y. Sakai and I. Katsumata. An Energy Resolution Formula of a Three Plane Grids Retarding Field Energy Analyser. *Japanese Journal of Applied Physics*, 24(3):337–341, 1985.

[118] J. T. Scheuer, M. Shamim, and J. R. Conrad. Model of plasma source ion implantation in planar, cylindrical, and spherical geometries. *Journal of Applied Physics*, 67(3):1241–1245, 1990.

[119] M. Schiller and W. Kulisch. Plasma properties at the transition from remote to direct plasma. *Surface and Coatings Technology*, 98:1590–1599, 1998.

[120] W. Schwarzenbach, A. A. Howling, M. Fivaz, S. Brunner, and Ch. Hollenstein. Sheath impedance effects in very high frequency plasma experiments. *Journal of Vacuum Science and Technology A*, 14(1):132–138, 1996.

[121] J. Sheffield. *Plasma Scattering of Electromagnetic Radiation*. Academic Press, New York, 1975.

[122] T. E. Sheridan. Sheath expansion at a corner. *Journal of Physics D: Applied Physics*, 29:2725–2728, 1996.

[123] T. E. Sheridan. A model of plasma-based ion implantation around a round hole in a flat plate. *Journal of Physics D: Applied Physics*, 32:886–890, 1999.

[124] M. S. Silberberg. *Chemistry. The Molecular Nature of Matter and Change.* McGraw Hill, Boston, 2nd edition, 2000.

[125] J. A. Simpson. Design of Retarding Field Energy Analyzers. *The Review of Scientific Instruments*, 32(12):1283–1293, 1961.

[126] B. A. Smith and L. J. Overzet. Time-resolved energy distribution of F^- from pulsed radio frequency discharges. *Journal of Applied Physics*, 78(8):5195–5197, 1995.

[127] R. J. M. M. Snijkers, M. J. M. van Sambeek, G. M. W. Kroesen, and F. J. de Hoog. Mass-resolved ion energy measurements at the grounded electrode of an argon rf plasma. *Applied Physics Letters*, 63(3):308–310, 1993.

[128] K. R. Spangenberg. *Vacuum Tubes.* McGraw-Hill Electrical and Electronic Engineering Series. McGraw-Hill Book Company, New York, 1st edition, 1948.

[129] R. A. Stewart and M. A. Lieberman. Model of plasma immersion ion implantation for voltage pulses with finite rise and fall times. *Journal of Applied Physics*, 70(7):3481–3487, 1991.

[130] J. H. Sui and W. Cai. Effect of bias voltage on the structure and the electrochemical corrosion behavior of hydrogenated amorphous carbon (a-C:H) films on NiTi alloys. *Surface and Coatings Technology*, 201:6906–6909, 2007.

[131] F. Thièry, C. Vallée, Y. Arnal, and J. Pelletier. PECVD and PIID processing of diamondlike carbon. *Surface and Coatings Technology*, 186:146–152, 2004.

[132] X. Tian, K. Y. Fu, P. K. Chu, and S. Q. Yang. Plasma immersion ion implantation of insulating materials. *Surface and Coatings Technology*, 196:162–166, 2005.

[133] X. Tian, R. K. Y. Fu, J. Chen, P. K. Chu, and I. G. Brown. Charging of dielectric substrate materials during plasma immersion ion implantation. *Nuclear Instruments and Methods in Physics Research B*, 187:485–491, 2002.

[134] X. B. Tian, D. T. K. Kwok, and P. K. Chu. Modeling of incident particle energy distribution in plasma immersion ion implantation. *Journal of Applied Physics*, 88(9):4961–4966, 2000.

[135] M. F. Toups and D. W. Ernie. Pressure and frequency dependence of ion bombardment energy distributions from rf discharges. *Journal of Applied Physics*, 68(12):6125–6132, 1990.

[136] P. Tsai, K. Chang-Liao, H. Y. Kao, T. K. Wang, S. F. Huang, W. F. Tsai, and C. F. Ai. Improved electrical characteristics of high-k gated MOS devices by nitrogen incorporation with plasma immersion ion implantation (PIII). *Microelectronic Engineering*, 84:2192–2195, 2007.

[137] I. Tsyganov, M. F. Maitz, E. Wieser, F. Prokert, E. Richter, and A. Rogozin. Structure and properties of titanium oxide layers prepared by metal plasma immersion ion implantation and deposition. *Surface and Coatings Technology*, 174-175:591–596, 2003.

[138] M. Ueda, L. A. Berni, R. M. Castro, A. F. Beloto, E. Abramof, J. O. Rossi, J. J. Barroso, and C. M. Lepienski. Surface improvements of industrial components treated by plasma immersion ion implantation (PIII): results and prospects. *Surface and Coatings Technology*, 156:71–76, 2002.

[139] V. Vahedi, M. A. Lieberman, M. V. Alves, J. P. Verboncoeur, and C. K. Birdsall. A one-dimensional collisional model for plasma-immersion ion implantation. *Journal of Applied Physics*, 69(4):2008–2014, 1991.

[140] J. J. Vajo, J. D. Williams, R. Wei, R. G. Wilson, and J. N. Matossian. Plasma ion implantation of nitrogen into silicon: Characterization of the depth profiles of implanted ions. *Journal of Applied Physics*, 76(10):5666–5675, 1994.

[141] S. A. Voronin, M. R. Alexander, and J. W. Bradley. Time-resolved measurements of the ion energy distribution function in a pulsed discharge using a double gating technique. *Measurement Science and Technology*, 16:2446–2452, 2005.

[142] K. C. Walter, J. T. Scheuer, P. C. McIntyre, P. Kodali, N. Yu, and M. Nastasi. Increased wear resistance of electrodeposited chromium through applications of plasma source ion implantation techniques. *Surface and Coatings Technology*, 85:1–6, 1996.

[143] A. S. Wan, T. F. Yang, B. Lipschultz, and B. LaBombard. Janus, a bidirectional, multifunctional plasma diagnostic. *Review of Scientific Instruments*, 57(8):1542–1551, 1986.

[144] L. Wang, L. Huang, Y. Wang, Z. Xie, and X. Wang. Duplex DLC coatings fabricated on the inner surface of a tube using plasma immersion ion implantation and deposition. *Diamond and Related Materials*, 17:43–47, 2008.

[145] L. Wang, S. Zhao, Z. Xie, L. Huang, and X. Wang. MoS_2/Ti multilayer deposited on 2Cr13 substrate by PIIID. *Nuclear Instruments and Methods in Physics Research B*, 266:730–733, 2008.

[146] P. A. Watterson. Child-Langmuir sheath structure around wedge-shaped cathodes. *Journal of Physics D: Applied Physics*, 22:1300–1307, 1989.

[147] Ch. Wild and P. Koidl. Structured ion energy distribution in radio frequency glow-discharge systems. *Applied Physics Letters*, 54(6):505–507, 1989.

[148] B. P. Wood, D. J. Rej, A. Anders, I. G. Brown, R. J. Faehl, S. M. Malik, and C. P. Munson. Fundamentals of Plasma Immersion Ion Implantation. In A. Anders, editor, *Handbook of Plasma Immersion Ion Implantation and Deposition*, pages 243–301. John Wiley and Sons Inc, New York, 2000.

[149] J. R. Woodworth, I. C. Abraham, M. E. Riley, P. A. Miller, T. W. Hamilton, B. P. Aragon, R. J. Shul, and C. G. Willison. Ion energy distributions

at rf-biased wafer surfaces. *Journal of Vacuum Science and Technology A*, 20(3):873–886, 2002.

[150] J. R. Woodworth, B. P. Aragon, and T. W. Hamilton. Effect of bumps on the wafer on ion distribution functions in high-density argon and argon-chlorine discharges. *Applied Physics Letters*, 70(15):1947–1949, 1997.

[151] J. R. Woodworth, M. E. Riley, D. C. Meister, B. P. Aragon, M. S. Le, and H. H. Sawin. Ion energy and angular distributions in inductively coupled radio frequency discharges in argon. *Journal of Applied Physics*, 80(3):1304–1311, 1996.

[152] Z. W. Wu, Q. Sun, K. Ding, and C. X. Gu. Simulation and dose uniformity analysis of plasma based ion implantation. *Journal of Physics D: Applied Physics*, 38:4296–4301, 2005.

[153] M. Yan and J. Goedheer. Particle-in-Cell/ Monte Carlo Simulation of Radio Frequency SiH_4/H_2 Discharges. *IEEE Transactions on Plasma Science*, 27(5):1399–1405, 1999.

[154] O. Zabeida, A. Hallil, M. R. Wertheimer, and L. Martinu. Time-resolved measurements of ion energy distributions in dual-mode pulsed-microwave/radio frequency plasma. *Journal of Applied Physics*, 88(2):635–642, 2000.

[155] O. Zabeida and L. Martinu. Ion energy distributions in pulsed large area microwave plasma. *Journal of Applied Physics*, 85(9):6366–6372, 1999.

[156] Z. M. Zeng, T. Zhang, B. Y. Tang, X. B. Tian, and P. K. Chu. Improvement of tribological properties of 9Cr18 bearing steel using metal and nitrogen plasma-immersion ion implantation. *Surface and Coatings Technology*, 115:234–238, 1999.

[157] Z. M. Zeng, T. Zhang, B. Y. Tang, X. B. Tian, and P. K. Chu. Surface modification of steel by metal plasma immersion ion implantation using vacuum arc plasma source. *Surface and Coatings Technology*, 120-121:659–662, 1999.

[158] M. Zeuner, H. Neumann, and J. Meichsner. Ion energy distributions in a dc biased rf discharge. *Journal of Applied Physics*, 81(7):2985–2994, 1997.

[159] W. Zhang, Z. Wu, C. Liu, S. Pu, W. Zhang, and P. K. Chu. Experimental and theoretical investigation of the effects of sample size on copper plasma immersion ion implantation into polyethylene. *Journal of Applied Physics*, 101:1133021–1133025, 2007.

[160] J. F. Ziegler, J. P. Biersack, and U. Littmark. *The Stopping and Range of Ions in Solids*. Pergamon Press, New York, 1985.

[161] Y. Zou, Y. Cui, V. Yun, A. Valfells, R. A. Kishek, S. Bernal, I. Haber, M. Reiser, and P. G. O'Shea. Compact high-resolution retarding field energy analyzer for space-charge dominated electron beams. *Physical Review Special Topics- Accelerators and Beams*, 5(072801):1–7, 2002.